Metallurgical Issues in Low-Temperature Joining of Silver Nanowires

by

Peng Peng

A thesis
presented to the University of Waterloo
in fulfillment of the
thesis requirement for the degree of
Doctor of Philosophy
in
Mechanical Engineering - Nanotechnology

Waterloo, Ontario, Canada, 2014

©Peng Peng 2014

AUTHOR'S DECLARATION

I hereby declare that I am the sole author of this thesis. This is a true copy of the thesis, including any required final revisions, as accepted by my examiners.

I understand that my thesis may be made electronically available to the public.

Abstract

Silver nanowires (Ag NWs) have a wide range of applications in the electronic industry and are attracting growing world-wide interest because of their unique thermal, chemical, electrical and mechanical properties. Understanding of mechanical properties of Ag NWs and joining processes for them at a nano scale is urgently needed to support exploitation of their applications. Particularly, study of processing-structure-property relationships is of much significance. In the present thesis, the following research works were conducted.

Ag NWs were synthesized using the polyol method. Joining of individual Ag NWs in an end-to-end orientation at room-temperature without assistance of external pressure was investigated. Selective surface activation of Ag NWs provided surface free of protective organic layers for metallurgical joining. A similar crystal orientation was maintained between the NWs, and diffusion along the boundary contributed to the nanojunction formation. Monocrystalline V-shaped or zig-zag silver prisms were formed after nanojoining, terminated by twin boundaries and free surfaces.

The feasibility of room-temperature pressure-free joining of copper (Cu) substrates using Ag NW paste was conducted and demonstrated for flexible electronic packaging applications. The organic content in water-based Ag NW pastes was largely reduced by a repeated washing process to decrease the joining temperature. The formation of end-to-side or side-to-side joints between Ag NWs was observed concurrently with those joined end-to-end. The mechanical and electrical properties of Ag NW joints were examined. It was found that self-generated local heating within the Ag NW paste and Cu substrate system promoted the joining of Ag-to-Ag and Ag-to-Cu without any external energy input. The localized heat energy could be delivered in-situ to the interfaces and promoted atomic diffusion and metallic bond formation while the bulk component temperature maintaining near room-temperature. The organic layer on the side surfaces of the Ag NWs could be broken down through consumption of the residual PVP by a CuO-PVP reaction and which produced localized heating, increasing activated surface sites dramatically and making three-dimensional networks feasible.

Ag NWs were introduced into Ag nanoparticle (NP) matrices joined at low-temperature. Joining was facilitated by solid state sintering of the Ag nanomaterials and metallic bonding at Cu-Ag interfaces. It was found that Ag NWs in a Ag NP matrix acted as a second reinforcement phase. In

addition to improving the fracture toughness of joints, the introduction of Ag NWs affected the path of fracture propagation, where necking, breakage and pullout of Ag NWs occurred during loading.

Acknowledgements

At the end of my enjoyable and difficult journey in obtaining a Ph.D. degree, I would like to thank all those people who contributed in many ways to the success of this project and made it an unforgettable experience for me.

The greatest gratitude should go to my supervisors, Dr. Y. Norman Zhou, and Dr. Adrian P Gerlich. I am sincerely indebted to them from their incredible knowledge and deep insight in the field of joining and materials science. They introduced me into this interesting research area with their ongoing and unconditional guidance during my study at the University of Waterloo. They have taught me, both consciously and un-consciously, to have a sharp mind and eyes in science while keeping a good, well-rounded attitude. Without their continual guidance, encouragement and support, this work would not have been possible.

I wish to express my sincere appreciation to Dr. Anming Hu at the University of Tennessee. Dr. Hu set up a good example for me when he was at CAMJ. He is smart, hard-working and stringent with scientific research. Three years of working with him is successful and important for my future career. I would also like to thank Dr. Xiaogang Li, Dr. Yuquan Ding, Dr. Lei Liu and Dr. Scott Lawson at the University of Waterloo for their thoughtful discussion and suggestions of research and technical writings.

I would also like to thank all my friends inside and outside the CAMJ group for all their assistance: Yongde Huang, Andie Pequegnat, Golnaz Bohlouli, Robert Liang, Matthew Daly, Hong Huang, Ehsan Marzban, Wenchao Ma, and other good friends. Very special thanks to Chao Jin in Civil Engineering for discussion and exchanging critical thoughts on state-of-the-art technologies and interesting papers for learning new things and inspiring new ideas.

I greatly appreciate the financial support of the State Scholarship Fund of China during my study. Finally, a special thought is also devoted to my parents and my sister for the never-ending support. Their understanding and their endless love encouraged me to work hard and to continue pursuing a Ph.D. degree abroad.

Dedication

To My Family

Table of Contents

AUTHOR'S DECLARATION ii
Abstract iii
Acknowledgements v
Dedication vi
Table of Contents vii
List of Figures x
List of Tables xix
Chapter 1 Introduction 1
1.1 Low Temperature Joining Process 2
1.2 Mechanical Properties of Porous Materials 4
1.3 Motivation of Research 5
1.3.1 Issues Associated with Flexible Electronic Packaging 6
1.3.2 Advantages of Low-Temperature Joining of Ag NW Pastes 6
1.3.3 Mechanical Properties of Ag Nanoporous Materials 7
1.4 Objectives and Contributions of Research 7
1.5 Dissertation Organization 9
Chapter 2 Literature Review 10
2.1 Overview of Ag Nanomaterials 10
2.1.1 Synthesis of Ag Nanomaterials 11
2.1.2 Mechanical Properties of Ag Nanomaterials 14
2.1.3 Nano-indentation Characterization 27
2.2 Joining of Ag Nanomaterials 35
2.2.1 Basic Joining Concepts 36
2.2.2 Size Effects on Low Temperature Sintering 37
2.2.3 Progress in Low Temperature Joining of Ag Nanomaterials 39
2.2.4 Joining of Ag NWs 45
2.3 Problem Summary 48
Chapter 3 Joining of Individual Silver Nanowires 49
3.1 Introduction 49
3.2 Experimental 50
3.2.1 Synthesis of Ag NWs 50

3.2.2 Surface Activation Process 50
3.2.3 Characterization of Ag NWs 50
3.3 Results 51
3.3.1 Comparison of As-synthesized and Washed Ag NWs 51
3.3.2 Effects of Ultrasonication and Centrifugation 52
3.3.3 Joint Selection 54
3.3.4 Angle Measurement and Distribution 54
3.4 Discussion 57
3.4.1 Selective Surface Activation 57
3.4.2 Phase Relationships of Joints 60
3.4.3 Joining Mechanism: Self-Oriented Nanojoining 64
3.5 Summary and Remarks 66
Chapter 4 Joining Using Silver Nanowire Pastes 68
4.1 Introduction 68
4.2 Experimental 69
4.2.1 Synthesis of Ag NW pastes 69
4.2.2 Thermogravimetric Analysis 69
4.2.3 Joining using Ag NW Pastes 70
4.2.4 Tensile Testing 70
4.2.5 Nanoindentation 71
4.2.6 Resistivity Measurement 71
4.2.7 Microstructural Characterization 71
4.2.8 Local Heat Measurement 72
4.3 Results 72
4.3.1 Organic Content in the Pastes 72
4.3.2 Sintering Behaviors and Weldability of Pastes 75
4.3.3 Mechanical Properties of Ag NW Joints 76
4.3.4 Mechanical Properties of Ag NW Porous Materials 79
4.3.5 Electrical Property of Ag NW Joints 80
4.3.6 Microstructure Characterization 82
4.4 Discussion 85
4.4.1 Self-generated Local Heat 85

4.4.2 Local Heat: Lumped Capacity Model 87
4.4.3 Interfacial Reaction 89
4.4.4 Local Temperature 91
4.4.5 Local Heating Effects Induced Nanojoining 95
4.5 Summary and Remarks 97
Chapter 5 Reinforcement of Silver Nanoparticle Joints with Nanowires 99
5.1 Introduction 99
5.2 Experimental 100
5.2.1 Synthesis of Ag NPs and NWs 100
5.2.2 Joining using Ag NP-NW Binary Pastes 101
5.2.3 Tensile Testing 101
5.2.4 Nanoindentation 102
5.2.5 Microstructure Characterization 102
5.3 Results 102
5.3.1 Microstructures of Sintered Ag NPs and Ag NWs 102
5.3.2 Mechanical Properties 106
5.3.3 Fracture Behaviours of Joints 110
5.4 Discussion 114
5.4.1 Fracture Energy 114
5.4.2 Reinforcement Mechanisms 115
5.5 Summary and Remarks 118
Chapter 6 Conclusions and Recommendations for Future Work 120
6.1 Conclusions 120
6.2 Recommendations for Future Work 122
Reference 124

List of Figures

Figure 1.1 (a) Schematic of bonding with sintered nanomaterial fillers, *T*, *P* and *t* stand for sintering temperature, pressure and time, respectively. Interface qualities of nanomaterials - nanomaterials (b) and nanomaterials - substrates (c) affecting the joint properties (the critical separation distances of particle interfaces, *x*, and particle centres, *y*)...4

Figure 2.1 Typical micrographs of Ag NPs prepared with seed-mediated method with (a-b) different precursor volumes and (c-d) different seed solution volumes; Arrow in (d) indicating the multiply twined structure. (reproduced from [57]) 11

Figure 2.2 (a) SEM image of Ag NWs with pentagonal cross section. Schematic illustration of the mechanism proposed to account for the growth of silver nanowires with pentagonal cross sections: (b) Evolution of a nanorod from a MTP terminated by {111} end facets, and {100} side facets. (c) Diffusion of silver atoms toward the two ends of a nanorod, with the side surfaces completely passivated by PVP. (reproduced from [66]) 13

Figure 2.3 (a) HRTEM image of the cross-section of the Ag nanowires; the scale bar is 2 nm. The 2.08Å spacing labeled by white lines is indexed as d002. The inset shows the model of the 7.5 °misfit angle of a five twinned crystal. (b) Schematic illustration of the truncated decahedronal structure of Ag NW bounded by five [100] planes and capped by ten [111] planes at both the tips of the Ag NW, whose growth direction is along [110]. (c) The cross-section of the Ag NW, two distinct layers of five [110] plane subunits, overlapped onto each other. (reproduced from [70]) 14

Figure 2.4 (a) Hall-Petc

h and inverse Hall-Petch behavior in nanocrystalline copper; ΔH is the increment of hardness and *d* is grain size. (b) Schematic diagram of strength of polycrystalline materials as a function of grain size with Hall-Petch and inverse Hall-Petch relations involving the deformation mechanisms. (reproduced from [73, 76, 86])..16

Figure 2.5 Sample size dependence of yield strength in micro/nano pillars under compression punched with flat indenter. The surface effect and strain rate will affect the deformation process. (experimental data from [94], image from [95, 96])..17

Figure 2.6 Tensile testing of polycrystalline silver microwires with different grain sizes (*d*) and sample diameters (*t*). (a) Hall-Petch relationship applied to the 0.2% yielding strength. Analysis of the

proof strength with the relation of (b) sample size (*t*) and (c) shape effects (*t/d*) and (d) cooperated effects of sample and shape. (reproduced from [97]) 18

Figure 2.7 (a) In-situ TEM tensile test of penta-twinned Ag NWs with a diameter of 42 nm. (b) Experimental stress-strain curves of Ag NWs of varying diameter. The roman numerals I-IV on the stress-strain curve indicating the recording times of the corresponding TEM images in (a). (reproduced from [99]) 20

Figure 2.8 Images before and after deformation of (a) region where fracture occurred and (b) plastic region away from fracture point. Surface nucleation of stacking fault decahedra (SFD) formation in thin Ag NWs: Simulation snapshot of (c) the first partial dislocation nucleation from a penta-twinned Ag NW with D = 12 nm; (d) front side of the stacking fault decahedron (SFD) formed following the first dislocation nucleation event in (c); (e) A sequence of SFDs formed along the NW axis following the first SFD in (d). (f) TEM image of plastic region in NW, the inset shows a SAED pattern recorded from the same NW region indicating the [110] growth direction (d_{220} = 0.148). (reproduced from [99])21

Figure 2.9 Elastic modulus data from molecular statics simulations of ⟨110⟩ axially oriented nanowires with square, rhombic, and pentagonal cross-sectional geometry. "Nanowire thickness" is the shortest lateral dimension of each cross section. (reproduced from [101]) 22

Figure 2.10 (a) Size effect on the tensile yield strength of pentagonal, rhombic, and truncated-rhombic silver nanowires; Snapshots of silver nanowires with (b) pentagonal cross-section of 2.56 nm, (c) truncated rhombic cross-section of 1.9 nm, and (d) rhombic cross-section of 2.2 nm during tensile deformation at 300 K. (reproduced from [102])... 23

Figure 2.11 AFM images of pentagonal silver nanowire with 23.6 nm in diameter (a) before bending and (b) after failure. (Scale bars are 250 nm). (c) F-d curves recorded during the consecutive manipulation by AFM tip-induced lateral bending of a 23.6 nm pentagonal silver nanowire. Curves 1 and 2 show that the wire was elastically loaded and unloaded. The unloading points are identified as vertical dashed lines. Curve 3 is a single shot experiment and shows nonlinear elastic behavior of silver nanowire, followed by limited plastic deformation and then brittle failure. Note that F-d curves are shifted for clarity. Inset: schematic of bending test showing that the bending angle defined as the angle between the deformed wire and its original direction. (reproduced from [103])............................ 25

Figure 2.12. A schematic diagram of load-displacement curve from an indentation experiment. The quantities shown are P_{max}: the peak indentation load; h_{max}: the indenter displacement at the peak load;

h_f: the final depth of the contact impression after unloading; and *S*: the initial unloading stiffness. (reproduced from [110]) 29

Figure 2.13 TEM image taken from the in situ nanoindentation experiment. (a) the probe and silver nanoparticle before the nanoindentation. (b-e) during indentation, where contrast bands highlighted with A-H. (f) the probe and nanoparticle after deformation. (reproduced from [114]) 31

Figure 2.14 HRTEM image of (a) silver nanoparticle before compression, the present twin is highlighted; the (b) beginning and (c) middle of indentation, an edge dislocation is highlighted in the inset; (d) after indenter is removed. (reproduced from [114]) 31

Figure 2.15 (a) SEM image of solution-derived nanoparticle silver ink thin films sintered at 150℃ for 5-min. (b) Nanoindentation load-displacement curve for nanoink silver film on a Si substrate. (c) Indentation hardness as a function of fractional indentation depth. (reproduce from [115]) 33

Figure 2.16 (a,b) AFM images of indents on silver nanowires after nanoindentation; (c) height profile of an indent on the wire and (d) a representative nanoindentation load-displacement curve. (reproduced from [111]) 35

Figure 2.17 MD simulation of two large particles sintering at T = 63% T_m. (a-d) without grain boundary and (e-h) with grain boundary. Snapshots for the sintering process are t = 500, 50000, 200000 and 500000 steps. Every particle contains around 3000 atoms with bulk atoms (blue), surface or grain boundary atoms (red) and vapour state atoms (cyan), respectively. (reproduced from [157]) 38

Figure 2.18 Strength of joints bonded at different temperatures. (data from [18, 172, 174, 177]) 41

Figure 2.19 Strength of joints bonded with Ag nanomaterials at different sintering times. (data from [16, 174, 175, 178-182]) 42

Figure 2.20 Strength of joints bonded at different external pressures. (data from [164, 173, 175, 183, 184]) 43

Figure 2.21 Particle size effect on the strength of sintered nanomaterial joins. Closed symbols indicate that the sizes are uniform in the pastes; Open symbols represent average sizes of nanoparticles in the pastes with different gradations and the size distribution is represented as a solid line covering a range. (data from [173, 185]) 44

Figure 2.22 (a) Schematic illustration of chemically activated joining using cationic polymer or electrolyte solution. The microstructure of Ag NPs before (b) and after (c) applying cationic polymer. (reproduced from [186-189]) 45

Figure 2.23 Optical nanowelding set-up and scanning electron microscope (SEM) images before and after illumination. Finite element method simulations of optical heat generation at silver nanowire junctions during the nanowelding process. (reproduced from [9]) 47

Figure 2.24 Ag NW film: before (a) and after (b) applying 25 MPa pressure for 5 seconds. (reproduced from [201]) 48

Figure 3.1 Optical and SEM micrographs of (a,c) as-synthesized and (b,d) washed Ag NWs, illustrate that the V-shaped and *zig-zag* Ag NWs significantly increased after washing. 51

Figure 3.2 SEM images of (a) pristine Ag NWs in EG and after washing with (b) water, (c) acetone and (d) ethanol. 52

Figure 3.3 Optical images of Ag NWs after ultrasoncating with different time and energy. (a-d scale bars are 20 μm) 53

Figure 3.4 SEM images of V-shaped NWs formed (a) between two thin or thick NWs; (b) Thick NWs to thin NW. 53

Figure 3.5 Difference of (a) bending with one continuous curve, and (b) joining with sharp corner and two curved surfaces with small V-notch. 54

Figure 3.6 (a) Optical and (b) SEM micrographs of a bonded V-shaped Ag NWs (with 117° angle) laid flat on Si substrate. (c) High magnification of the V-shaped Ag NWs with two curved surfaces and a V-shaped notch in the joint region. 55

Figure 3.7 (a) Angle distribution of Ag NW joints. (b) TEM images of typical Ag NW joints. 56

Figure 3.8 TEM images of the end (a) and side (b) of pristine Ag NW; (c) and (d) washed Ag NW. Some areas on the end of Ag NW were exposed without organic coatings as highlighted in the circles in (c). Te breakage on the side of Ag NW is not significant in (d). (e) Schematic of assembly of Ag NWs by modifying the surface of NWs with polymer chains grafts of different chain densities. 59

Figure 3.9 (a) Ag NW joint with 126° angle: the SAED patterns on (b) upper wire with [011] and (c) bottom wire with $[\bar{1}12]$ zone axis, (d) right the joint region. (e) The HRTEM image of inner angle of the joint. 61

Figure 3.10 A typical joint of end-to-end Ag NWs: (a) TEM image of joint with a 126° angle; the SAED patterns of (b), (c) and (d) corresponding to two wires and joint shown in (a). 62

Figure 3.11 (a) Ag NW joint with 115° angle: the SAED patterns on (b) left wire with [011] and (c) right wire with $[\bar{1}12]$ zone axis, (d) right the joint region. (e) The HRTEM image of exterior angle of the joint, the (111) planes belong to two Ag NWs were matched with 10° mis-orientation. (The dashed circle indicating the contrasts from defects because of the mis-orientation)........................... 63

Figure 3.12 (a) Schematic illustration of end-to-end Ag NW joint, the cross-section of Ag NW is five-folded. (b) Two facets with different sizes attached via centre-to-centre and centre-to-edge configurations, letters H and L denote high and low diffusion sites belonging to different locations of Ag NWs. (c) The atomic arrangement of Ag NW join, when view from a [110] orientation that is on the coherent twin boundary with 70.53^{o} angle of *fcc* Ag. 66

Figure 4.1 Schematic illustration of (a) wire configuration during joining, (b) side-view and (c) cros-section of Ag NW joint after heating. *L* and *D* denote the joining length and thickness of joint......... 70

Figure 4.2 Schematic illustration of tensile shear strength testing of bonded samples. 71

Figure 4.3 Schemes of temperature testing configurations of (a) bare Cu substrate and (b) Cu-Ag NW paste system at room temperature. 72

Figure 4.4 (a) SEM image of as-centrifuged Ag NW paste (inset photo is the greenish-grey paste). (b) SEM image of pentagon- shaped (as arrows indicated) Ag NW with 60 nm mean thickness. (c) TEM image displayed the organic coating on the side of Ag NW. 74

Figure 4.5 TGA curves of three pastes with different washing times using DI water. Solid lines are weight (%) and dashed for derivate weight change (%/^{o}C).. 74

Figure 4.6 Microstructures of sintered Ag NW paste at (a) 200 ^{o}C for 5min on Si substrates; (b) Room-temperature, (c) 200 ^{o}C for 1hr and (d) 300 ^{o}C for 1 hr bonded Ag NW on Cu substrates....... 75

Figure 4.7 Photos of 250 μm copper wires bonded with (a) copper wire, (b) silver coated copper pad, (c) gold coated polyimide and (e) ITO plated PET. (f) 25 μm copper wire bonded on flexible ITO-PET. (scale bars are 10 mm)... 76

Figure 4.8 Tensile shear strength of bonded Cu-Cu wires with Ag NW paste as a function of joining temperature, the pastes washed once and twice for joining were compared (data of Cu NP are from [18] and data of Ag NP are from [172]).. 77

Figure 4.9 Tensile testing load-displacement curves of bonded copper wires with Ag NP and Ag NW pastes. 78

Figure 4.10 Typical load-depth curves Ag NP and NW porous materials (bulk Ag for comparison). 80

Figure 4.11 Relative resistivity of bonded Cu wire joint with Ag NW paste washed three times as a function of sintering and testing temperatures. Bulk resistivity of pure Cu wire was compared. Inset: the configuration of measured joint, relative resistivity was calculated using $\rho=RA/l$ with the measured resistance (R), cross-section area of joint (A), and length for measuring voltage drop (l)... 81

Figure 4.12 Microstructures of cross sections of Ag NW paste bonded Cu-Cu joints at room temperature: (a) Two Cu wires can be identified with a 20 μm gap filling with Ag NW paste with the bonded wires shown in the inset; (b) Optical microscope image of clear interface of Cu and Ag matrix; (c) SEM image of bonded interface of cross section shows the bond is continuous and formed metallurgical bond between the Ag nanomaterials and Cu wire; Dashed arrow indicating (d) the EDX line scanning direction, Ag and Cu elements formed a 0.5 μm transition layer by atoms diffusion.... 82

Figure 4.13 SEM (a) and TEM (b) images of three-dimensional Ag discontinuous networks formed at room-temperature. Arrows indicating the Ag-Ag junctions, numbers 1, 2 and 3 showing end-to-end, end-to side and side-to-side three different joining modes of Ag NWs. Fracture surface of joints formed at (c) room-temperature and (d) 300 °C. Circles indicated the failure of Ag NWs................. 83

Figure 4.14 SEM images of (a) failure joint bonded at room-temperature, the high-magnification images of squares corresponding to (b) Ag matrix surface, (c) folded Ag NW layer, with particles attached on AgNW and (d) Cu wire surface with EDX results. The Cu wire surface of failure joint bonded at (e) 100 °C and (f) 150 °C. 84

Figure 4.15 "In-situ cleaning" behavior of PVP during joining. 85

Figure 4.16 (a) DSC curve of Ag NW paste with Cu powder heating in air. (b) Temperature profiles of pure water and Ag NW paste with Cu substrate. 86

Figure 4.17 (a) Cu and NW paste plate assembly for heat energy calculation using lumped capacity model and (b) its schematic of temperature profile with calculated localized heat energies at the nanoscale. (c) Side view of localized interface with size configurations. 88

Figure 4.18 SEM images of (a) fractured sample and (b) fractured surface on Ag NW side. (c) Nanoparticle decorated Ag NW layer. (d) Comparison of InLens and Back-scatting images of NP decorated NWs, indicating the NPs have different composites with Ag NWs. (e) TEM micrograph of NP grow on the surface of Ag NW taken from Cu-Ag interface of bonded sample. 90

Figure 4.19 SEM micrographs of fractured interfaces of joint formed at room-temperature: (a) heated at 150°C for 1 hr and its high resolution image (b). 91

Figure 4.20 SEM and TEM images of (a, b) CuO grown on the surface of Ag NW at room-temperature with large portions of amorphous structures and (c, d) changing to Cu nanocrystalline structures after heating at 80°C for 3 hrs. 91

Figure 4.21 Schematic illustration of cross-section view of simplified Cu-Ag localized interface (a) before and (b) after temperature rise due to CuO-PVP reaction. 94

Figure 4.22 TEM images of (a) nanoporous Cu-Ag interface (arrows indicating the joining of Ag-Cu and Ag-Ag), (b) lattice image of Cu (111) -Ag (100) interface; (c) Cu-Ag interface and corresponding high-resolution image (b): lattice fringes showing the (111) plane of Ag and (200) of Cu well matched. Arrows indicating the lattice directions of polycrystalline Cu. 96

Figure 4.23 TEM images of the interface of two AgNWs of joint bonded at room-temperature (a) with end-to-end joining and square area corresponding to the high-resolution image (b); (c) tri-junction of Ag NWs and (d) lattice image of side-to-side Ag-Ag interface. 97

Figure 5.1 Schematic illustration of tensile shear strength testing of bonded samples. The starting distance between the grips was fixed at 40 mm, L and D denote the bonding length and thickness of joint. 101

Figure 5.2 Microstructure of condensed (a) AgNP and (b) AgNW paste after centrifuging. High magnification SEM images of (c) polyhedron shaped Ag NPs and (d) pentagon shaped Ag NWs with length of 10-20 μm and 50-100 nm thickness. 103

Figure 5.3 SEM images of Ag NP/NW paste sintered at different temperatures: (a) unsintered Ag NP/20NW paste, and sintered Ag NP/20NW paste at (b) 60 ^{o}C, (c) 100 ^{o}C, (d) 150 ^{o}C and (e) 200 ^{o}C for 1 hour with arrows highlighting the bridge paths between NP-NP and NP-NW. Sintered paste with different Ag NW volume additions (f) 0 vol.%, (g) 10 vol.% and (i) 30 vol.% after sintering at 150 oC for 1 hour. Inset low magnification image (h) and (j) are corresponding to Ag NP/10NW and Ag NP/30NW pastes. 105

Figure 5.4 During testing, two fracture modes for various NW contents: (a) filler material fracture and (b) interfacial fracture on the Cu wire and Ag nanopaste joint interface. 106

Figure 5.5 (a) Bond strength of bonded samples as a function of Ag NW volume fraction at different bonding temperatures. Squares, circles, triangles and diamonds represent tested samples bonded at 60°C, 100°C, 150°C and 200°C, respectively. Open and closed symbols, representing the filler material fracture and interfacial fracture, indicate the dominated fracture mode of bonded samples with various Ag NW contents. The dashed line denotes the fracture strength of copper wires. (b) The fracture strength of bonded samples of Ag NP/20NW and Ag NP pastes as a function of joining temperature. Star represents 60%Tin/40%lead commercial solder joint soldered at 200°C. 108

Figure 5.6 Typical load-depth curves of Ag NP-NW porous materials with different NW fractions.109

Figure 5.7 Microstructure of fracture Ag surface of NW reinforced Ag NP joints bonded at 150℃ with various Ag NW contents from (a) 0 vol.%, (b) 10 vol.%, (c) 20 vol.% to (d) 30 vol.%. Cracks are indicated by dashed lines. 111

Figure 5.8 Microstructures of cross sections of AgNP/20NW paste bonded Cu-Cu joints: The pulled out Cu wire can be identified by dashed line in an optical microscope image (a). (b) Ag matrix attached on the surface of bare Cu wire and (c) bonded interface of Cu-Ag with pore highlighted by arrow. Right column: (d) SEM image of bonded interface of cross section; (e) High magnification of interface shows lack of gap or debonding area between the Ag sintered nanomaterials and Cu wire; (f) The backscattered electronic SEM image for the interface, dark area denoting the Cu and bright area for Ag. 112

Figure 5.9 SEM images of Cu-Ag interface: (a) AgNP/20NW paste side with labelled 1, 2, 3 three points of interest, (b) Cu wire side with 4, 5, 6 points of interest, dotted line with arrows indicating the Cu wire. 113

Figure 5.10 Typical load-displacement curves of bonded joints: solid line for AgNP/10NW and dashed line for Ag NP. 115

Figure 5.11 SEM images of silver nanowires in joints after testing: (a) NW bent under stress with arrow indicating the bend region; (b) NW pullout, arrows highlighting residual NPs attached on the top and wall of NW; (c) Plastic deformation of NW with deformation regions highlighted by arrows; (d) NWs broken under stress, deformation region in the NW is shown. Not individually, the combined actions of Ag NWs are illustrated: (e) Bent NW was broken into two wires under stress, the fracture areas stayed in the circle; (f) NW was bent and pulled out, plastic deformation zones are highlighted by arrows. Dashed lines indicate the cracks. 116

Figure 5.12. Schematic mechanisms of AgNWs reinforcement in AgNP/NW joints: (a) Energy absorption causing crack closure by NP-NP debonding and crack propagation. (NP-NP bond < stress on crack tip); (b) While the crack grows in front of AgNW, the deformation splits along the NW and forms a compressive stress then bends the NW. The dispersed strain and energy consumption of bending NW stops the crack propagation or causes crack deflection. (Stress on crack tip < NW yield strength < NP-NW bond); (c) Deformation or even breaking of NW. (NW yield strength < Stress on crack tip < NP-NW bond); (d) NW being pulled out by debonding of NP-NW and further diversion of the crack. (NP-NW bond < Stress on crack tip). New generated smaller crack can propagate in the debonded areas. 118

List of Tables

Table 2.1 Comparison of three-point bending test of elastic modulus of as-synthesis and annealed silver nanowires with different diameters. (data from [103-106]) 26

Table 2.2 Projected areas, intercept corrections, geometry correction factors for various types of indenter tips. (The semi-angles given for pyramidal indenters are the face angles with the central axis of the tip) [109] 29

Table 2.3 Physical properties of inkjet-printed silver nanoporous layers after sintering for 24 h at different temperatures [118]. 34

Table 3.1 Measured angles of exactly the same Ag NWs with optical microscopic image (OM) and SEM image (SEM) 55

Table 4.1 Relative density, elastic modulus and hardness of Ag NP and NW porous materials (joining at 60°C). 80

Table 5.1 The fracture modes for bonded joints with various AgNW contents at different temperatures. 106

Table 5.2 Relative density, elastic modulus and nanohardness of Ag NP-NW porous materials (joining at 60°C). 110

Table 5.3 EDX results of selected points on two different sides of the interface of a joint bonded with AgNP/20NW paste at 150 ^{o}C 114

Chapter 1
Introduction

The miniaturization and multi-functionalization of devices with high efficiency and sensitivity are expected to meet the growing requirements. Based on such goals, numerous new materials and manufacturing processes have been explored, *e.g.* graphene, semiconductor or metal nanowires, *etc.* and nano-lithographing, three dimensional printing, *etc.* Various materials function as the basic building blocks in the devices, and contribute their certain properties to achieve required performance. Complex functions always need the cooperation of different materials. For example, flexible electronics are usually composed by thin film transistors with conductive and semi-conductive materials fabricated on bendable or stretchable organic substrates. Thus, assembly of functional components to meet certain requirement is one of the key processes for device realization.

Generally, smaller sized materials are more sensitive to the surroundings and reveal some new properties what their parent bulk materials barely exhibit. The most well-known terminologies are nano size effects and quantum effects. The former is used to describe the properties which have been enhanced from classic theories and bulk materials points of view when the material size decreasing to nano scale, 1-100 nm; the later deals with the properties beyond the classic physical and chemical theories. With these building blocks of devices or functional components from the macro and micro scales, down to the nano regime, many new properties which differ from their parent bulk materials have been discovered and lead to a broad range of applications. Meanwhile, numerous new challenges have also risen up and attracted growing world-wide interest. It can be grouped into three main areas: a) processing of nanostructures with different shapes and properties including nanomaterial design, synthesis and characterization; b) assembling technologies of nanostructures into devices; c) understanding the underlying mechanisms of properties and performances of nanostructures and devices.

Through decades of effort, a large amount of nanostructures have been synthesized ranging from zero to three dimensional crystalline materials and/or glasses, including metals, oxides, sulfides and many other compounds. Amongst a huge family of metal nanostructures, noble metals, such as gold and silver, are widely studied because of their excellent optical, electrical and thermal properties among all metals. Particularly, silver nanowires, a typical one-dimensional nanostructure, have attracted considerable attentions because of their unique thermal and electrical conductivities may

have extensive applications in electronic devices as high density logic circuits or interconnects. The waveguides and catalysis may also benefit from the excellent optical and chemical properties of silver.

1.1 Low Temperature Joining Process

It is well known that, as the size range transitions to the nanoscale, higher specific surface energy and increasing surface to volume ratio in the nanostructured materials enhances their sensitivity to heat. Although laser welding [1-3], spot welding [4], ultrasonic [5] and soldering [6-8] have been applied on nanomaterials successfully as in the case of welding of bulk materials, these conventional methods with high heat input processes may have a risk of damage to the ever-smaller and more delicate micro-electronic components and/or nano-objects when their original shapes are required to remain. Therefore, a low temperature or even room-temperature-interconnecting technique, such as optical welding [9] and cold welding [10, 11], is required to minimize the heat effects on the properties of heat-sensitive components during assembly.

Some studies have been focused on interconnecting individual silver nanomaterials to explore their application in nanodevices [12]. Since the contact interface is at a nanoscale for interconnecting nanomaterials, only a fraction of the energy input is required to achieve the metallic bonding via interdiffusion compared to macro scale joining, suggesting that the joining processes might be able to conduct at low temperatures. Some approaches benefit from nanotechnology, in which nanoscale diffusion bonding using metallic nanomaterials offers significant advantages over conventional soldering or adhesive bonding, such as lower bonding temperatures and higher diffusion rates [13]. It is also worth noting that this size effect has been long proposed as one of thermodynamic factors which suppress the melting point of metals at a nano scale [14, 15]. Considering the size effect and nanoscopic diffusion process of nanomaterials, developing a bonding method that can work at low temperatures by using silver nanomaterials is important for polymer and flexible electronics. Recently, low temperature joining techniques using a metallic nanoparticle paste, such as silver [16, 17], copper [18] or gold [19], appears to be a promising alternative for lead-free electronic packaging and flexible electronic interconnections.

Figure 1.1 shows a schematic of nanomaterials being used as filler materials to bond two components together. For example, this would be the typical case where a Ag-based nanopaste, containing Ag NPs and organic binders, is uniformly coated on clean surfaces of two bulk components. The components are typically held under a low compressive stress with the Ag

nanopastes at the interface, and sintered at a specific time and temperature, see Figure 1.1a. Often a shielding gas or vacuum is needed in the sintering processing in order to suppress oxide formation with more reactive nanomaterials. The bonded joints can be evaluated in terms of their thermal, mechanical and electrical properties. Similarly, these properties are controlled by two interfaces: nanomaterials-nanomaterials and nanomaterials-substrates as indicated in Figure 1.1b-c. It is worth noting that the bonding interface is built up via a bottom-up approach, where the porosity of the sintered nanomaterials and substrate coverage need to be considered when discussing the mechanical and electrical properties. Some porosity of the sintered nanomaterials always remains since pathways for the release of organic binders and solvents will be required during sintering. To reduce the porosity, applying external pressure and pre-sintering may be adopted and these treatments can have a significant positive effect on joint properties. However, the pores at the interface of nanomaterials and substrates, referred to as coverage in the 2D model shown in Figure 1.1c, are difficult to eliminate. Theoretically, there is only one layer of nanomaterials directly in contact with the substrates. Consequently, the coverage is $(1 - x/y)$, where x is the uncovered length and y stands for the central distance of two nanoparticles. To increase the coverage, the gap x should be decreased. Simply applying a force in one direction (vertically between two bulk components) cannot efficiently achieve a dense interface. Meanwhile, applying a force parallel to this interface (horizontally on the nanomaterials) is very difficult in practical applications since this filler layer is only tens of nanometers depending on the materials size in the nanopastes.

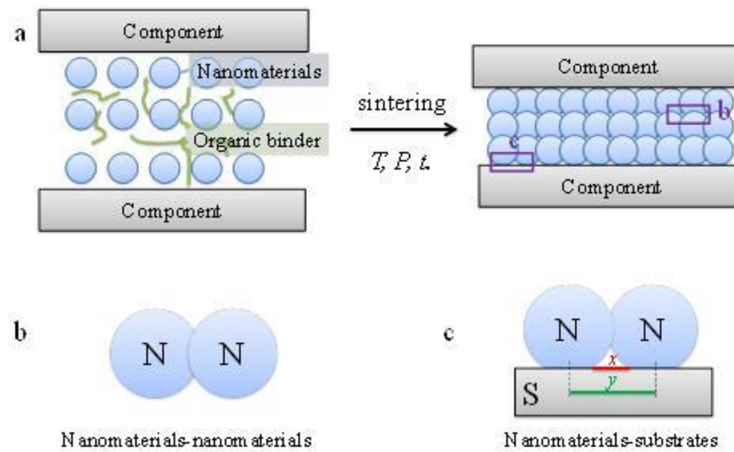

Figure 1.1 (a) Schematic of bonding with sintered nanomaterial fillers, *T*, *P* and *t* stand for sintering temperature, pressure and time, respectively. Interface qualities of nanomaterials - nanomaterials (b) and nanomaterials - substrates (c) affecting the joint properties (the critical separation distances of particle interfaces, *x*, and particle centres, *y*).

1.2 Mechanical Properties of Porous Materials

During the last 30 years, there has been a tremendous improvement in novel processing techniques and surge of research into the structure and properties of porous materials. These porous materials, such as foam, bone and lattice contain hierarchically arranged constituents and have a wide range of porosity with pore sizes spanning from nanometres to micrometres or even centimeters [20]. Nowadays, nanoporous materials are playing an important role in the fields of materials science, nanotechnology, chemistry, and bioscience. Many reports have been focused on their applications using their lightweight, high surface area for bioceamics [21] and tissue engineering [22-24], *etc*. However, the complete characterization of nanoporous materials still remains a difficult, which including their properties in such fields: novel solid hosts for confinement of matter on the nanoscale, highly specific shape selective catalysts for energy efficient organic transformations, new media for pollutant removal, and gas storage materials for energy applications [25, 26].

Among the various possible porous structures, metallic porous materials, especially nanoporous materials, occupy a special place since their distinct mechanical and chemical properties [27-31]. Generally, the mechanical properties (elastic modulus, E, and strength, σ.) of metallic porous materials are described using unit-cell geometry (open and/or closed cell) with the general relation as follows,

$$E, \sigma \propto \left(\frac{\rho}{\rho_{bulk}}\right)^n \qquad 1.1$$

here, n is a constant; the ρ/ρ_{bulk} is the relative density of porous materials (ratio of the density of foam to parent bulk material). For example, the strength of porous materials developed by Gibson and Ashby [32] can be written as, $\sigma=C_s\sigma_{bulk}(\rho/\rho_{bulk})^{3/2}$ (with n=1.5 in Eq. 1.1). C_s is the empirical materials coefficient [32, 33], which is a constant for metallic foam; σ_{bulk} stands for the strength of the bulk parent materials. This relation involves the relative density and the solid material mechanical properties with the assumption that the properties are independent of its dimension.

1.3 Motivation of Research

Joining of nanomaterials, namely nanojoining as a kind of assembly processes, can produce permanent unions or connections between nanosized building blocks and form functional devices and systems at the nano-scale. Joining methods also allow integrating these nanodevices and systems to their surroundings. Since the sensitive nanomaterials to external energy, such as heat and pressure, developing of nanojoining methods is required even massive joining processes have been developed for bulk materials. Therefore, joining of nanomaterials and forming metallic bonds would be an essential process for practical applications. In particular, developing a low temperature joining method that can work at high service temperatures by using nanomaterials, such as silver, is important for flexible electronics.

Considering the nano size effects, nanoscopic diffusion process would occur with a different manner as bulk materials since the surface energy of nanomaterials and driving force for diffusion are influenced by such effect. The understanding of nanoscopic joining process of silver nanowires can enrich the nanojoining theory and provide alternative joining methods for other materials. Silver, especially for silver nanowires, has revealed unique properties in service, such as thermal and electrical conductivities, which also has performed excellent mechanical properties as a typical ductile metal. Studying of their mechanical behaviors at a nanoscale allows one to exploit their property limits and stimulate new applications.

1.3.1 Issues Associated with Flexible Electronic Packaging

Flexible electronic packaging requires the process temperature below the softening or decomposition temperature which is usually < 250 ^{o}C. Different substrates have different softening temperatures. Thus, lower the processing temperature will broaden the selection of substrates. However, the current packaging techniques are close to 200 ^{o}C which restrict the practical applications. Also, some interconnect technologies have other concerns besides of high process temperature.

Wirebonding is a mature and dominant interconnect methods in packaging industry. However, it is good for two dimensional packaging but not suitable for three dimensional structures. Alternatively, solder reflow is a facile method and good for three dimensional packaging. The electrical and thermal properties of commercial solder materials are not as good as pure metals. The solder materials have thermodynamically stability issues [34, 35] because of the tin phase separation and coarsening (tin whisker growth) [36, 37] or crack growth [38] in the solder alloys. Further, this technique may have environmental concern if heavy elements such as lead are used in the solder. Pressure-assisted silver sintering can achieve good electrical and thermal performances because of the usage of silver. However, the external pressure is used to assist sintering process and that is inconvenience to build up complex interconnection structures. A relatively new packaging technology using conductive epoxy [39, 40] has great potential for flexible electronics since it has low processing temperature and is a very soft material. However, the electrical conductivity of conductive epoxy is still lower than commercial solders and pure metals.

1.3.2 Advantages of Low-Temperature Joining of Ag NW Pastes

A new filler material, silver nanowire (Ag NW) paste, and its subsequent room-temperature joining process are presented in this dissertation. The room temperature processing can make the flexible electronics packaging reality on various flexible substrates. The absence of external pressure during processing not only simplifies the packaging process and reduces the residual stress in the joints but also makes the three dimensional and/or complex structure packaging possible.

The Ag NW pastes can be applied through various forms, such as syringe-dispensing, screen printing, or stencil printing, and can be served as a direct drop-in substitution to the commercially available solders [17] as well. The reduction of organic binders in the pastes can achieve excellent electrical conductivity for the joints even processed at room temperature. Furthermore, unlike the

solder joint cannot function while the temperature is beyond the joint formation temperature because of the softening and melting of solders, Ag NW joint will be able to continue to serve at higher temperatures, in which the failure temperature is limited by the device and substrate, not by Ag NW filler materials. Finally, Ag NW porous materials are expected to have low modulus (~10 GPa) because of their porous microstructure, making it more compatible with flexible substrates and help with relieving the thermomechanical stress [17].

1.3.3 Mechanical Properties of Ag Nanoporous Materials

The study of nanoporous materials fabricated with top-down approaches is a long-standing focus in materials science. It has provided many examples to observe how bulk materials behave at the nano scale and extend the understanding from macro size to micro or nano scale. Investigating of bottom-up constructed nanoporous materials starting from nano scale building blocks can help to shed new understanding by explaining how nano building blocks behave at micro or macro scale.

The discussed low temperature joining process is one of these bottom-up construction techniques benefiting from the nanoscopic sintering. The produced silver nanowire nanoporous materials represent a good starting point, and example to expand the understanding of mechanical properties of nanoporous materials. It can also enhance the understanding of the relationship of mechanical properties between the building blocks and bulk materials. Accordingly, establishing a valid structure-property relationship is important to design of proper structural materials facing with practical demands.

1.4 Objectives and Contributions of Research

The aforementioned motivations drive to the investigation of joining processes of silver nanowires and their mechanical properties and applications. To be specific, the following scientific issues are addressed in the present work:

(1) Room temperature joining of individual silver nanowires is studied. Some previous researches have described interconnection of nanowires regarding nanoscopic soldering, plasmonic welding, and pressure welding. However, these methods involved localized melting with high temperature or severe deformation that can change the local structure or properties of nanowires. Recently, cold welding, a long studied technology in bulk materials, has been achieved in gold nanowires with the help of in-situ TEM technique. If individual silver nanowires can be joined at room temperature without localized melting and deformation, the practical application of high density

logic circuits would hopefully be realized in nanodevices. Thus, room temperature joining of individual silver nanowires and the joining mechanisms are of much interest and significance.

(2) Room temperature joining using silver nanowire pastes is conducted. Using silver nanomaterials as filler materials, the joints would obtain good electrical conductivity and thermomechanical stability. To implement the silver nanomaterial pastes into industrial applications, a pressure-assisted low temperature joining process has been achieved for die attachment. However, flexible electronics packaging requires even lower or room temperature joining processes. Interconnection of silver nanowires with substrates without external heat input would achieve real room temperature joining. A study of how the organic content of silver nanowire pastes affects the joint performance is essential to allow joining with flexible electronic packaging. The mechanical and electrical properties of porous materials based on silver nanowires are important for their practical applications.

(3) Mechanisms for room temperature joining using silver nanowire pastes are examined. When external heat and pressure input are absent, silver nanowires are usually difficult to interconnect due to the obstruction of organic layers at the interfaces. Identifying the trigger for the joining process and understanding the underlying mechanisms of room temperature joining can help to design active nanomaterial pastes in various joining systems for flexible electronic packaging.

(4) The behaviors of silver nanowires in nanoparticle matrices under loading are explored. Much attention is currently paid to low-temperature joining of silver nanoparticle paste for flexible electronic packaging. To improve the mechanical behaviors of silver nanoparticle joints, many research efforts have focused on tuning of the nanoparticle size, organic coatings on nanoparticles and binders in pastes. However, relatively little attention has been paid to the influence of the shape of nanomaterials for this low-temperature joining technology. This study is inspired by fiber reinforced composite materials, such as carbon nanotubes in polymers [41] and silicon carbide whiskers in aluminum alloys [42, 43], in which one-dimensional materials in the matrix can enhance the fracture toughness. Thus, silver nanowires may act as such in the nanoparticle joints. This motivates the investigation of the mechanical behaviors of silver nanowires in a nanoparticle matrix.

1.5 Dissertation Organization

The dissertation is organized into six chapters as follows:

The current chapter (Chapter 1) gives the necessary backgrounds and highlights the issues of interest regarding a) low temperature joining process which is an alternative material joining technique in electronics packaging industry; b) mechanical properties of porous materials. Chapter 2 reviews the previous works in relative areas systematically with consequently the proposed problems. In Chapter 3, a new strategy was discovered to interconnect individual silver nanowires through simply selective surface activation process. It was possible to join two or more silver nanowires with end-to-end configuration to form V-shaped or zig-zag silver nanostructures at room temperature. Following that, Chapter 4 presents a room temperature joining process for interconnecting massive silver nanowires and silver nanowires to copper substrate for flexible electronic packaging. This room temperature joining process was without any external heat and pressure input, but was induced by self-generated local heating effects. Chapter 5 investigates the mechanical behaviors of silver nanowires in the nanoparticle matrix. Silver nanowires could act as the second phase for both strength and toughness reinforcement in nanoparticle matrix. The reinforcement mechanisms were attributed to necking, breakage and pullout of these nanowires occur on loading. The conclusions as well as recommendations for further research are stated in Chapter 6.

Chapter 2
Literature Review

To utilize shaped nanomaterials for functional devices, joining of nanoscale building blocks with their original structure and shape is one of the essential manufacturing processes. However, producing permanent connections among such nanosized structures and forming nanosystems, and then integrating these connected materials to the bulk components or surroundings remains a challenge [13]. Exploring new joining processes at nanoscale has received increasing attention in electronic and optoelectronic industry. The chemical and mechanical properties of nanomaterials are strongly affected by their size; however, understanding the nano size effects on the nanojoining process and mechanical behaviors of joined nanomaterials is still incomplete. In this Chapter, two main introductions, silver nanomaterials including synthesis, mechanical properties with corresponding characterization methods, and low temperature joining of silver nanomaterials are given. In each case, the previous works are discussed and the current research hotspots and outstanding issues are highlighted.

2.1 Overview of Ag Nanomaterials

Silver (Ag) is a noble metallic material with a face-centred cubic (*fcc*) crystal structure. As a typical precious metal, it has long been used in coins, jewelry, tableware, decorated coatings, *etc*.. Bulk silver has melting point of 962 ^{o}C, density of 10.49 $g \cdot cm^{-3}$, thermal conductivity of 429$W \cdot m^{-1} \cdot K^{-1}$ (at 20 ^{o}C), electrical conductivity of 15.87 $n\Omega \cdot m$ (at 20 ^{o}C), elastic modulus of 83 GPa, shear modulus of 30 GPa, and Vickers hardness of 251 MPa. It is widely used as electrical contacts and thermal conductors, as mirror coatings and as catalysis of chemical reactions. Silver and its compounds are used as photosensitive and anti-microbial materials as well. Nanomaterials describe materials the dimension (at least one) of which is sized at nanoscale, 1-100 nm. For silver nanomaterials, including two-dimensional films, nanoplates, nanodisks, *etc.*, one-dimentsional silver nanowire, nanobelts, nanotubes, *etc.*, and zero dimensional nanocubes, nanodecahedrons, nanospheres, *etc.* [44-50], many reports focused on synthesis of different shaped and structured materials, characterization of their properties from macro to nano scale, and exploiting their applications. In this section, two main silver nanomaterials, nanoparticles and nanowires, are introduced regarding their synthesis methods and structure.

2.1.1 Synthesis of Ag Nanomaterials

2.1.1.1 Ag NPs

Silver nanoparticles (Ag NPs) have unique optical, thermal, chemical, and physical properties due to a combination of the large proportion of high-energy surface atoms compared to the bulk solid [51, 52]. Currently, wet chemistry process is the most common approach to synthesize Ag NPs with controllable size and shape.

Using silver nitrate ($AgNO_3$) as Ag source, Ag NPs can be prepared using borohydride [53], borohydride in basic medium [54], linear polyethylenimine (LPEI) [55] or citrate [56], *etc.*. The NP size can be controlled by changing the molar ratio of shape controlling agents to Ag source or seed-mediated regrowth process. Figure 2.1 shows the Ag NP size was well tuned through different seeds and precursor solution concentrations [57]. These polyhedral NPs are usually with multiple twins inside as indicated by arrow in Figure 2.1d.

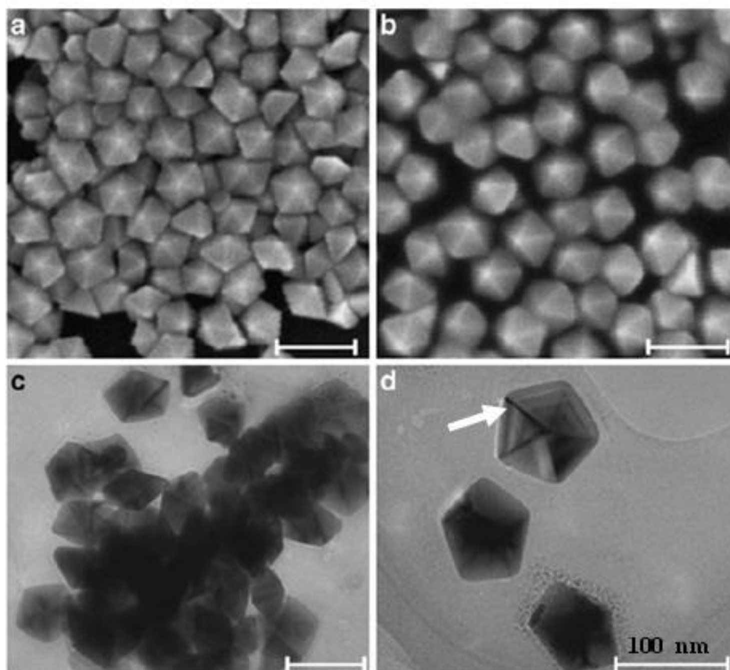

Figure 2.1 Typical micrographs of Ag NPs prepared with seed-mediated method with (a-b) different precursor volumes and (c-d) different seed solution volumes; Arrow in (d) indicating the multiply twined structure. (reproduced from [57])

2.1.1.2 Ag NWs

One-dimensional metallic nanostructures have attracted much interest due to their unique electrical, optical, magnetic, and thermal properties and the potential applications in nanoelectronics, optoelectronic devices and sensors, which also provide an ideal model system to experimentally investigate physical phenomena, such as quantized conductance and size effects in one dimension [58, 59]. Silver nanowires (Ag NWs) have received considerable attention due to the high electrical and thermal conductivities of bulk silver, in applications of electronics, waveguides, *etc.*.

Ag NWs can be synthesized within physical templates such as macroporous membranes, mesoporous materials, carbon nanotubes, DNA channels and organic nanotubes [60-62]. However, the template method has limitations, such as the diameter of NW dependence on the pore size of template, the limited amount of product and the cost of templates. Caswell *et al.* have reported a seedless and surfactantless wet chemical approach to prepare Ag NW [63]. Meanwhile, Wang *et al.* used glucose and AgCl to prepare AgNW with hydrothermal route [64]. However, the productivity and morphology of these Ag NWs are still uncontrollable. Furthermore, these methods are very time-consuming. Though Gou *et al.* modified a polyol method to synthesize Ag NWs within 3.5 minutes with the assistance of microwaves [65], this fast process is difficult to apply in fabricating Ag NWs with various lengths.

Sun *et al.* developed a polyol-process to obtain large-scale uniform Ag NWs using polyvinyl pyrrolidone (PVP) as a structure-directing reagent and NPs as seeds [66, 67]. This polyol method was considered as an efficient way to prepare Ag NWs with pentagon cross sections, see Figure 2.2. This type of Ag NWs has been widely used nowadays. In this typical polyol process, with PVP as a polymer capping reagent and the introduction of a seeding step, silver nitrate was reduced in the presence of seeds (Pt, Au, Fe or Ag particles of a few nanometers) and formed multiply twinned particles (MTP) via heterogeneous and homogeneous nucleation processes, respectively. In the early stage of the ripening process, the majority of larger silver particles could be directed to grow into nanorods with uniform diameters, which could then grow continuously into uniform nanowires of up to 50 μm in length because of the PVP's capping effects on Ag surface. Figure 2.2b-c shows a schematic illustration of the mechanism of growing silver into NW at the initial stage of the Ostwald ripening. Firstly, the formation of MTP with five-fold symmetry and ten {111} surface facets. Those MTP is a favourable structure once the particle size has reached a critical value in polyol process because of surface-energy minimization [66, 68]. Due to the highest-energy site of twin boundary on the surface of an MTP, silver atoms prefer to diffuse toward its vicinity during the Ostwald ripening

process. Consequently, rod-shaped nanostructure formed with the crystallization of silver atoms on the twin boundaries (labelled in red). The pyrrolidone units of PVP absorbed on newly formed {100} side surfaces through chemical interactions of Ag and O [69]. In comparison, the interaction between PVP and the {111} facets should be much weaker to enable the two ends of the nanorod to grow continuously. Therefore, the ends are largely uncovered and remain attractive toward new silver atoms. Figure 2.2c shows Ag atoms diffusion process, indicating that Ag atoms always prefer to diffuse to the ends of a nanorod because of their high chemical potential and reactivity. The HRTEM image of the Ag NW cross-section gives direct evidence of this five twinned structure as shown in Figure 2.3a. It can also be seen that large amounts of edge dislocations lie among the twinning boundaries. Some twin boundaries are narrow while others are broad to eliminate the gap of 7.5 ° misfit of the Ag nanowires. Figure 2.3b-c illustrates an ideal model of the three-dimensional structure and the pentagonal cross-section of those Ag NWs.

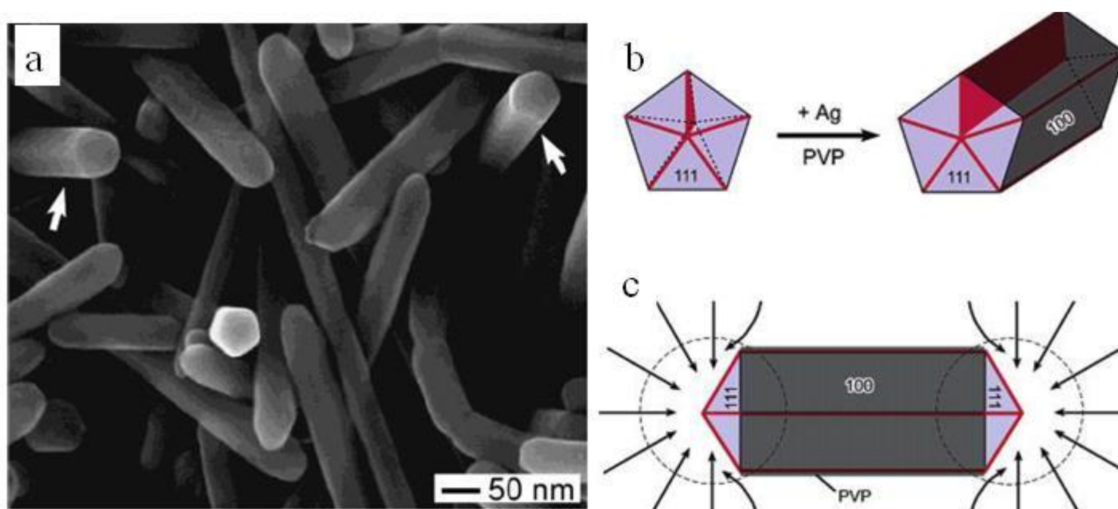

Figure 2.2 (a) SEM image of Ag NWs with pentagonal cross section. Schematic illustration of the mechanism proposed to account for the growth of silver nanowires with pentagonal cross sections: (b) Evolution of a nanorod from a MTP terminated by {111} end facets, and {100} side facets. (c) Diffusion of silver atoms toward the two ends of a nanorod, with the side surfaces completely passivated by PVP. (reproduced from [66])

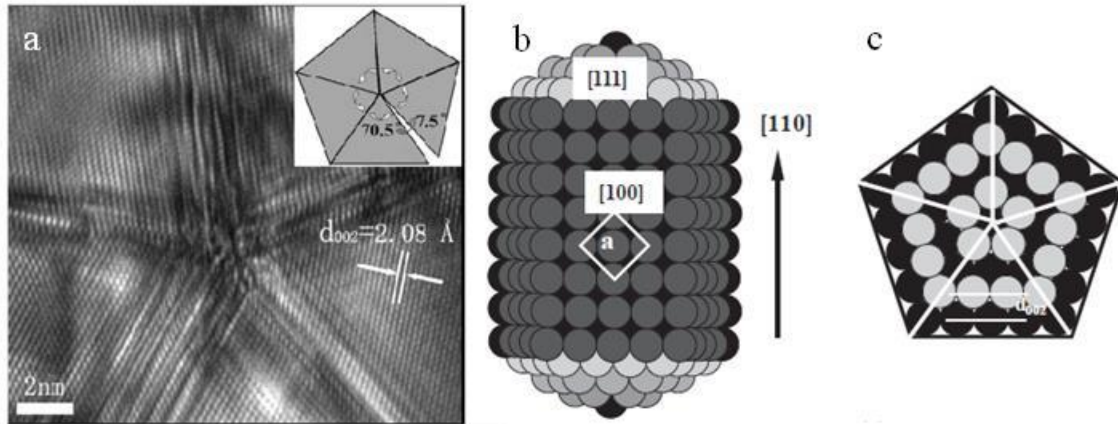

Figure 2.3 (a) HRTEM image of the cross-section of the Ag nanowires; the scale bar is 2 nm. The 2.08Å spacing labeled by white lines is indexed as d002. The inset shows the model of the 7.5 ° misfit angle of a five twinned crystal. (b) Schematic illustration of the truncated decahedronal structure of Ag NW bounded by five [100] planes and capped by ten [111] planes at both the tips of the Ag NW, whose growth direction is along [110]. (c) The cross-section of the Ag NW, two distinct layers of five [110] plane subunits, overlapped onto each other. (reproduced from [70])

2.1.2 Mechanical Properties of Ag Nanomaterials

Between the dimensions on an atomic scale and the dimensions which characterize bulk materials is to be found a size range where materials exhibit some remarkable specific properties [71], involving strength [72, 73], plasticity [74-77], melting temperature [71], chemical reactivity [78, 79], optical properties [80, 81], *etc*. Coming from the so-called microstructural constraint, size effects are attributed to the changes of physical properties of materials. In this section, only the nanoscale size effects on mechanical properties of silver nanowires are introduced briefly.

2.1.2.1 Size Effects: Grain and Sample Size, Probing Size

Size effects play an important role for miniaturization and the understanding of phenomenon in nanotechnology [82]. Regarding the strength of materials, it can be increased by reducing systems' characteristic length scales [83] because of the reduced possibility of pre-existing defects. The reduced length scales can be considered as size effects, including grain size, sample size, probing size.

2.1.2.1.1 Grain Size

Generally, the strengthening mechanisms in crystalline materials are attributed to the blockage and/or elimination of dislocations through like work hardening, precipitate, and grain boundary strengthening. Therefore, grain size, precipitate size, twin boundary spacing, or dislocation density would affect the deformation and strength of materials. For example, the strength of polycrystalline metals is well known to depend on grain size described with the Hall-Petch power relation [84-88] and inverse effect in the nanocrystalline regime, so called inverse Hall-Petch relation [89-92]. Hall-Petch strengthening (grain boundary strengthening) is due to the dislocation blockage, while inverse Hall-Petch softening is because of the dislocation elimination. These two relations follow the power law shown in Eq.2.1,

$$\sigma_y - \sigma_0 \propto d^n \qquad 2.1$$

where σ_y and σ_0 represent the yielding strength of polycrystalline metals and bulk properties, *d* is the grain size. Usually n is -0.5 for Hall-Petch power relation which positive *n* for inverse relation, see Figure 2.4a. Greer *et al.* concluded that the difference of dislocation mediated deformation and grain boundary mediated deformation would account for this transition when the grain size is smaller than 20 nm [76], see Figure 2.4b.

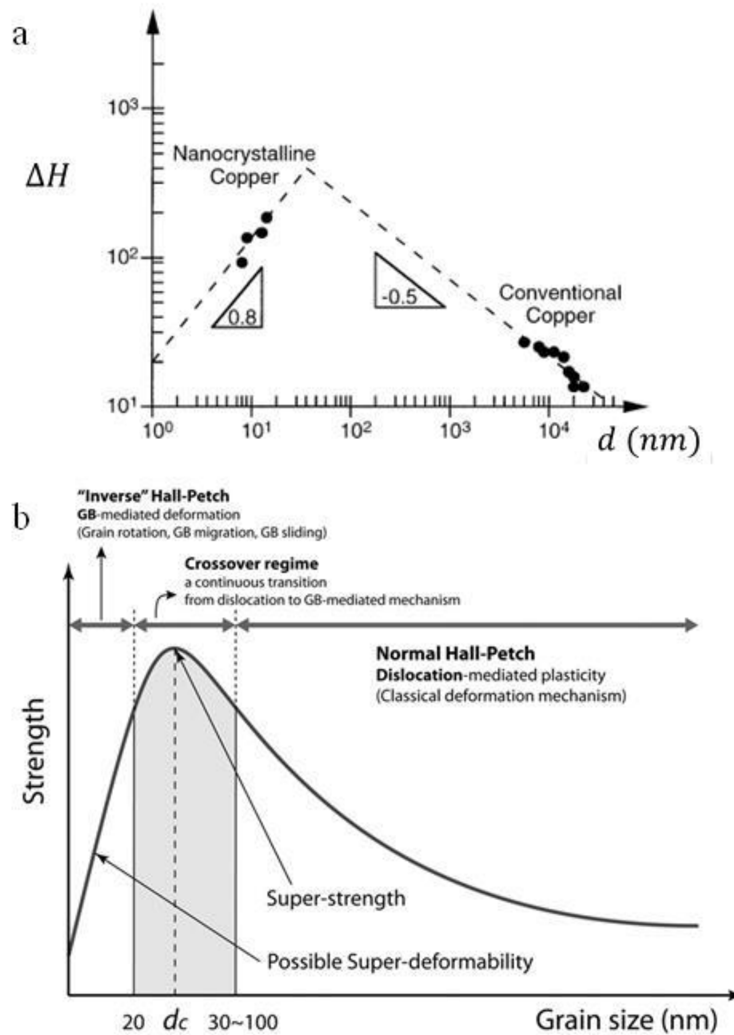

Figure 2.4 (a) Hall-Petch and inverse Hall-Petch behavior in nanocrystalline copper; ΔH is the increment of hardness and d is grain size. (b) Schematic diagram of strength of polycrystalline materials as a function of grain size with Hall-Petch and inverse Hall-Petch relations involving the deformation mechanisms. (reproduced from [73, 76, 86])

2.1.2.1.2 Sample Size

Recently, numerous small scale structures (micro to nano scales) regarding single or polycrystalline materials, such as wires, pillars, films, have been studied. It is showing that the strength of materials also holds a power law relation with the size of test samples as illustrated in Figure 2.5. It is worth noting that the sample size also includes thickness of thin films. The strength sometimes can be close to the theoretical strength of the parent bulk materials. Zhu *et al.* suggested

that the upper limit of strength is attribute to the surface dislocation nucleation under ultrahigh stress [83] since it is expected to dominate the dislocation nucleation process in nano-sized volumes [93]. The very small activation volume of surface dislocation nucleation would make the strength is strain rate sensitive at nano scale as well.

This sample size effects is known as “smaller is stronger” phenomenon. For example, Brenner reported that the tensile strengths of copper, ion and silver whiskers decreased with considerable scatter when the diameter and length of these whiskers is increased, suggesting the strongest whiskers are the smallest in size [72]. The highest strength values for these three metal whiskers were close to or above the lower estimate of the strength of perfect crystals.

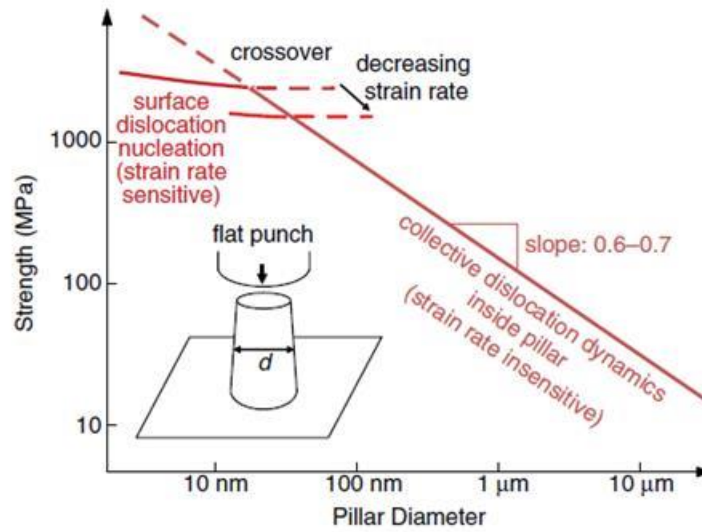

Figure 2.5 Sample size dependence of yield strength in micro/nano pillars under compression punched with flat indenter. The surface effect and strain rate will affect the deformation process. (experimental data from [94], image from [95, 96])

Chen *et al.* [97] has also demonstrated that the strength of polycrystalline silver microwires depended on both grain size (d) according to Hall-Petch and the wire thickness (t) with the relation shown in Eq.**2.2**.

$$\sigma_{0.2\%} = \sigma_1(t) + \sigma_2(t/d) + k_y d^{-1/2} \quad 2.2$$

The Hall-Petch relation when applying 0.2% strain, $\sigma_{0.2\%}=\sigma_0+k_y d^{-1/2}$, is plotted in Figure 2.6a. The sample size effects were expressed through specimen size effect $\sigma_1(t)$ and shape size effect $\sigma_2(t/d)$, as plotted in Figure 2.6b-d.

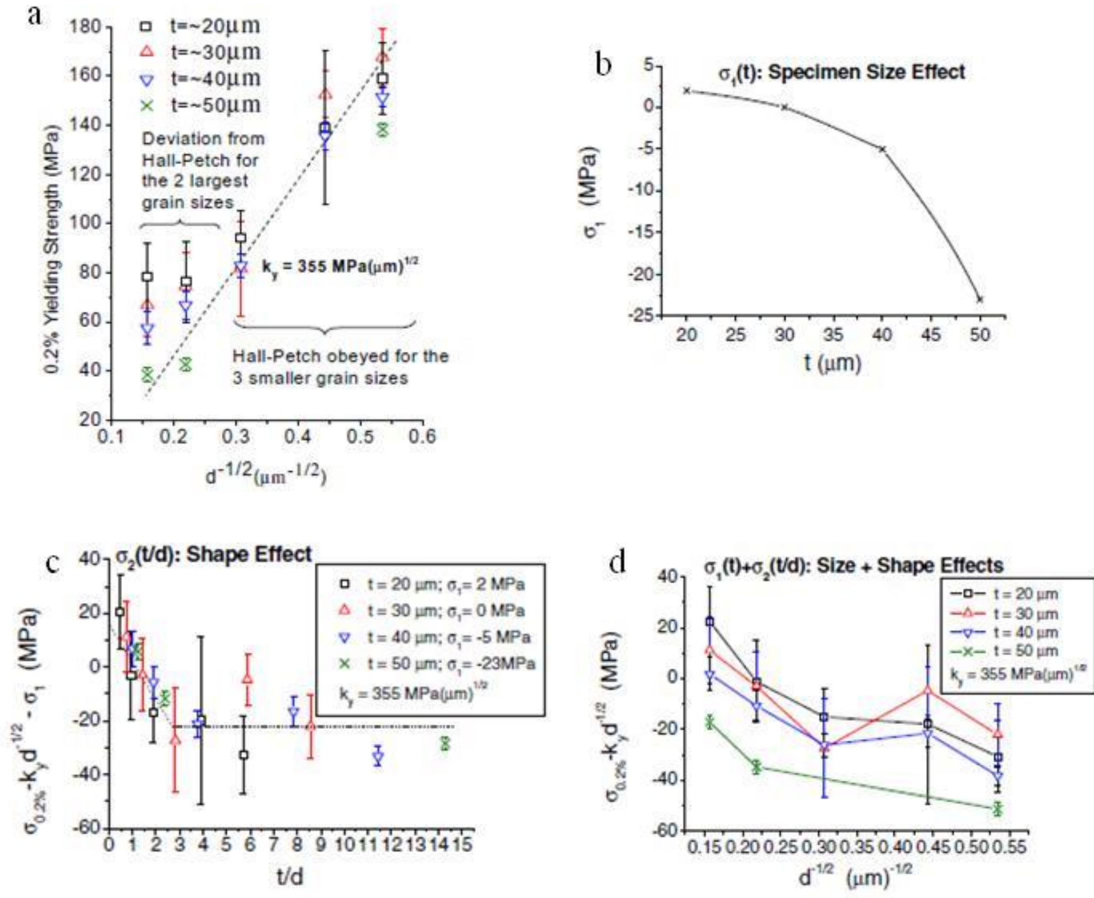

Figure 2.6 Tensile testing of polycrystalline silver microwires with different grain sizes (*d*) and sample diameters (*t*). (a) Hall-Petch relationship applied to the 0.2% yielding strength. Analysis of the proof strength with the relation of (b) sample size (*t*) and (c) shape effects (*t/d*) and (d) cooperated effects of sample and shape. (reproduced from [97])

2.1.2.1.3 Probing Size

Due the strain gradient, the probing size could also affect the mechanical properties of materials. For example, Nix-Gao's microindentation size effect model [77] exhibits the depth related indentation hardness of crystalline materials, described as Eq. 2.3 :

$$\left(\frac{H}{H_0}\right)^2 = 1 + \frac{h^*}{h} \qquad 2.3$$

where H is the hardness for a given indentation depth, h; h^* represents the characteristic length that depends on the properties of indented materials and the shape of the indenter; H_0 is the hardness in

the limit of infinite depth (when $h \gg h^*$). This relation agrees well with the experimental results when the indentation depth in micro scale. Based on this model, Huang *et al.* built a nanoindentaion size effect model [98] to predict the indentation depth in nano scale range. Therefore, this probing size regarding the contact loading zone is needed to be considered when the mechanical properties of materials are characterized as well.

2.1.2.2 Mechanical Properties of Individual Ag NWs

There are many works done on individual nanowires to understand the mechanical performance under strain at nanoscale. These nanowires include metals, copper, gold, silver, nickel, ion, semiconductor, silicon, zinc oxide, carbon nanotubes and various one dimensional materials. Here, only silver nanowire is reviewed. Most of mechanical behavior characterizations of silver nanowires are investigated by bending test, in-situ tensile test and molecular dynamics (MD) simulation.

2.1.2.2.1 Experimental Tensile Testing

Since Brenner developed a tensile testing experiment to study the mechanical behavior of microwhiskers [72], showing that decreasing of diameter of silver whiskers from 10 to 4 μm, the elastic strengths increased from 0.8 GPa to 1.8 GPa with considerable plastic deformation prior to fracture, some researchers reduced the thickness of silver nanowires and conducted the tensile testing. For example, silver nanowires with pentagonal cross-section and diameter range from 42-118 nm have been tested using in-situ TEM [99], see Figure 2.7. In-situ tensile testing is able to monitor the structure changes in real time. Figure 2.7a shows the number of deformation region increased with increase of strain. It is shown that the ultimate tensile strength increases from 2 to 6.5 GPa when the diameter of silver nanowires reduce from 118 to 42 nm, see Figure 2.7b. The calculated elastic modulus according to the slope of initial stress-strain curves is found to be about 124 GPa (1.5 times of bulk value) for the thinnest nanowire [99]. Similarly, the ultimate tensile strength of 2.35 GPa and elastic modulus of 148 GPa for 42 nm diameter pentagonal silver nanowires have also been reported based on in-situ SEM tensile testing by Zhu *et al.* [100]. During loading, the dislocations nucleated and propagated in discrete localized regions along the nanowires. The length of local plastic zones was proportional to the diameter of nanowire; however the number of local plastic zones had an inverse relation with that. The typical plastic regions at fracture tip and away the fracture point are shown in Figure 2.8a-b. Starting with the nucleation of partial dislocation (Figure 2.8c) on the surface of

nanowire, it could affect the entire cross section area between two twin boundaries to form a triangular stacking fault area. When this stacking fault reaches the twin boundaries, it activated the dislocations on {111} slip planes which can be grouped as two types: type-I is the mirror planes activated from twin boundaries; type-II is the mirror planes from surfaces, see Figure 2.8d-e. Consequently, these ten triangular stacking fault areas (five type-I, five type-II) formed a stacking fault decahedron (SFD), which structures have been observed experimentally, see Figure 2.8f. It is worth noting that the SFD chains could locally harden the silver nanowires and promote subsequent nucleation of stacking faults at other locations [99].

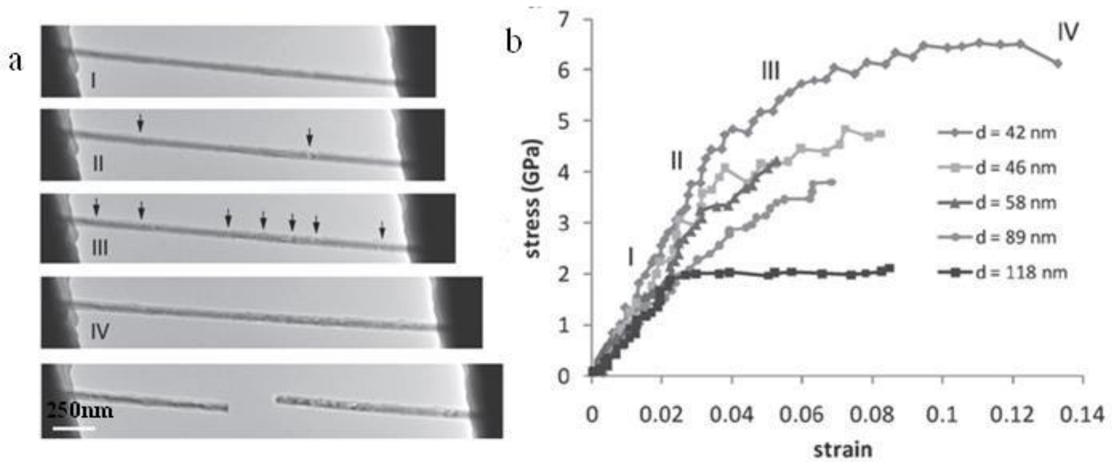

Figure 2.7 (a) In-situ TEM tensile test of penta-twinned Ag NWs with a diameter of 42 nm. (b) Experimental stress-strain curves of Ag NWs of varying diameter. The roman numerals I-IV on the stress-strain curve indicating the recording times of the corresponding TEM images in (a). (reproduced from [99])

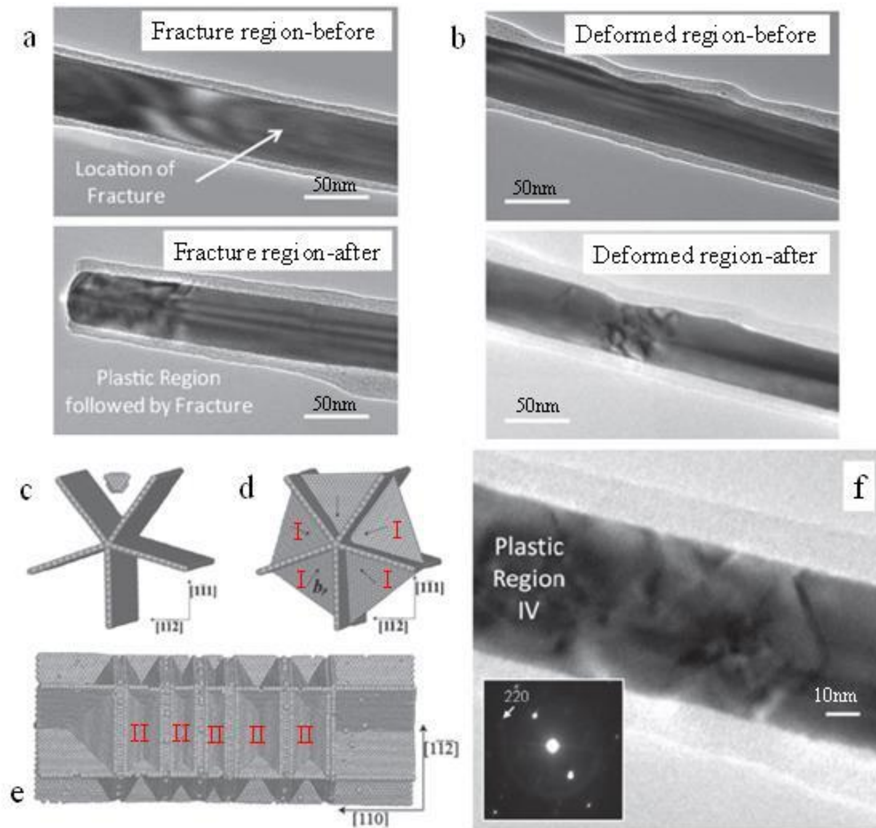

Figure 2.8 Images before and after deformation of (a) region where fracture occurred and (b) plastic region away from fracture point. Surface nucleation of stacking fault decahedra (SFD) formation in thin Ag NWs: Simulation snapshot of (c) the first partial dislocation nucleation from a penta-twinned Ag NW with D = 12 nm; (d) front side of the stacking fault decahedron (SFD) formed following the first dislocation nucleation event in (c); (e) A sequence of SFDs formed along the NW axis following the first SFD in (d). (f) TEM image of plastic region in NW, the inset shows a SAED pattern recorded from the same NW region indicating the [110] growth direction (d_{220} = 0.148). (reproduced from [99])

2.1.2.2.2 Simulated Tensile Testing

Molecular statics simulations using embedded atom method have been performed to determine the properties of silver nanowires with different cross-sectional geometries through strain the nanowire along the axial direction [101]. The relationship between elastic modulus and nanowire thickness is shown in Figure 2.9, which nanowires are with <110> axial orientation. The results suggested that the elastic modulus increased with decrease of nanowire thickness. The highest value is a round twice of bulk modulus for <110> silver. It can be seen that the cross section geometry had

no significant effects on their elastic modulus. However, it could cause the change of strength of silver nanowires according to Leach et al.'s results from molecular dynamics (MD) simulations [102]. Nano size effect on tensile strength of silver nanowires has been studied as well, see Figure 2.10. The pentagonal nanowire exhibited the highest yield strength for all size scale, see Figure 2.10a. The highest value is up to about 4.5 GPa when the diameter is only 1.6 nm for pentagonal nanowire. Other rhombic and truncated rhombic nanowires also exhibited ultrahigh yield strength when the diameter is less than 1.5 nm. The yield strengths decrease with increasing the diameters for all three nanowires. However, strengths became fairly stable when diameters were larger than 10 nm. Comparing the strains of three nanowires, the pentagonal nanowire has limited ductility due to the internal twin boundaries restricted the motion of partial dislocations, which twin boundaries also strengthened the nanowires (Figure 2.10b). The motion of partial dislocation is widespread along the nanowire and results in the truncated-rhombic nanowires with a strain of 24% before fracture (Figure 2.10c). The deformation twinning accounts for the plastic deformation of rhombic nanowires with over 40% strain before failure (Figure 2.10d) [102].

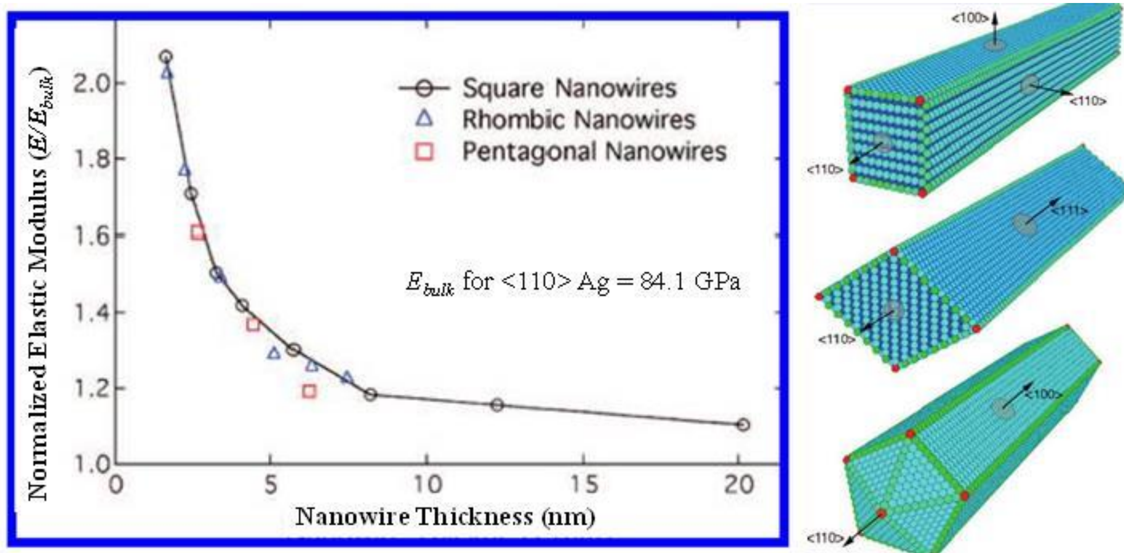

Figure 2.9 Elastic modulus data from molecular statics simulations of ⟨110⟩ axially oriented nanowires with square, rhombic, and pentagonal cross-sectional geometry. "Nanowire thickness" is the shortest lateral dimension of each cross section. (reproduced from [101])

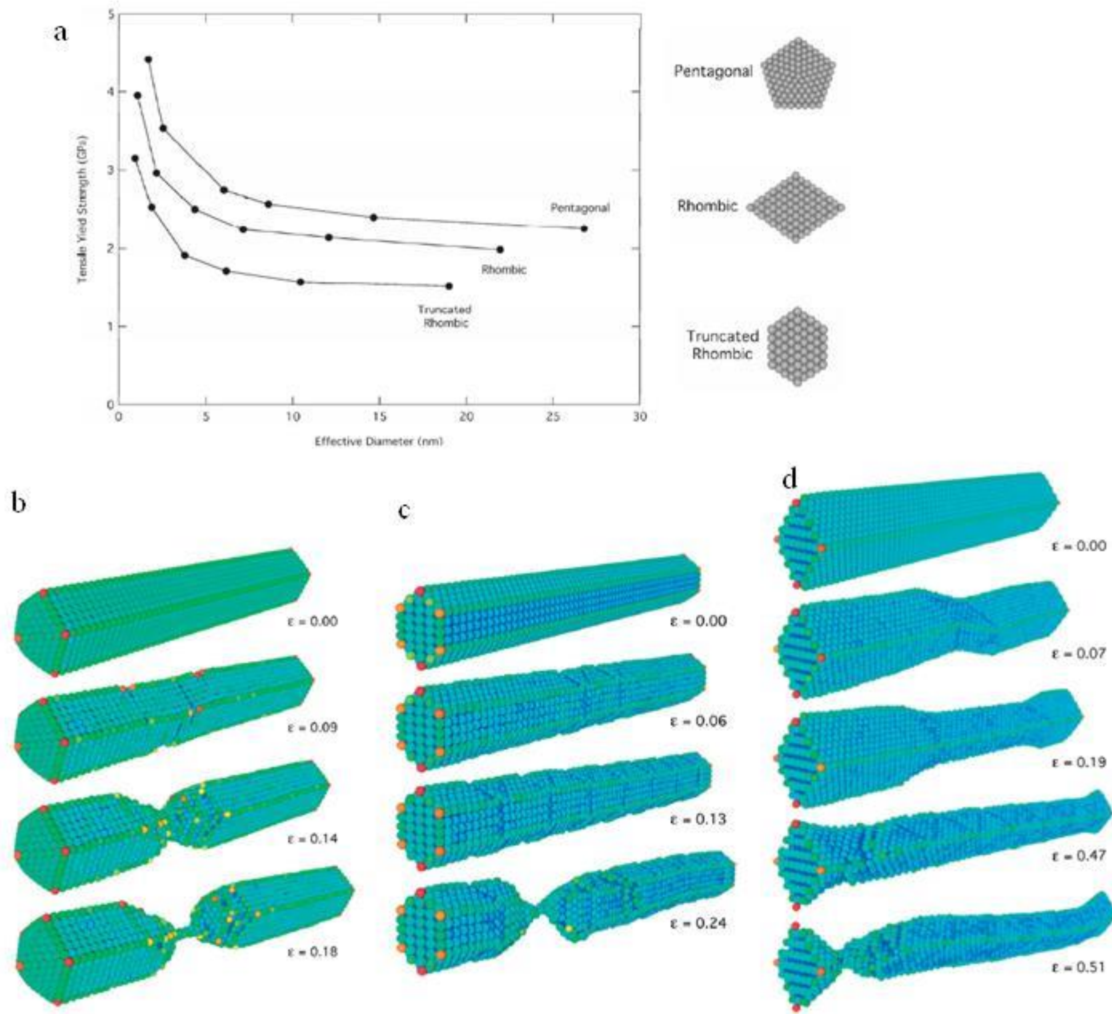

Figure 2.10 (a) Size effect on the tensile yield strength of pentagonal, rhombic, and truncated-rhombic silver nanowires; Snapshots of silver nanowires with (b) pentagonal cross-section of 2.56 nm, (c) truncated rhombic cross-section of 1.9 nm, and (d) rhombic cross-section of 2.2 nm during tensile deformation at 300 K. (reproduced from [102])

2.1.2.2.3 Bending Testing

Atomic force microscopy (AFM) has been employed to conduct three-point bending test of silver nanowires to measure their elastic modulus and yield strength as well with the nanowires crossing the trench (or hole) [103-106]. Firstly, noncontact mode is used to locate the nanowires and the bending point; secondly, AFM tip moves to the bending point (usually ½ of the cross length scale to simplify the calculation afterward) and applies force in contact mode, in which the force vs.

displacement curves are recorded; finally, AFM can be tuned back to noncontact mode to image the nanowire after bending test. The detailed procedures can be found in the literature [107]. Figure 2.11 shows a bending test on a 23.6 nm pentagonal silver nanowire reported by Wu *et al.* [103]. This nanowire fractured when the lateral force of AFM tip was 0.8 μN, see Figure 2.11c. Elastic modulus was calculated by fitting the initial force-displacement curve at small displacement, suggesting a 90 GPa modulus [103]. This three-point bending test on silver nanowires can be considered as fixed beam bending. Then the description of mechanical properties is expressed as [103, 108] according to the setup indicated in Figure 2.11c inset,

$$F_{center} = \frac{192EI}{L^3} f(a) \Delta z_{center} \tag{2.4}$$

where F_{center} is the applied force, E is elastic modulus, I is the moment of inertia ($I=\pi r^4/4$, r is the radius of nanowires), $f(a)$ stands for the rigidity enhancement function (proportional to maximum displacement $\Delta center$ under bending).

The elastic moduli of silver nanowires are compared in Table 2.1. Generally, the modulus increases as decrease of diameter of nanowire. The annealing process is to remove the twin boundaries [103] internal pentagonal silver nanowires and organic coating layers [105] on the surface. The annealed wires have much reduced elasticity with lower yield strengths because enhanced recrystallization by annealing results in elimination of twin boundary structure according to Wu *et al.* [103]. An ultrahigh yielding strength 7.3 GPa was estimated when the diameter is 16.3 nm that is substantially larger than that of bulk silver [103].

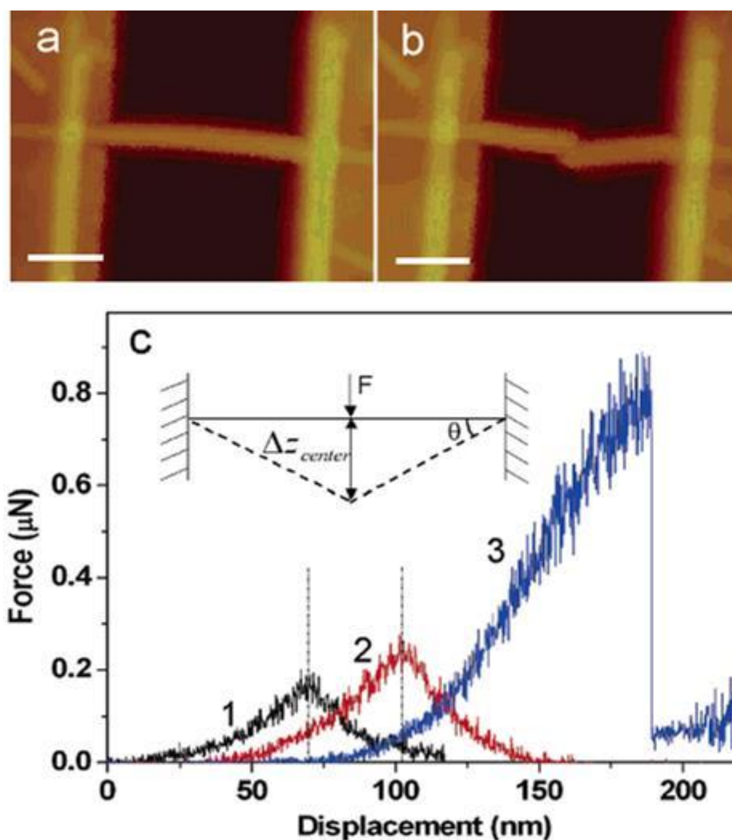

Figure 2.11 AFM images of pentagonal silver nanowire with 23.6 nm in diameter (a) before bending and (b) after failure. (Scale bars are 250 nm). (c) F-d curves recorded during the consecutive manipulation by AFM tip-induced lateral bending of a 23.6 nm pentagonal silver nanowire. Curves 1 and 2 show that the wire was elastically loaded and unloaded. The unloading points are identified as vertical dashed lines. Curve 3 is a single shot experiment and shows nonlinear elastic behavior of silver nanowire, followed by limited plastic deformation and then brittle failure. Note that F-d curves are shifted for clarity. Inset: schematic of bending test showing that the bending angle defined as the angle between the deformed wire and its original direction. (reproduced from [103])

Table 2.1 Comparison of three-point bending test of elastic modulus of as-synthesis and annealed silver nanowires with different diameters. (data from [103-106])

Diameter (nm)	Process	Elastic Modulus (GPa)	Yield Strength (GPa)	Synthesis Structure	Reference
64.2	annealed	94.3±5.9		Polyol Pentagonal	Chen et al.
65.9	as-synthesized	86.5±3.2			
84	annealed	91.3±5.6			
85.4	as-synthesized	83.7±9.4			
23.6	as-synthesized	90		Polyol Pentagonal	Wu et al.
23.2	annealed	121			
17	annealed	99			
16.5	annealed		7.3		
22-35	as-synthesized	102±23			
140	as-synthesized	75±15		Polyol Pentagonal	Jing et al.
100	as-synthesized	76±17			
75	as-synthesized	88±12			
59	as-synthesized	91±18			
40	as-synthesized	118±28			
20	as-synthesized	161±32			
135	as-synthesized	81.5		Electrochemical Unknown	Cuenot et al.
86	as-synthesized	89.6			
50	as-synthesized	120			
40	as-synthesized	138			
Bulk		83			

In-situ tensile testing requires the manipulation of nanowires, such as positioning, clamping, which could introduce artifacts or pre-exist strain interior nanowires and affect the results. Sometimes these defects or flaws can act as weak positions and cause the failure location on the edge of grips rather than in the gauge region. Since perfect alignment of nanowire axis with the tensile axis of grips is likely impossible, the misalignment angle usually varies (less than 25° is acceptable) and cause the fluctuation of measurements. Silver nanowires usually coat with an organics from chemical synthesis process or amorphous carbon from electron deposition during SEM/TEM observation. These coating

layers will also affect the stress measurements with up 11% error [99]. For MD simulations, the size of simulated materials is usually below 20nm and only very few in micron scale so far. To deal with the large numbers of atoms and short step times, computational demands are still prohibitive when trying to simulate the real nanostructures at realistic strain rates. Further, the embedded atom method used in MD simulations slightly underestimates the surface stress which might be an important parameter at nano scale in some cases.

2.1.3 Nano-indentation Characterization

Indentation testing is a method that using a materials with known properties to touch another materials of interest whose mechanical properties are unknown, such as elastic modulus and hardness [109]. Since the expression of Mohs' hardness, there are few types of hardness, Vickers, Brinell, Knoop, and Rockwell tests, have been established. Conventionally, these tests are with the length scale of penetration in micro- and/or milli- meters. When the length scale of penetration is in nanometers, the indentation test is so called nanoindentation. In this section, a brief background of nanoindentation technique using nanoindenter is presented.

2.1.3.1 Theory

In nanoindentation test, the size of the residual indention is only on the order of a microns or nanometers, which is too small to be measured directly with conventional methods. However, with the known geometry and well-shaped indenter, one can determine the area of contact via measuring the depth of penetration of the indenter into the material surface. It can record the contact area changes at full load directly. Thus, the nanoindetation tests can be considered a special case of the more general terms: instrumented indentation testing (IIT) or depth-sensing indentation (DSI) [109]. Nanoindentation can provide hardness, elastic modulus, strain-hardening exponent, fracture toughness and viscoelastic properties for the materials of interest. The most common data that are measured from nanoindentation testing are Hardness (H), Elastic Modulus (E) and Contact Stiffness (S). The theoretical background of these three is described below. Nanoindentation can be conducted using different indenter tips, such as sphere, flat, Berkovich, Vickers, Knoop, Cube corner, and Cone. Here, the most commonly used Berkovich tip (three-sided pyramid) is reviewed.

The nanoindentation hardness is defined by

$$H = \frac{P_{max}}{A} \tag{2.5}$$

where P_{max} is the maximum indentation force and A is the corresponding projected contact area at that load. The nanoindentation elastic modulus is calculated using the Oliver-Pharr data analysis method [110] through fitting the unloading curve to a power-law relation. The initial unloading contact stiffness, $S = (dP/dh)$, is the slope of the upper portion of the unloading data, as shown in Figure 2.12. According to Sneddon's relationships for the indentation of an elastic half space by any punch, a geometry-independent relation involving contact stiffness, contact area, and elastic modulus can be derived as follows [111]:

$$S = \frac{dP}{dh} = \frac{2\beta}{\sqrt{\pi}} E_r \sqrt{A} \tag{2.6}$$

where β is a constant that depends on the geometry of the indenter. It has a value of β =1.034 for Berkovich indenter [112]. E_r is the reduced modulus and A is the projected area of the elastic contact. The reduced modulus E_r accounts for the fact that the measured displacement includes contribution from both the materials of interest and the indenter tip. It is given by

$$\frac{1}{E_r} = \left(\frac{1-\nu^2}{E}\right)_{specimen} + \left(\frac{1-\nu_i^2}{E_i}\right)_{indenter} \tag{2.7}$$

where E and ν are elastic modulus (or Young's modulus) and Poisson's ratio of the specimen. E_i and ν_i are the same parameters for indenter. For the commonly used diamond tip, E_i and ν_i are 1141 GPa and 0.07, respectively [110].

The area function of a Berkovich indenter tip can be calibrated using fused quartz or other materials. A plot of the computed area as a function of contact depth is plotted and a fitting procedure can be employed to fit the A *vs*. h_c using a polynomial of the form [110],

$$A = C_0\, h_c^2 + C_1\, h_c + C_2\, h_c^{1/2} + C_3\, h_c^{1/4} + C_4\, h_c^{1/8} + \cdots + C_8\, h_c^{1/128} \tag{2.8}$$

C_0 for a Berkovich tip is 24.5. The first term describes a perfect Berkovich tip and the rest is deviations from the geometry due to tip blunting during indentation. If considering a perfect tip, then the relationship of projected contact area (A) and contact depth (h_c) for Berkovich tip can be expressed as Eq. 2.9.

$$A = 24.5\ h_c^2 \quad (2.9)$$

The nanoindentation related parameters of other indenter tips can be found in the Table 2.2 from the literature [109].

Table 2.2 Projected areas, intercept corrections, geometry correction factors for various types of indenter tips. (The semi-angles given for pyramidal indenters are the face angles with the central axis of the tip) [109]

Indenter type	Projected area	Semi-angle θ (deg)	Effective cone angle α (deg)	Intercept factor [a] ε	Geometry correction factor β
Sphere	$A \approx \pi 2Rh_c$	N/A	N/A	0.75	1
Berkovich	$A = 3\sqrt{3}h_c{}^2\tan^2\theta$	65.27°	70.3°	0.75	1.034
Vickers	$A = 4h_c{}^2\tan^2\theta$	68°	70.3°	0.75	1.012
Knoop	$A = 2h_c{}^2\tan\theta_1\tan\theta_2$	θ_1=86.25°, θ_2=65°	77.64°	0.75	1.012
Cube corner	$A = 3\sqrt{3}h_c{}^2\tan^2\theta$	35.26°	42.28°	0.75	1.034
Cone	$A = \pi h_c{}^2\tan^2\alpha$	α	α	0.727	1

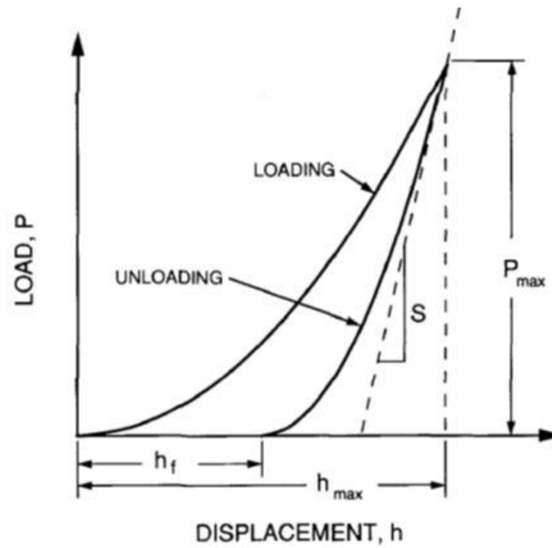

Figure 2.12. A schematic diagram of load-displacement curve from an indentation experiment. The quantities shown are P_{max}: the peak indentation load; h_{max}: the indenter displacement at the peak load; h_f: the final depth of the contact impression after unloading; and S: the initial unloading stiffness. (reproduced from [110])

2.1.3.2 Characterization of Ag Nanomaterials

There are large amount of works regarding nanoindentation characterization of nanomaterials with in-situ or ex-situ techniques. Here only the silver materials are summarized, especially nanoporous materials, regarding the characterization using nanoindenter. Generally, the peak indentation depth is controlled less than 30% of thickness of the measured materials to reduce the substrate effect on the measurement of the hardness and elastic modulus [113].

In-situ TEM nanoindentation was carried out on silver nanoparticles to observe the deformation and defects formation during compression in real time [114]. Silver nanoparticles were affixed to a metal wire and against diamond tip. The indentation steps are shown in Figure 2.13. It was observed that the strain on the nanoparticle caused several contrast bands (Figure 2.13b-e). After unloading, the contrast bands vanished when the strain was removed (Figure 2.13f). Through analyzing the possibility of which can cause these contrast bands, the localized strain near the core of dislocations was determined. There is an attractive force between dislocations and free surface of nanoparticles which can be changed because of the different strain energy when a dislocation moves towards to the free surface. Both dislocations and elastic type artifacts in nanoparticle can contribute to the absent of contrast bands when removing the strain. Under HRTEM, the revolution of dislocations can be observed, see Figure 2.14. It is suggested that the dislocation occurs and becomes more as the strain on nanoparticle increases. They are invisible when the indenter is removed finally. It confirmed that the dislocation caused contrast can be observed. However, the mechanical properties, such as hardness or elastic modulus, have not been shown in this work.

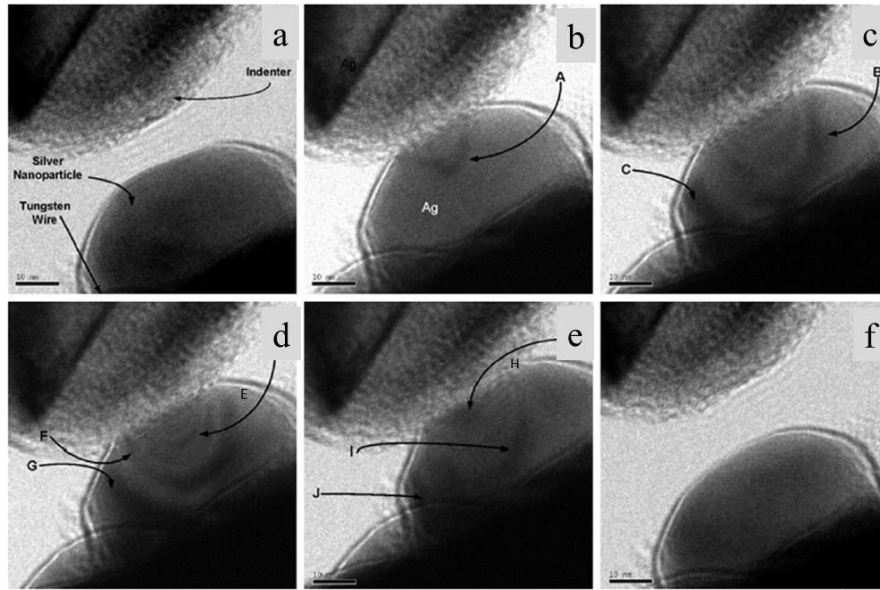

Figure 2.13 TEM image taken from the in situ nanoindentation experiment. (a) the probe and silver nanoparticle before the nanoindentation. (b-e) during indentation, where contrast bands highlighted with A-H. (f) the probe and nanoparticle after deformation. (reproduced from [114])

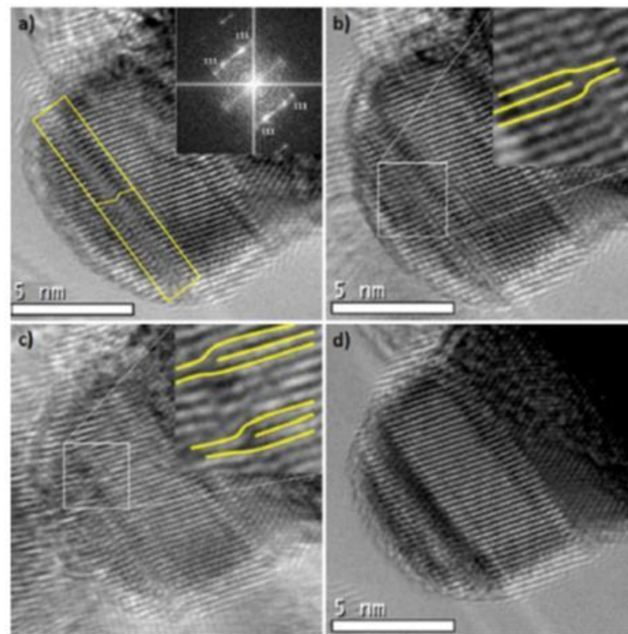

Figure 2.14 HRTEM image of (a) silver nanoparticle before compression, the present twin is highlighted; the (b) beginning and (c) middle of indentation, an edge dislocation is highlighted in the inset; (d) after indenter is removed. (reproduced from [114])

The mechanical properties of sintered nanoink silver films fabricated through spin coating and thermal annealing were characterized by Greer *et al.* [115]. The typical microstructure and load-displacement curve obtained for the film are shown in Figure 2.15a-b. To account for the effect of the substrate when the indentation depth is larger than 30% of the film thickness, Greer *et al*. used the method developed by Korsunsky *et al*. [116] to calculate the true film hardness from the measured value H_{meas},

$$H_{meas} = H_{Si} + \frac{H_f - H_{Si}}{1 + {h^2}/{\chi t}} \qquad 2.10$$

where H is the respective harness (subscripts 'Si' and 'f' present Si substrate and silver film), h is the indentation depth, and χ is the geometric parameter and t stands for the thickness of silver film. The hardness of film and substrate composite based on Eq. 2.10 and the measured data are shown in Figure 2.15c. Consequently, the average hardness was 0.91 GPa for the sintered nanoink silver films with a 50 nm particle size, which is half of the hardness of a corresponding nanocrystalline silver film with a 50 nm gain size, being 1.8 GPa [115]. The average elastic modulus was 110 GPa which is lower than the value of 148 GPa reported by Panin *et al.* [117] due to the incomplete sintering of silver nanoparticles.

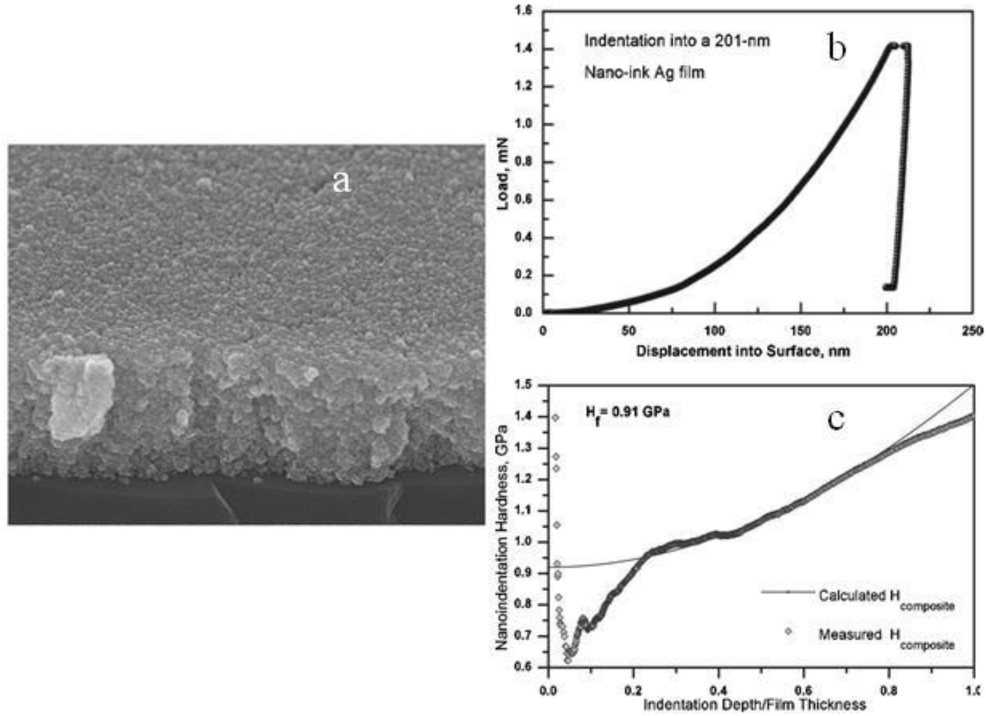

Figure 2.15 (a) SEM image of solution-derived nanoparticle silver ink thin films sintered at 150℃ for 5-min. (b) Nanoindentation load-displacement curve for nanoink silver film on a Si substrate. (c) Indentation hardness as a function of fractional indentation depth. (reproduce from [115])

Recently, the inkjet-printed silver nanoporous films have also been studied by Dou *et al.* [118]. The effect of nanoparticle size (ligament thickness) was investigated. By applying known relative density ($\rho_{foam}/\rho_{ligament}$) and measured apparent strength (σ_{foam}) of silver foam, the strength of nanoporous materials can be calculated with the following expressions [32, 119].

$$\frac{\rho_{foam}}{\rho_{liagment}} = \frac{(t/l^*)^2\left(1 + 0.776(t/l^*)\right)}{0.776(1 + t/l^*)^3} \quad 2.11$$

$$\frac{\sigma_{foam}}{\sigma_{liagment}} = 0.3\frac{(t/l^*)^3}{(1 + t/l^*)^2} \quad 2.12$$

where l^* represents the length of ligament loaded in shear and t is the thickness of ligament. Table 2.3 shows these calculated ligament yield strength of sintered nanoporous silver films and other properties. The ligament strength show very high values, up to 1 GPa when the ligament size is 80 nm which is greater than the strength of bulk polycrystalline, that increases with decreasing the ligament size [118]. This work shows an obvious nano size effect on mechanical behavior of silver. The nucleation of Shockley partial dislocations and deformation twins in micro scale accounts for the high

strength. However, the scaling relation of strength for nanoporous silver is not well discussed and the evolution of deformation microtwins is still unclear as well.

Table 2.3 Physical properties of inkjet-printed silver nanoporous layers after sintering for 24 h at different temperatures [118].

Annealing temperature (°C)	Mean ligament diameter (nm)	Young's modulus (GPa)	Hardness (apparent strength, MPa)	Relative density (%)	Ligament strength (MPa)
180	80 ± 10	6.40 ± 1.0	74 ± 10	28 ± 2	1070 ± 150
280	160 ± 15	4.34 ± 0.5	30 ± 10	22 ± 2	660 ± 120
380	230 ± 20	4.60 ± 0.5	23 ± 6	24 ± 2	480 ± 100

Flat punch nanoindentation has been performed on silver micro pillars to investigate the deformation behaviors by Buzzi *et al.* [120]. They suggested that deformation localized at twin boundaries which are formed due to the dislocation slip on (111) plane. The dislocation and deformation twinning were caused by the low stacking fault energy of silver. The inverse dependence of strength on the diameter of pillars is presented. However, pillar diameter is in submicron level and not reach 100 nm and below. The study of if the deformation behavior of nanopillars (and/or nanowires) follows the same process is needed to understand the nano size effects on mechanical properties of silver nanomaterials.

A nanoindentation study on silver nanowire with 4 µm long and 42 nm in diameter conducted by Li *et al.* [111] is shown in Figure 2.16. The AFM images and height profile were employed to calculate the indentation projected areas since the wire is curved which is different with the circumstance of flat surface usually involved. There is a step (or namely pop-in mark sometimes) in the loading curve, see Figure 2.16d. The loading curve before the step was used to calculate the elastic modulus using Hertzian elastic contact mode. The fitting result indicated the elastic modulus of silver NW is 88 GPa. The hardness is about 870 MPa. These two values are in good agreement with the nanoindentation results of bulk silver single crystal [111]. They also suggested that the step on loading curve was attributed to beginning of plastic deformation associated with the dislocation nucleation and motion [121]. The nucleated dislocations led the indentation more difficult afterward and increased the slop of loading curve.

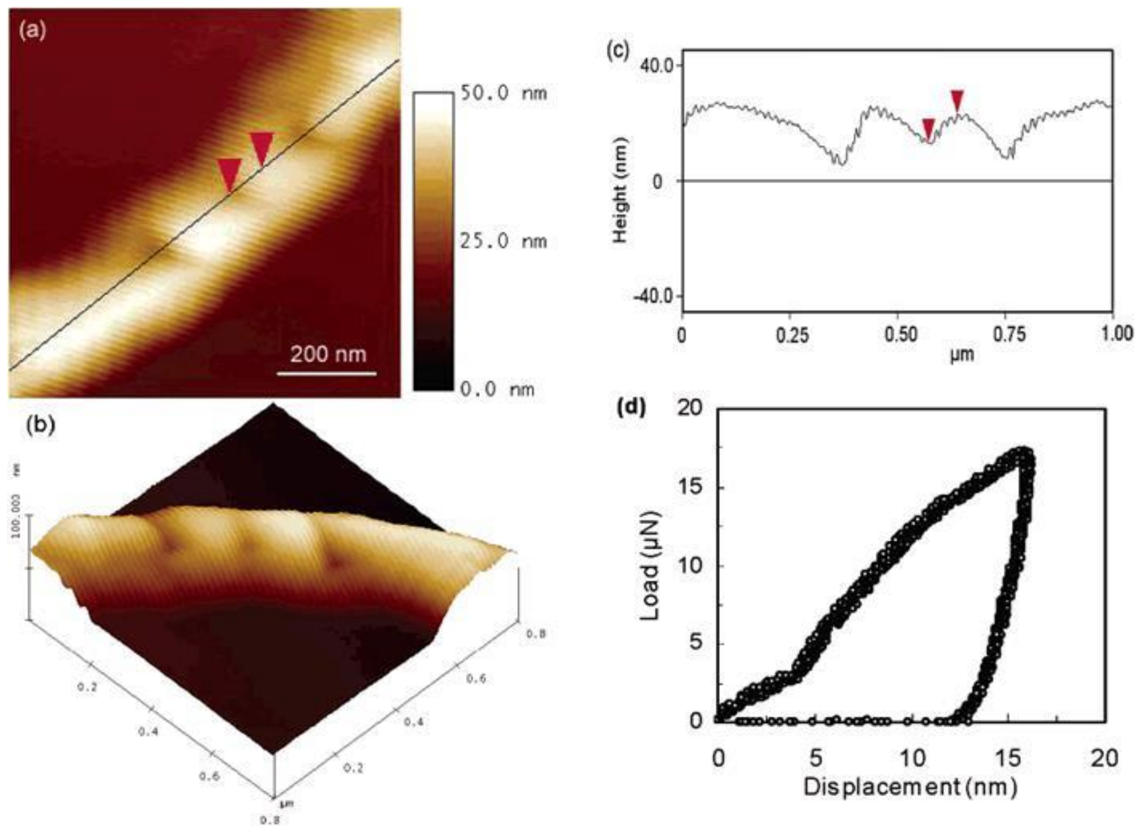

Figure 2.16 (a,b) AFM images of indents on silver nanowires after nanoindentation; (c) height profile of an indent on the wire and (d) a representative nanoindentation load-displacement curve. (reproduced from [111])

2.2 Joining of Ag Nanomaterials

Similar to classified features and terminologies in regular welding and microjoining, the current joining methods for nanomaterials can be divided into three categories on the basis of the physical state of base components: fusion welding, solid-state joining, brazing and soldering. When the size of joining components shrinks to nano scale, nano size effect can stimulate the low temperature joining process. Regarding silver nanoparticles, this low temperature joining process has been applied in electronics packaging industry to replace the micro silver flack pastes. At present, limited research has investigated low temperature joining of silver nanowires and its application for flexible electronics packaging.

2.2.1 Basic Joining Concepts

At the macro and micro scale, various joining processes have been developed to fabricate metallic interconnects for achieving good mechanical strength and electrical conductivity in bulk materials. Roughly, they can be classified as three major types based on the physical states of the parts to be joined: fusion welding, soldering/brazing, solid-state bonding [122].

In general, fusion welding processes involving the high heat input and high temperatures using various energy sources, including laser [1-3], electron beam [123], electrical resistance [6], plasma [124], microwave [125-127] and chemical reaction [128], which all cause local melting of the base building blocks. In terms of soldering and brazing, important methods of joining materials without melting the base components, molten filler metal is introduced between the base components for their metallurgical reaction which includes the dissolution process of the solid base metal into molten liquid and then formation process of a reaction layer between them [13, 129].

Among brazing and soldering, the filler metals typically have low liquidus temperatures (< 450 ^{o}C) in soldering, and originally contained lead which raised many concerns due to health, environmental and safety issues worldwide. Presently, even the well-developed lead-free soldering technology [130-133], where the general melting point of filler metals ranges from 200 to 300 ^{o}C, is still insufficient to satisfy the requirement of interconnection of heat-sensitive substrates, thus restricting the popularization of flexible electronic or organic light-emitting devices [11, 134, 135], and ferroelectric materials with low transition temperature or organic ferroelectric materials [136-138].

As solid-state bonding processes, friction welding [139, 140] or ultrasonic wire bonding [141] will introduce high strain and plastic deformation to the parts at near their melting temperatures. Solid-state sintering or even diffusion bonding of bulk materials, are typically carried out in an inert atmosphere or vacuum, and involve temperatures at least over half of the melting point, with pressures between 1 to 10 MPa [142]. The bond formation generally takes place in two phases, first where a partial bond is formed and the asperities between the components begin to collapse with residual porosity between the joined asperities. Then a complete bond is formed after prolonged times at high temperatures such that diffusion and creep increase the contact area.

2.2.2 Size Effects on Low Temperature Sintering

Sintering occurs by migration of atoms mainly along the particle surfaces, suggesting that surface energy and curvature would be the dominant factors for sintering. Surface energy, γ, is an excess free energy and it is the reduction in surface area which drives the sintering process. It is defined to be the energy to create a unit area of surface [143].

The driving force at the interface when two spherical particles contact is given by the Laplace equation,

$$P = P_0 + \gamma\left(\frac{1}{R_1} + \frac{1}{R_2}\right) \qquad 2.13$$

where R_1 and R_2 are the principal radii of curvature at the contact point of the surface. P_0 is the pressure external to the surface and γ is the surface energy, $\gamma=(\partial G/\partial A)_{T,P,n}$. The surface energy includes the structural contribution due to surface stress derivation and surface chemical contribution from the energy in breaking bonds related not only to curvature, but also to stress and composition [144]. Therefore, the driving force for reduction of surface area will increase when the size of particles decreases to nano scale.

Generally, the sintering process is controlled by sintering temperature and time. The sintering temperatures of materials can be written as,

$$T_s = \alpha T_m \qquad 2.14$$

where T_s is the sintering temperature and T_m is melting temperature dependent on the material. The factor α is dependent on material geometries and other environmental conditions. Thus, the effective sintering temperature is contributed by two aspects, the coefficient α and melting temperature T_m. Although sintering processes proceed without melting in most cases, the decrease of melting temperature in nanoparticles (T_m) can contribute to the decreasing of sintering temperature compared with bulk sintering. Based on modified versions of the Debye model for size dependence of melting point [145, 146], it can be shown that the sintering of nanoparticles is enhanced by the suppression of the melting point T_m, which is reduced from that of the bulk material melting point (T_{mb}) by a factor as follows [147, 148]:

$$T_m = T_{mb}(1 - \frac{\delta}{D}) \qquad 2.15$$

where D is the particle diameter and δ is a material dependent parameter with reported values from about 1.80 to 2.65 nm for various metals [15], depending on the atomic volume and solid-vapor interfacial energy [148] (related to the bonding energy of the crystal structure). Thereby, the $T_m < T_{mb}$ for

nanoparticles contributes to a reduced sintering temperature. The other influencing factor α is usually selected to be 0.8 for bulk materials [149], ($T_s = 0.8T_{mb}$). However, the sintering of microparticles can proceed at 0.5-0.8T_m [150-152], while values of as 0.1-0.3T_m [150, 153] have been reported for nanoparticles and Monte Carlo and molecular dynamic simulation show even lower temperatures down to a few Kelvins [154-156]. The reduction of the influence factor from *0.8* to *0.3* is attributed to the larger driving force for nanoparticles as previously mentioned and further reduces the sintering temperatures.

The sintering process in nanoparticles begins with rapid neck formation followed by neck growth driven by surface diffusion, and then by vapour-condensation. Surface and grain-boundary diffusion are the two main mechanisms throughout the entire sintering process, although dislocations are present at the early stage of the sintering. Grain-boundary diffusion promotes the neck size growth [157] as illustrated in the numerical modeling results in Figure 2.17. Faster surface diffusion plus evaporation condensation at higher temperatures are also among the factors promoting faster neck size growth.

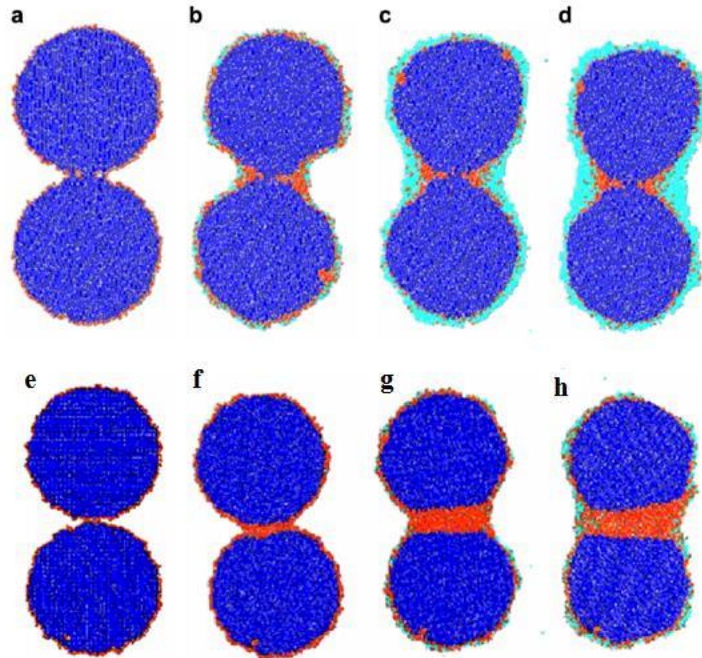

Figure 2.17 MD simulation of two large particles sintering at T = 63% T_m. (a-d) without grain boundary and (e-h) with grain boundary. Snapshots for the sintering process are t = 500, 50000, 200000 and 500000 steps. Every particle contains around 3000 atoms with bulk atoms (blue), surface or grain boundary atoms (red) and vapour state atoms (cyan), respectively. (reproduced from [157])

Currently, the sintering behaviors among individual spherical particles have been well established [158-162]. The above model only describes the sintering behaviors between spherical particles. However, materials with different shapes are rarely considered in studies of the sintering behaviors. Since other shaped materials, such as fibers, belts and disks [156], are different from the spherical case, it may not be suitable for them. Therefore, starting from a small scale, the study of nanosintering processes of different shaped nanomaterials could enrich the sintering theory.

2.2.3 Progress in Low Temperature Joining of Ag Nanomaterials

2.2.3.1 From Micro to Nano Pastes for Electronics Packaging

Since the late 1980s, electronics packaging has already employed Ag material pastes as a die attach material [163]. Usually, the weight percentage of the metallic particles in the paste has been 70% ~ 80% [164]. The rest is composed of organic solvents, dispersant and polymer-based binders to increase the material stability and processing ability. Rheology of the paste can be tuned by using different surfactants and particle sizes [165-168]. Binders and dispersants serve the same function of dispersing the particles and both terms have been often used interchangeably in literature [169]. They can prevent the agglomeration of particles in the paste but will also restrain the sintering. Therefore, the reduction of such organics can achieve lower sintering temperatures. Elevated temperatures are usually used to remove the organics during the bonding process. Their release can generate voids after sintering as well. Generally, sintering pressure, time, temperature, particle size and the surface condition of substrates could influence the joint properties significantly. However, large pressures, typically above 10 MPa [163], could be needed to achieve robust bonding, which may be unsuitable for practical applications. Hence, various research efforts have been conducted to reduce the sintering pressure during bonding processes.

It has been found that the surface diffusion coefficient increases with the decrease of nanoparticle (NP) size suggesting a higher specific surface energy of NPs than that of the micro-particles or bulk materials. Considering that the driving force for diffusion is inversely proportional to the size of the particles as mentioned in Section 2.2.2, a high driving force results in a decrease in sintering temperature of nanoparticles [170]. The suppression of melting temperature (as shown in Eq.2.15) and existence of a surface premelting layer (as observed with molecular dynamic simulation [148, 171]) will enhance the sintering of NPs. It also appears that smaller these NPs could be interconnected under lower external pressure since the stresses at contact areas increase with reducing NP size. Therefore, replacing micro-flakes with NPs will simultaneously induce low sintering

temperatures and required pressure, making low temperature joining feasible. For example, these factors may make it possible for significant sintering to occur at less than one third of the melting temperature of the materials, a temperature where traditional diffusion bonding of bulk materials is not normally feasible [150].

2.2.3.2 Application of Ag NP Pastes in Electronics Packaging

Currently, the leading application for sintered nanomaterial joints is for micro-electronic packaging. The performance of sintered nanomaterial joints can be affected by various parameters during bonding process, including temperature, time and pressure, and the qualities of nanopastes (such as organic content in the paste, size and shape of nanomaterials). Usually, appropriate sintering temperatures are chosen according to the application requirement and substrates used and the sinterability of pastes. These factors depend on the types and contents of organic binders and dispersant in the pastes, the different materials coated onto substrates and the materials of substrates (such as, Ag/Au/Ni coated Cu, bare Cu, or Ag/Au coated plastics [16, 17, 172-175]).

2.2.3.2.1 Influence of Temperature during joining

The elevated sintering temperature can produce higher strength of sintered nanomaterial joints due to more intense sintering between nanomaterials and nanomaterial to substrates. During initial development of low temperature joining technology, the sintering temperatures ranged from 250 to 350 ^{o}C since a significant amount of polymers were added into the pastes to improve the stability of nanopastes and coating properties on substrates. Sintering temperatures have subsequently been reduced to below 200 ^{o}C successfully after many efforts, as shown in Figure 2.18. For example, PVP coated Cu NPs were introduced into the paste to replace Ag NPs and achieved bonding at 170 ^{o}C [18]. An in-situ transformed Ag NP from the Ag_2O method has been invented by Hirose *et al.* [174, 176] in order to bond Cu substrates, in which the paste contained a large amount of organics to support the reaction of Ag_2O and this reduced the bonding temperature to 180°C. The organics in the pastes of the above two methods have been limited, thus further reducing temperatures. If the paste content incorporates less organics, the bonding temperature could decrease to 150 ^{o}C or even lower with further tuning of the particle size distributions, as demonstrated by Zou *et al.* [177] and Hu *et al.* [172]. Although increasing temperatures clearly enhance diffusional bonding, coarsening and coalescence of nanostructures also occur, which ultimately deteriorate the microstructure and disrupt the properties which are enhanced at the nano scale.

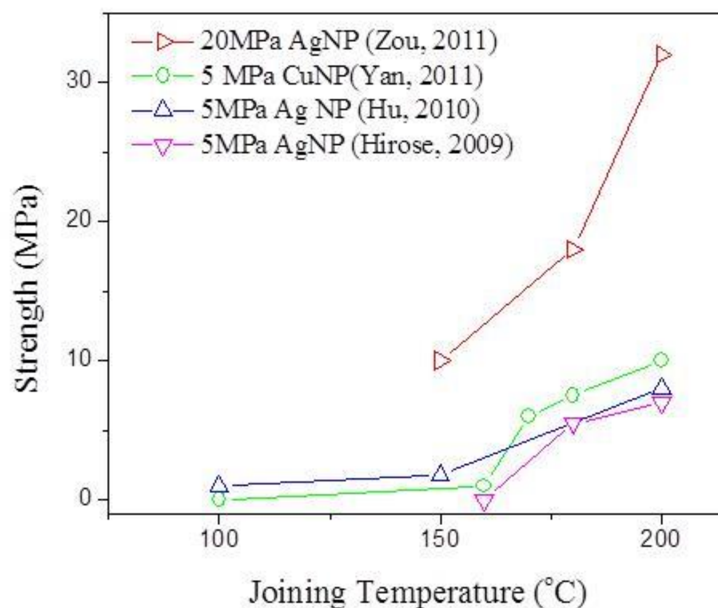

Figure 2.18 Strength of joints bonded at different temperatures. (data from [18, 172, 174, 177])

2.2.3.2.2 Influence of Time during joining

Time is another factor controlling the sintering process and will affect the joint strength eventually. At the same sintering temperature, longer sintering time could allow the organics or solvents to decompose and more nanoparticles interconnect with their near neighbors to increase the density of sintered nanomaterials and improve the joint strength. Figure 2.19 summarizes the joint strength recorded at various sintering times from a few seconds to 60 minutes. A nearly linear relation between strength and sintering time at 250 ^{o}C was reported by Hirose *et al.* [174] using in-situ formed Ag NPs, as open squares plotted in Figure 2.19. At same time, the coarsening of nanoparticles must be considered when the sintering time increases because grain growth instead of densification of sintered nanomaterials naturally leads to lower joint strength [169]. Herein, higher sintering temperature might be better to further improve the strength since it could help densify the sintered nanomaterials due to the grain boundary and lattice diffusion of interconnected nanomaterials, which are also referred to as densification mechanisms at higher temperature in the literature [169, 178]. For example, using an external pressure of 5 MPa at 200 ^{o}C, the joint strength increased from 28 MPa to around 35 MPa when sintering time was increased from 5 to 30 min [175]. However, when the temperature increased to 275 ^{o}C, 40 MPa was recorded after only 1 min of sintering at the same pressure [179].

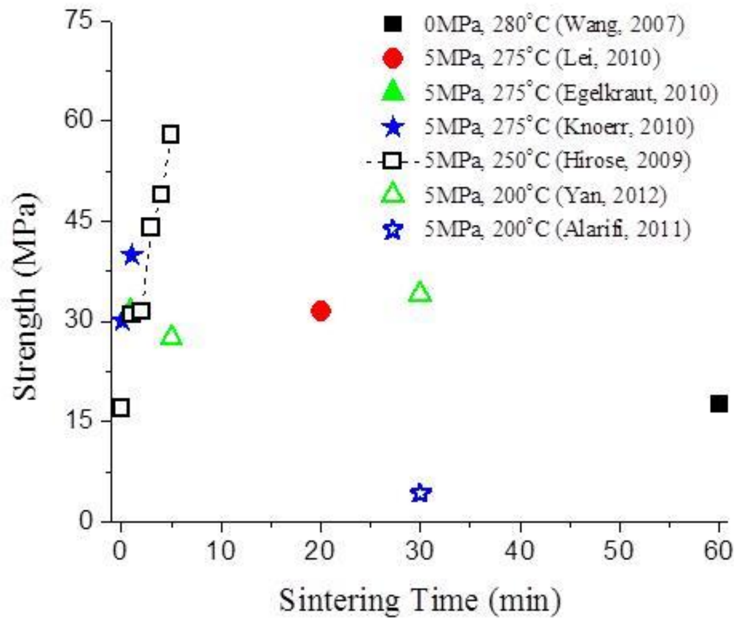

Figure 2.19 Strength of joints bonded with Ag nanomaterials at different sintering times. (data from [16, 174, 175, 178-182])

2.2.3.2.3 Influence of pressure

When the particle size decreases to the nanoscale, the sintering pressure between two contacting spherical particles will increase as suggested in Section 2.2.2. The application of external pressure during a sintering process could enhance this sintering pressure and also help densify the sintered nanomaterials and improve the joint strength. Figure 2.20 illustrates the influence of bonding pressure on the joint strength. From the work of Morita *et al.* and Yan *et al.* [175, 183], the strength exhibited a significant increase when the bonding pressure increased from 0 to 5 MPa at 250°C and 300°C. However, increases in bonding pressure to 10 MPa provided limited improvement in the strength [183]. This threshold bonding pressure of 5 MPa has been reported when the sintering temperature is 275 ^{o}C by Lei *et al.* as well [169, 180]. It has been found that this threshold pressure is also dependent on particle size [180]. However, a direct correlation between particle size and threshold pressure is difficult to establish by theoretical modeling since a wide distribution in particle size and irregular particle geometries in experimental studies complicate this issue. Although the bonding pressure has been dramatically decreased using Ag NPs instead of Ag microflakes, the ideal

pressureless bonding has been difficult to achieve in practical applications. By tuning the Ag NP surface conditions and organic contents in the pastes, pressureless bonding has been now demonstrated at low temperatures, which is very helpful for microelectronic packaging [175, 182, 184]. However, it is still a challenge to decrease the porosity of sintered nanomaterials and increase the coverage on the substrates to further improve strength and conductivity when no bonding pressure is applied.

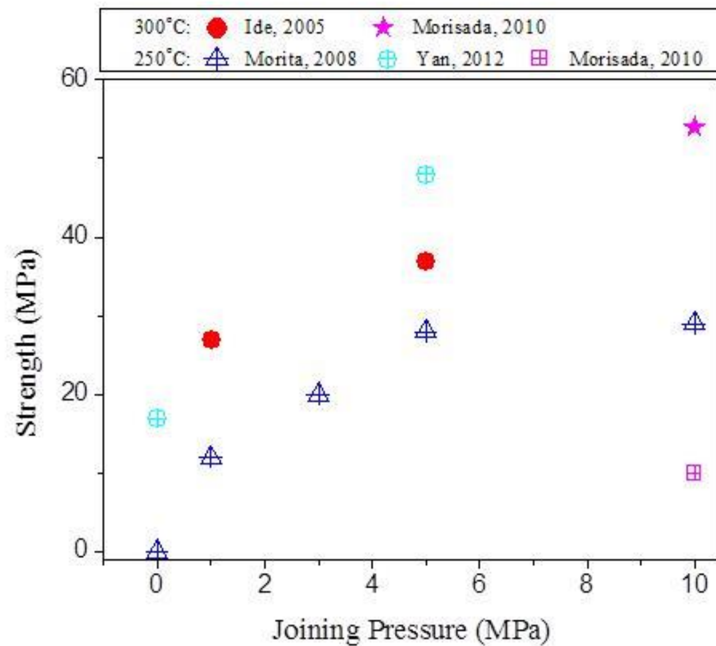

Figure 2.20 Strength of joints bonded at different external pressures. (data from [164, 173, 175, 183, 184])

2.2.3.2.4 Influence of particle Size

While the processing factors discussed above relate to the bonding process, the nanomaterials themselves also play an important role in nanosintering and bonding applications. The nanoparticle size is one of the main parameters to influence the joint performance. The particle size effect on the joint strength is demonstrated by Ide et al. [173] as shown in Figure 2.21. The smaller Ag NPs can produce higher joint strength because of higher sintering pressure and lower sintering temperature in general. The different packing density of Ag NPs with different sizes is another item that should be considered during nanosintering. Obviously, NPs with a broad size distribution could gain more dense packing and improve the joint strength as demonstrated by Morisada *et al.* [185] at 200°C and

300°C, respectively. In Morisada's study [185], three kinds of Ag NPs with mean sizes of 20 nm, 58 nm and 168 nm were mixed in different fractions: the joint using the trimodal mixture of Ag NPs achieved pressureless bonding with good strength. Thus, size distribution of NPs in the paste could be adjustable to improve the performance of sintered nanomaterials for low temperature and pressureless bonding applications.

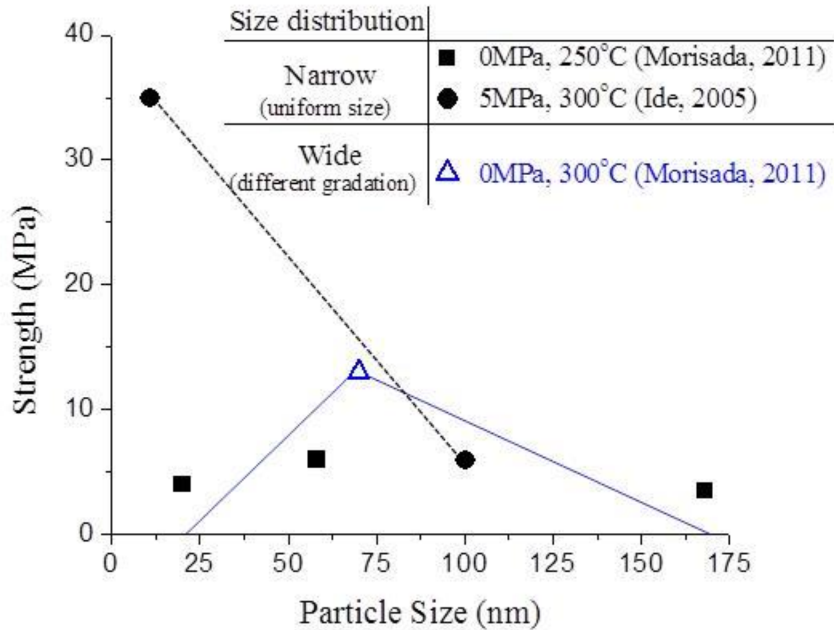

Figure 2.21 Particle size effect on the strength of sintered nanomaterial joins. Closed symbols indicate that the sizes are uniform in the pastes; Open symbols represent average sizes of nanoparticles in the pastes with different gradations and the size distribution is represented as a solid line covering a range. (data from [173, 185])

2.2.3.3 Chemically Activated Sintering at Room Temperature for Thin Films

Usually, a thin organic layer is coated on surfaces of nanomaterials to reduce oxidation because of the high surface energy when material size decreases to the nanoscale. This passive layer at the interface will restrain atomic diffusion. It is difficult to remove since the organic compounds are stable at room temperature until they are heated to their decomposition temperature or dissolved in certain solvents. Due to the high diffusion rate at the nanoscale, interdiffusion occurs automatically when two clean interfaces are brought into close proximity. This will promote room temperature joining when particle arrays are treated with different solvents to remove passive layers, as

demonstrated in Figure 2.22. At present, the solvents used in the reported methods involve two main categories, cationic polymers and electrolyte solutions. For example, poly-diallyldimethylammonium chloride is the one of the polymers used in Magdassi *et al.*'s study [186]. Solutions of NaCl, $MgCl_2$ and $CaCl_2$ were adopted to trigger the sintering of Ag NPs as well [187-189]. However, the mechanism for removal of organics in these solvents is unclear at this moment. In general, all these usable solvents contain Cl^{-1} to help desorption of protective organics on the surfaces. However, Cl^{-1} or other ions will also leaveresidue on the nanomaterials surfaces significantly influencing their chemical properties. Changes in the shape of Ag NPs may also occur after immersing them into solutions with high concentrations of ions. Further, this approach is not area selective since the entire surfaces would be exposed after removing the organics. However, it will be a potentially efficient and programmable method to fabricate conductive films or electrodes due to the complete removal of organics.

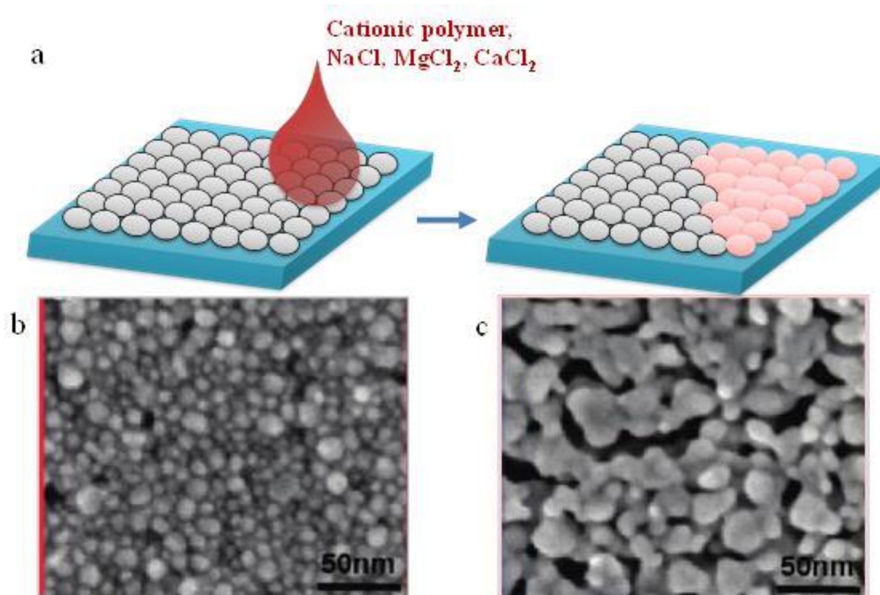

Figure 2.22 (a) Schematic illustration of chemically activated joining using cationic polymer or electrolyte solution. The microstructure of Ag NPs before (b) and after (c) applying cationic polymer. (reproduced from [186-189])

2.2.4 Joining of Ag NWs

At present, there are many attempts on joining of metal nanowires, such as end-to-end joining of gold nanowires by reflowing tin solder [7, 190, 191], butt or lap welding of platinum nanowires by Joule heating [192], end-to-side joining of gold nanowire with platinum-cobalt nanowire by tin-gold solder [6]. These methods all involved high heat energy and temperatures which can cause the melting of

nanowires or filler materials. Due to the nano size effect, the nanomaterial shape or surfaces will be more active during heating because of surface energy effects on the melting points and thermal sensitivity. During the heating process, it is difficult to maintain the original structure and shape of nanowires, especially when nanowires are melted. However, the shape and size of nanomaterials are two key factors which are vital for fully exploiting their properties. Thus, more precise and controllable low temperature or even room-temperature sintering or joining methods are required. As mentioned previously, when the interconnection area, the required energy for promoting diffusion to form atomic level bonds will be reduced dramatically. Therefore, only a small amount of energy is needed for joining two nanomaterials, and joining may even occur by surface diffusion without external energy to trigger. Recently, Lu *et al.* found that end-to-end joining of gold nanowires by oriented attachment at room temperature[11]. Here, two recently developed room temperature joining methods developed for silver nanowires are reviewed.

2.2.4.1 Optical Welding: Localized Plasmonic Heating

Light will induce heating of materials due to absorption of radiation, *e.g.* pulsed lasers with high energy density may induce rapid heating and melting in a short time. This energy source requires improve control for welding of nanomaterials. Recently, the use of a tungsten [9] or xenon [193, 194] lamp was demonstrated in fabricating large area transparent conductive thin films. Garnett *et al.* [9] explained this as a self-limited plasmonic welding method to create nanojunctions of Ag NWs, as shown in Figure 2.23 a-c. In this scenario, by using the plasmonic effect of silver, a low density of light will concentrate at the gaps between two adjacent nanoobjects, and these areas are referred to as hot-spots. This concentration of light can induce a high temperature locally without heating the surroundings as suggested in the simulated results in Figure 2.23d. Thus, local melting can occur and form metallic bonds at the interfaces, keeping the rest of the nanowires with their original shape. However, it is not an area specific method and joint quality will depend on the lighting time and light intensity, interface geometries and the separation distances between nanomaterials because of the limited size of the hot-spots. Nevertheless, selective plasmonic welding might be interesting for nanodevice fabrication in the future. Liu *et al.* [195] has reported that femtosecond laser induced plasmon excitation could be locally controlled in one single silver nanowire, in which local heat will be a useful source for controllable selective joining of individual silver nanowires.

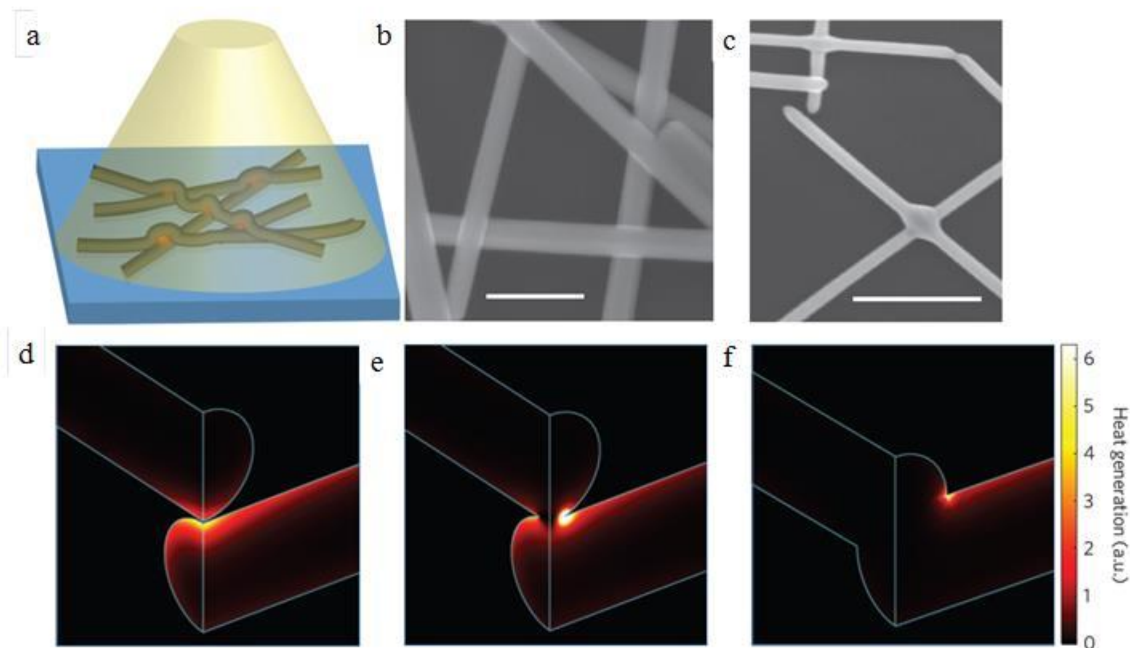

Figure 2.23 Optical nanowelding set-up and scanning electron microscope (SEM) images before and after illumination. Finite element method simulations of optical heat generation at silver nanowire junctions during the nanowelding process. (reproduced from [9])

2.2.4.2 Pressure Joining: Plastic Deformation

Plastic deformation has been used in joining of bulk materials during ultrasonic wire bonding [196], roll bonding [197], forge welding [198], and friction stir welding [199, 200]. However, these methods involve friction or severe deformation at the interfaces and generate extensive heat up to near the melting point of the material, which is difficult to control in the case of nanomaterials. Due the small interface of two nanomaterials, a small external force will produce large pressure for plastic deformation. If friction is absent, nanomaterials may join under such high pressure at room temperature. A simple approach has been demonstrated using this idea as illustrated in Figure 2.24. By applying a pressure of 25 MPa on the Ag NW thin film and holding only 5 seconds, these nanowires were crosslinked and formed junctions, showing an ultralow sheet resistivity [201]. In this study, the microstructure of local interfaces was not shown and the interconnection mode (metallic or mechanical) was unclear. Further, this is not an interconnection area specific approach since the external pressure is applied on a large area. Thus, selective joining using pressure induced plastic deformation will be another interesting topic needing to be studied.

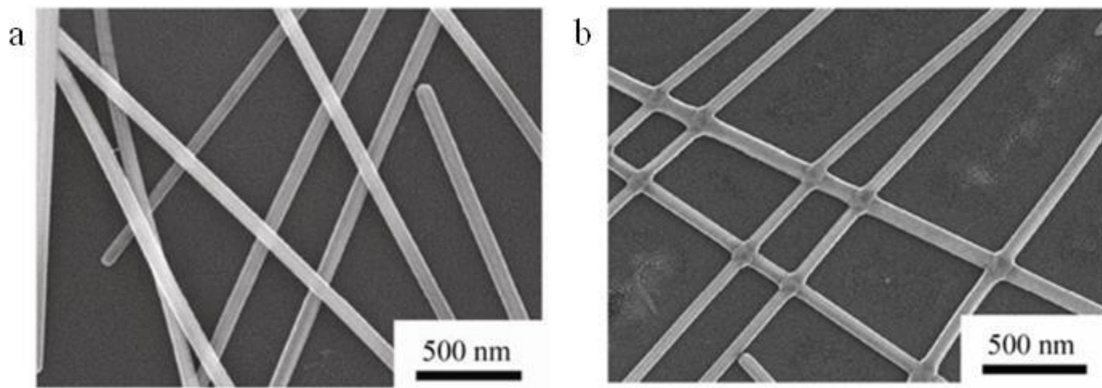

Figure 2.24 Ag NW film: before (a) and after (b) applying 25 MPa pressure for 5 seconds. (reproduced from [201])

2.3 Problem Summary

From above review, it can be found that previous research on low temperature joining process is mainly for nanoparticles rather than different shaped nanomaterials. The joining process is still with the assistance of external pressure (~5 MPa) and heat (~200 ^{o}C). The understanding of nano size effects on joining process is still incomplete, and it remains unclear whether the joining process can be completed without external pressure and heat. On the other hand, there are little published papers on mechanical behavior of silver nanoporous materials. The majority of research on mechanical properties of silver nanowire are based on tensile testing through in-situ SEM/TEM and molecular dynamics simulations, and three-point bending testing, which are all have their own drawbacks. At present, the mechanical properties of silver nanowires are focused on individual nanowires. There is very limited research on the practical application of them. In practice, their mechanical behavior under loading is still lacking of understanding. Therefore, more work on low temperature or even room-temperature joining of silver nanowires and their mechanical behaviors on loading are expected to be done in these areas.

Chapter 3
Joining of Individual Silver Nanowires*

3.1 Introduction

With the extensive study of nanoelectronic devices and nanoelectromechanical systems (NEMS), nanointerconnections have become a necessity for extremely dense logic circuits [11]. Bottom-up assembly of metallic one-dimensional (1D) nanostructure is one of the most efficient methods to construct nanocircuits. Silver nanowires (Ag NW) have attracted considerable interest because of their excellent electrical conductivity and mechanical properties. Although some methods such as soldering [6, 7, 191], voltage and/or current excitation [4, 192, 202, 203], thermal sintering [204, 205], electron beam irradiation [206-208], laser irradiation [209, 210] and plasmon interaction [9] have been successfully used to create nanojunctions, local heating of some form is a general feature of these nanoscale welding techniques. As the size range transitions to the nanoscale, an increasing surface to volume atomic ratio [211] in the nanostructured materials enhances their sensitivity to heat. However, local heating is often detrimental to the properties of the base material or damage the underlying substructures. In addition it is difficult to precisely control the application of heat at the nanoscale. Due to these limitations, joining of Ag NWs without heating is essential to engineer nanocircuits, and would be considered an attractive technical solution for the electronic industry. Lu *et al.* [11] has demonstrated cold welding of nanowires is possible by simply contacting two gold nanowires, such that surface-atom diffusion and oriented-attachment leads to successful welding. In the case of Ag NWs with highly oriented crystal structure produced by synthesis from a polyol solution [70], this joining mechanism is generally precluded due to the layer of residual polyvinylpyrrolidone (PVP) that remains on the surface of the nanowires, thus the spontaneous cold welding mechanism has not been reported for Ag NWs. However, if the protective organic layer is removed then one could readily achieve this oriented attachment and promote cold welding of Ag NWs if the surface is activated. This is mainly driven by the high surface to volume atomic ratio of the NW ends which enhances atom diffusion as shown in the simulated results of Pereira and da Silva [10].

In this study, nanojunctions between individual Ag NWs with five-fold symmetry are created by following the surface activation. Through high-resolution transmission electron microscope (HRTEM) and selected area electron diffraction (SAED), the phase relationship and joint formation

* Portions of this study also appear in: Peng, P., et al., Self-Oriented Nanojoining of Silver Nanowires via Surface Selective Activation. *Particle & Particle Systems Characterization*, 2013. **30**(5): p. 420-426.

mechanism between Ag NWs have been investigated. The phase orientation between the two Ag NWs in the joint has been analytically studied and explained based on the crystallography of the oriented nanowires. These self-oriented welded regions revealed that a similar crystal orientation is maintained between the nanowires, and the diffusion along the boundary contributes to the nanojunction formation. Those oriented joints could exhibit same strength and electrical conductivity as the rest of the nanowires [11]. These end-to-end Ag NW nanojunctions may be considered as having potential applications in the future nanoscale electronic circuits [212]. Further, these monocrystalline V-shaped or *zig-zag* silver prisms terminated by twin boundaries and free surfaces may be a novel structure for investigating the transport of electrons, light and vibrations in curved Ag NWs.

3.2 Experimental

3.2.1 Synthesis of Ag NWs

Ag NWs were prepared in a polyol solution with polyvinylpyrrolidone (PVP) as a structure directing reagent using a method modified from the literature [66, 67]. In this study, 330 mg polyvinylpyrrolidone or PVP ($(C_6H_9NO)_n$, K25, M.W.= 24000, Alfa Aesar) and 12.5 mg silver chloride (AgCl, Alfa Aesar) were mixed with 40 ml ethylene glycol (EG, Fisher Chemical) and was heated to 170 ^oC. Then, 110 mg silver nitrate was dissolved in 10 ml ethylene glycol and added into the mixed solution while stirring vigorously and continuing the reaction conditions for 1 hour.

3.2.2 Surface Activation Process

Three 10 ml as-synthesis Ag NW solutions were diluted to 50 ml using deionized (DI) water, ethanol and acetone, respectively. These diluted solutions sonicated for 5 minutes and centrifuged at 3000 rpm to remove the supernates and collect Ag NWs. This process was repeated twice.

3.2.3 Characterization of Ag NWs

Optical microscopy (Olympus BX 51M, Japan) and Field-emission scanning electron microscope (FE-SEM, Zeiss LEO 1530/1550 Gemini, Germany) were used to study the microstructure of washed samples. Organic shells of Ag NW before and after washing and the diffraction pattern of Ag NWs were observed using high resolution transmission electron microscopy (HRTEM, JEOL 2010F, Japan).

3.3 Results

3.3.1 Comparison of As-synthesized and Washed Ag NWs

The as-synthesized Ag NWs were 8-16 μm long as shown in the optical micrograph in Figure 3.1a, c with an average diameter of 100 nm. Before washing with deionized (DI) water, few V-shaped NWs (less than 1%) were formed. However, the V-shaped NWs increased significantly after washing (more than 50%) as illustrated in Figure 3.1b, d. It was interesting to note that most of them show V-shaped or *zig-zag* structures with approximately 2 to 4 straight NW segments joined at similar angles. Therefore, it suggested that joining of few individual Ag NWs together at room temperature by washing process resulted in these V-shaped and *zig-zag* Ag NWs. Since the ends of most NWs are not flat, the straight bonding may not be a stable configuration. The long Ag NW was not because of joining but a single Ag NW from synthesis process. Various washing processes, such as using acetone or ethanol, resulted in the same Ag NWs joints as those produced by washing with water (arrows indicated in the SEM micrographic of Figure 3.2).

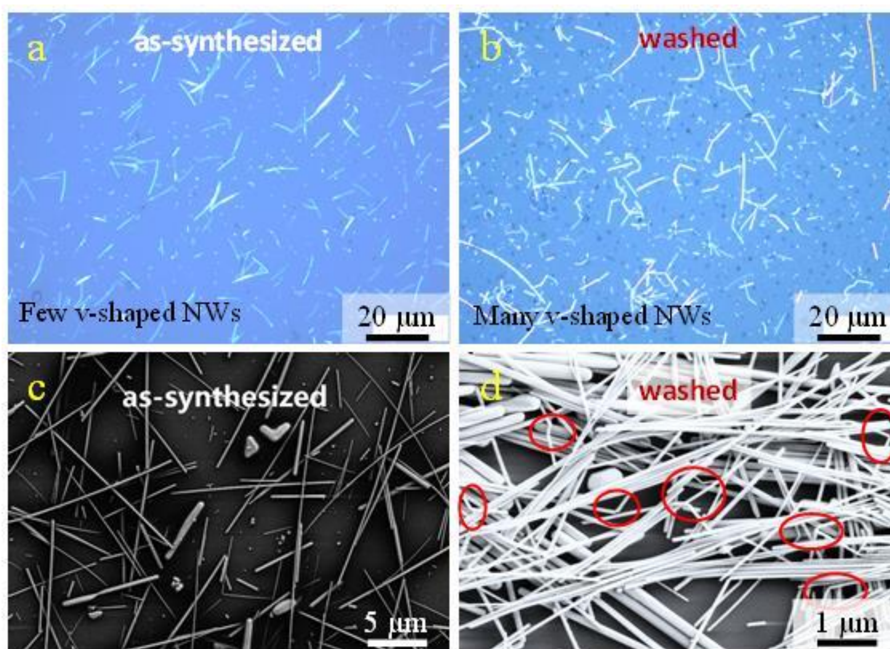

Figure 3.1 Optical and SEM micrographs of (a,c) as-synthesized and (b,d) washed Ag NWs, illustrate that the V-shaped and *zig-zag* Ag NWs significantly increased after washing.

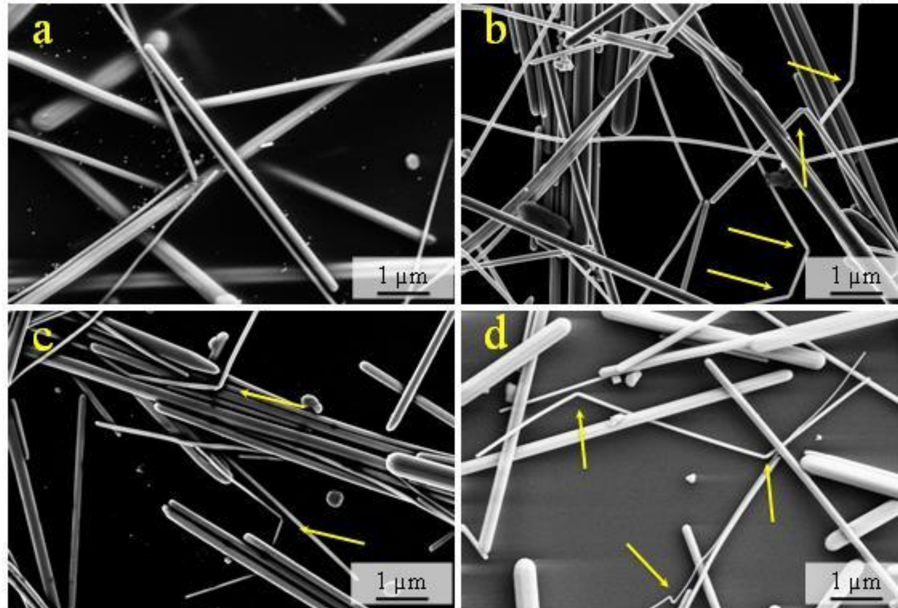

Figure 3.2 SEM images of (a) pristine Ag NWs in EG and after washing with (b) water, (c) acetone and (d) ethanol.

3.3.2 Effects of Ultrasonication and Centrifugation

To check if ultrasonication may contribute the energy input and form V-shaped NWs, the controlled experiment with different ultrasonication time and level was conducted, see Figure 3.3. It could be seen that the proportion of V-shaped NWs did not show significant variation. Therefore, the ultrasonication time and level did not largely promote nanojoint formation because the contact opportunity between nanowires was quite low. However, the nanojoints could be widely observed in the separated nanowires after centrifuging. Considering nanowires are separated from solution and gather together on the bottom of tubes, the contact opportunity of these nanowires dramatically increased and it might be one of the key parameters to control the joining. If nanowires have been separated from solution, the centrifuge time and speed also have no strong relation with joining proportion. It is worth noting that external pressure during the centrifuge process might promote surface atom diffusion once two wires contacted. Even though the external force acted on each nanowire is very weak, the stress/pressure is quite high because of the small contact area at the nanowire interfaces between two ends in contact. Therefore, this immense stress localization created between the ends of the nanowires during centrifuge process might be a considerable point for the nanojoint formation in this case. These points will be discussed in a later section.

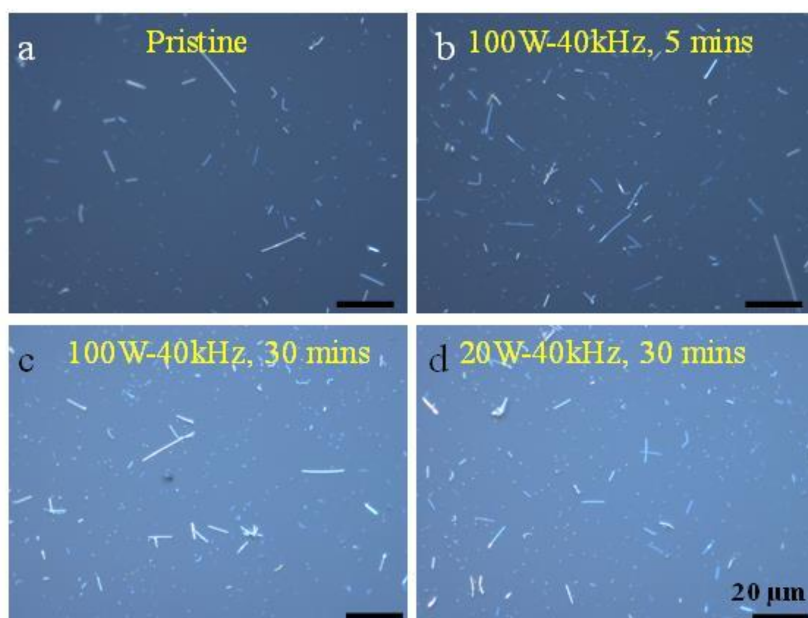

Figure 3.3 Optical images of Ag NWs after ultrasoncating with different time and energy. (a-d scale bars are 20 μm)

It was observed that most of the wires were joined during the centrifuge process due to the increased contact opportunities. Considering the nature of centrifuge process, wires with different size could be gradually separated from the solution if given a similar length of nanowires, around 10 um in this study. There is a higher probability that wires with similar thickness will have more opportunities to contact with each other, leading the V-shaped/ *zig-zag* nanojoints formed between wires in similar thickness, see Figure 3.4a. However, the configuration of thin nanowire to thick nanowires was observed as well even this was quite rare, Figure 3.4b.

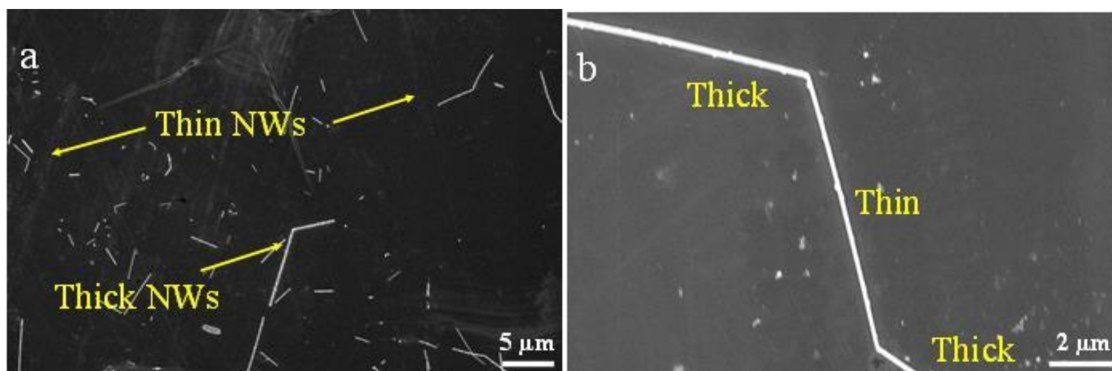

Figure 3.4 SEM images of V-shaped NWs formed (a) between two thin or thick NWs; (b) Thick NWs to thin NW.

3.3.3 Joint Selection

It was found that every part of the V-shaped NW was with the similar length as synthesized NWs by measuring the length of NWs. There were few defects, for example stacking faults, within the junction region according to the observation under TEM (this will be shown in details later), indicating it was not a deformed NW but joined. Usually, the deformed structure would prefer to show one continuous curve as the outer surface of NW indicated in Figure 3.5a. However, two severely curved surfaces with V-shaped notches in the NWs further suggested that they were not deformed by bending, see Figure 3.5b. Thus, it was believed that the majority of these V-shaped or *zig-zag* Ag NWs was not formed by bending but by joining. During angle measurement, those NWs with sharp corners as illustrated in Figure 3.5b were considered.

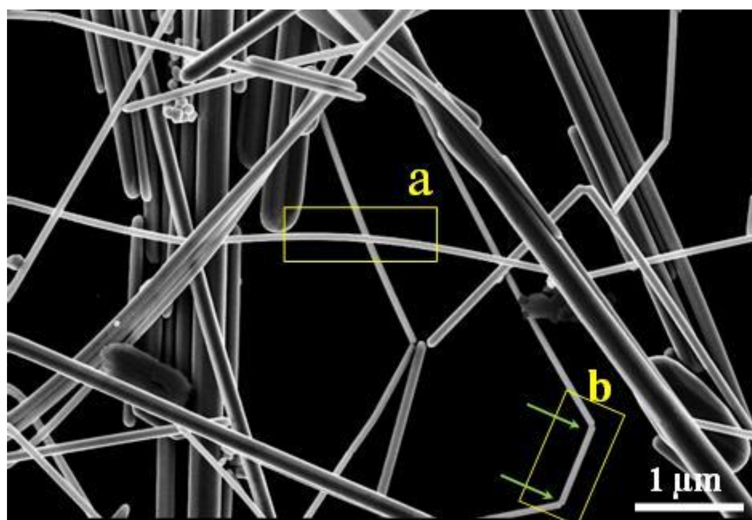

Figure 3.5 Difference of (a) bending with one continuous curve, and (b) joining with sharp corner and two curved surfaces with small V-notch.

3.3.4 Angle Measurement and Distribution

To make sure the measured angle of joints was close to the actual angle, those v-shaped NWs laid flat on the substrates and not intersected with others were selected. Thus, the concentration of NWs on substrates was very low for measurement in this case. Large portions of NWs in optical images laid flat on the substrate, making the angles were easy to measure. In addition, optical microscope might be better for counting angels because it has larger visual field than SEM. Therefore, most of those angles in this study were measured using optical images (500+ measurements in total). To investigate whether the V-shaped or *zig-zag* Ag NWs observed in optical

microscope (OM) could have different angles under SEM because of the diffraction limit of optical microscopy, the same nanowires were observed and measured in both SEM and OM. The results were compared and confirmed no difference for angle measurement as shown in Figure 3.6 (all compare results are listed in Table 3.1). It suggests that even the diameter of the nanowire in optical microscopy is several orders larger than its actual size, the angles between nanowires measured in optical microscope are the same as in SEM. Therefore, it is believed that the angle distribution measured under optical microscope is precise and truthful.

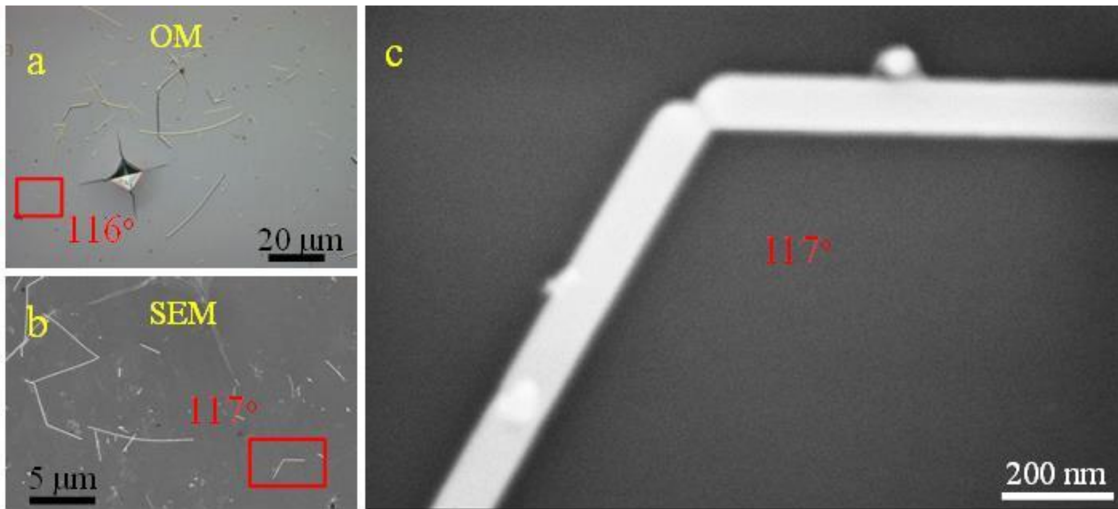

Figure 3.6 (a) Optical and (b) SEM micrographs of a bonded V-shaped Ag NWs (with 117° angle) laid flat on Si substrate. (c) High magnification of the V-shaped Ag NWs with two curved surfaces and a V-shaped notch in the joint region.

Table 3.1 Measured angles of exactly the same Ag NWs with optical microscopic image (OM) and SEM image (SEM)

	Measured Angles (^{o})															
OM	126	119	119	116	137	141	124	143	131	97	127	123	127	128	113	133
SEM	128	120	118	117	137	141	122	141	135	96	128	118	129	129	109	135

When the angles of joints are plotted as a function of the frequency as shown in Figure 3.7a, the distribution of angles concentrates in a narrow range of 121 to 130°. The typical morphology of such Ag NW joints is illustrated in the TEM micrograph in Figure 3.7b, where an angle of 125° is

observed. It is worth mentioning that the interior angle of the joint is sharp, because there is a large driving force for diffusion due to the high surface energy present at this location, while the outer surface has a larger radius or curved structure because the driving force for diffusion is low. This further supports the idea that these are joined, and not deformed wires because the outer surface of a deformed wire would be one continuous curve (not two curved surfaces as shown in Figure 3.7b). These structures differ from the previously reported V-shaped Ag NWs which formed due to twinned crystal plane induced growth and crystal lattice match induced fusion during polyol-thermal synthesis process [212, 213]. It should be noted that these nanojunctions were formed at room temperature after the washing process without any heat input.

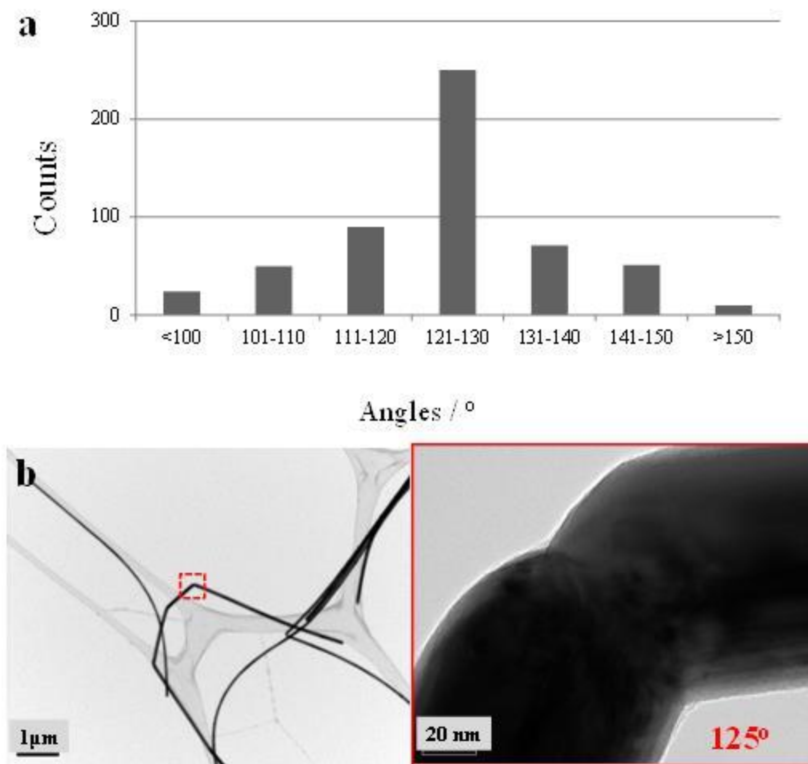

Figure 3.7 (a) Angle distribution of Ag NW joints. (b) TEM images of typical Ag NW joints.

3.4 Discussion

3.4.1 Selective Surface Activation

For *fcc* metals, surface energy of different faces is uniform, and mainly depends on the variable density of atoms on each face [214]. In terms of silver, the surface atom density between the {100} and {111} planes is 1.2×10^{19} *vs.* 1.38×10^{19} atoms/m^2, respectively [215]. Consequently, the relative surface energies of the low-index crystallographic planes are $\gamma_{111} < \gamma_{100}$. Due to the stronger interaction between PVP and {100} facets than that between PVP and {111} facets resulting from the higher surface energy, it functions as a structure directing reagent on the surface of Ag nanomaterials during synthesis. Xia and co-workers identified that the end of Ag NW with five-fold cross-section is covered by {111} facets and with sides corresponding to {100} facets[67]. The weak interaction of PVP with the end facets of {111} leads to the higher chemical potential and reactivity on the ends, while the adsorption of PVP on side surfaces of {100} is very strong and results in complete coverage [66]. TEM images in Figure 3.8a&b support this notion, and demonstrate that the organic shells have a 2.5 nm and 5 nm thickness on the ends and sides of as-synthesized Ag NW respectively.

Once these Ag NWs intersect, this organic layer originating from the synthesis process could be presented at the interfaces of the nanowires and influence the interdiffusion of atoms to facilitate joining of Ag NWs without assistance of external energies, such as heat and pressure. Although the PVP absorbed on the surfaces of Ag NWs does not readily decompose at below 300 ^{o}C [216, 217], the majority of this organic compound would efficiently be removed during the process of washing with DI water. Figure 3.8c&d indicate the organic shell reduced to 0.5 nm on the end and 2 nm on the side of the Ag NWs after washing. Meanwhile, some areas on the ends of Ag NW were completely devoid of organic coating as indicated in Figure 3.8c. These bare sites provide excellent interdiffusion channels between two NWs in contact in an end-to-end manner, which will promote spontaneous cold joining of Ag NWs due to the high driving force for surface diffusion at the nanoscale. It worth noting that external pressure during the centrifuge process might promote surface atom diffusion once two wires contacted. Even though the external force acted on each nanowire is very weak, the stress/pressure is quite high because of the small contact area at the nanowire interfaces between two ends in contact. However, the removal of PVP on the sides of Ag NW was not significant and the relatively thick organic layer (compared to the ends), would likely inhibit formation of a T-shaped joint (end-to-side). This suggests that the ends of the Ag NW have been selectively activated for joining at room temperature and while keeping the rest of nanowire still

protected. This selective activation process is associated with washing and the specific facets (111) of Ag NWs, indicating that it is not random but self-selective due to matching of crystal structures at the ends of nanowires.

It is worth noting that long polymer chains, PVPs in this case, graft on the surfaces of the nanowires and their presence could introduce repulsive secondary bonding forces between the two counterparts as demonstrated during Ag nanocube assembly [218]. These forces would lead to a gap on the order of few nanometers between the nanowires, impeding Ag atom diffusion as schematically shown in Figure 3.8e, since this gap is too large to facilitate the transfer of surface atoms and complete the diffusion process. The adsorption of polymer on the Ag surface also lowers the surface energy, leading to an increase in the activation energy of surface atoms [219-221]. Further, the residual polymers present in the gap between the nanowires could block the diffusion channels [222, 223]. However, if only a small fraction of the polymer material remains on the surface, the repulsive effect is reduced and the nanowire separation distance is much closer. Meanwhile, compared with large fraction, a small concentration of polymer could provide higher surface energy and lower activation energy of surface atoms to promote interdiffusion. Consequently, it promotes accelerated bonding between two surfaces and allows two Ag NWs to easily form metallic bonds at room temperature.

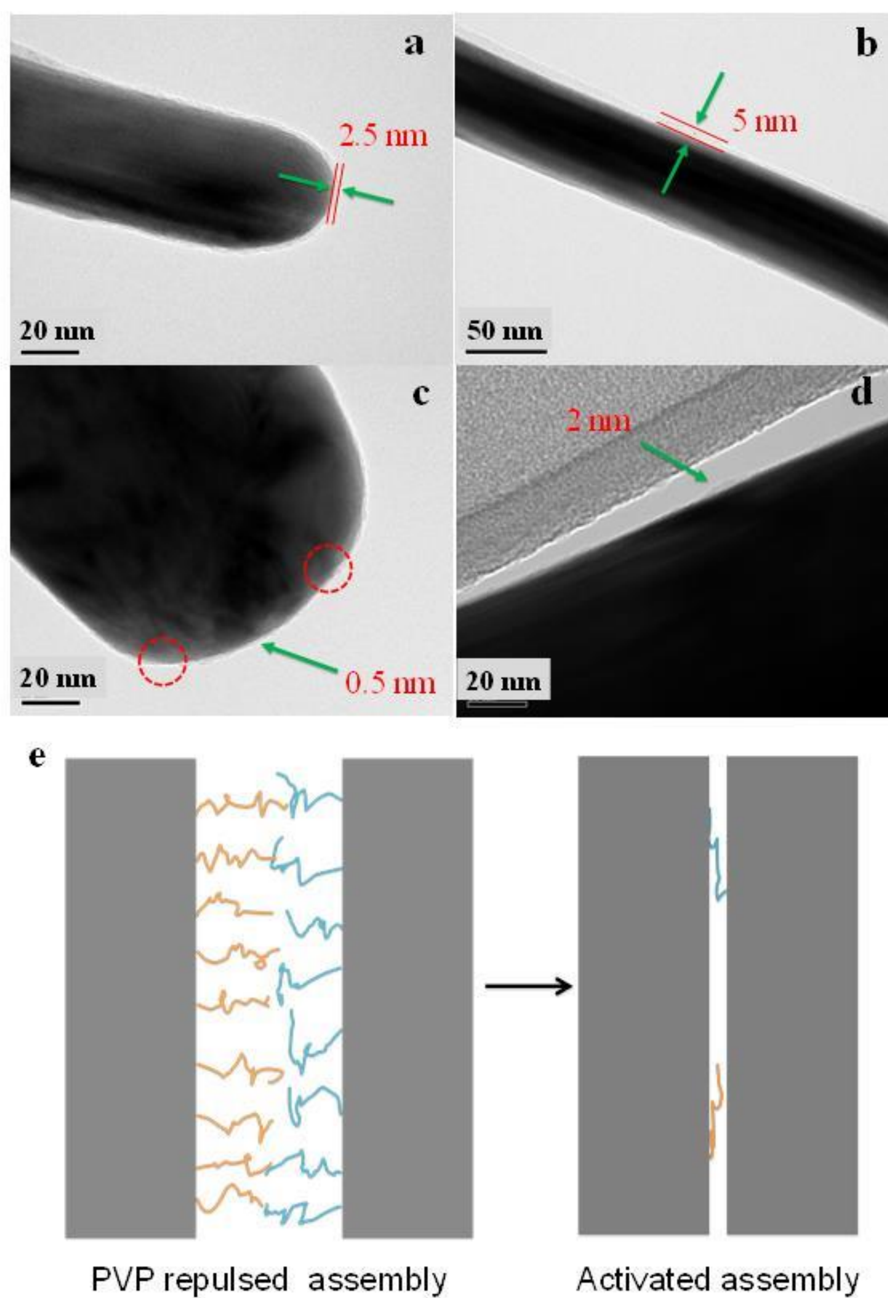

Figure 3.8 TEM images of the end (a) and side (b) of pristine Ag NW; (c) and (d) washed Ag NW. Some areas on the end of Ag NW were exposed without organic coatings as highlighted in the circles in (c). Te breakage on the side of Ag NW is not significant in (d). (e) Schematic of assembly of Ag NWs by modifying the surface of NWs with polymer chains grafts of different chain densities.

3.4.2 Phase Relationships of Joints

To understand the joining mechanism, HRTEM and SAED analysis were employed. Figure 3.9 illustrates the TEM images and SAED patterns of one joint, where an angle of 126° is presented between the joined wires. The SAED pattern of upper wire shows the incident beam was on a [011] zone axis and the NW is twinned on the {111} plane with a 39° twining angle, see Figure 3.9b. Measuring from a [110] orientation, the angle between two (111) planes along twinning boundary is 70.53^{o} [224], yielding the complementary angle of two twinned planes is 180° - 2$\times$70.53^{o} = 38.94^{o}, which is the observed twinning angle 39° through the diffraction patterns on the [011] zone axis. The measured angle between $(1\bar{1}1)$ and $(\bar{2}00)$ planes (or {111} and {100}) is 125°, which is in close agreement to the theoretical value of 125.26^{o}. The diffraction pattern of bottom wire is illustrated in Figure 3.9c. The length of index vectors shows that A/C=1.95 and B/C=1.65, indicating it is on the $[\bar{1}12]$ zone axis. The measured angle between $(\bar{2}\bar{2}0)$ and $(\bar{1}31)$ planes is 31° and in close agreement with the theoretical value of 31.48^{o}, while angles between $(\bar{3}\bar{1}\bar{1})$ with $(\bar{1}\bar{3}1)$ and $(\bar{1}\bar{3}1)$ with $(1\bar{1}1)$ are 82° and 59°, respectively.

It is noted that there is also a group of weak diffraction spots indexed as [011] zone axis in Figure 3.9c. By rotating this set of spots by 55°, these are found to coincide with the [011] zone axis spots in Figure 3.9b. Moreover, the [110] direction has a 54.74^{o} angle with [211] direction, *i.e.* an angle between $(\bar{1}10)$ and $(\bar{1}12)$. It is suggested that the two wires have the same orientations according to the diffraction patterns. In the other words, the bottom wire could be considered as rotating the top wire by 55° in-plane, which the angle is the difference between 180° and 55°, yielding the angle observed at the joints, 125°. Some slight deviation of the measured angle is due to the error of measurement and a result of viewing angle variation. The diffraction patterns for the jointed region are shown in Figure 3.9d, and it can be separated as two individual sets of spots, one from the top wire [011] zone axis and another for bottom wire $[\bar{1}12]$ zone axis. The HRTEM image of the joint taken from the interior angle illustrates two Ag NWs connected without any gaps, see Figure 3.9e. The lattice fringes indicate there is a 125° angle between (111) and (200) planes. Since its counterpart is not on the same zone axis, its lattice could not be revealed. Similar results were characterized in detail for another joint and shown in Figure 3.10.

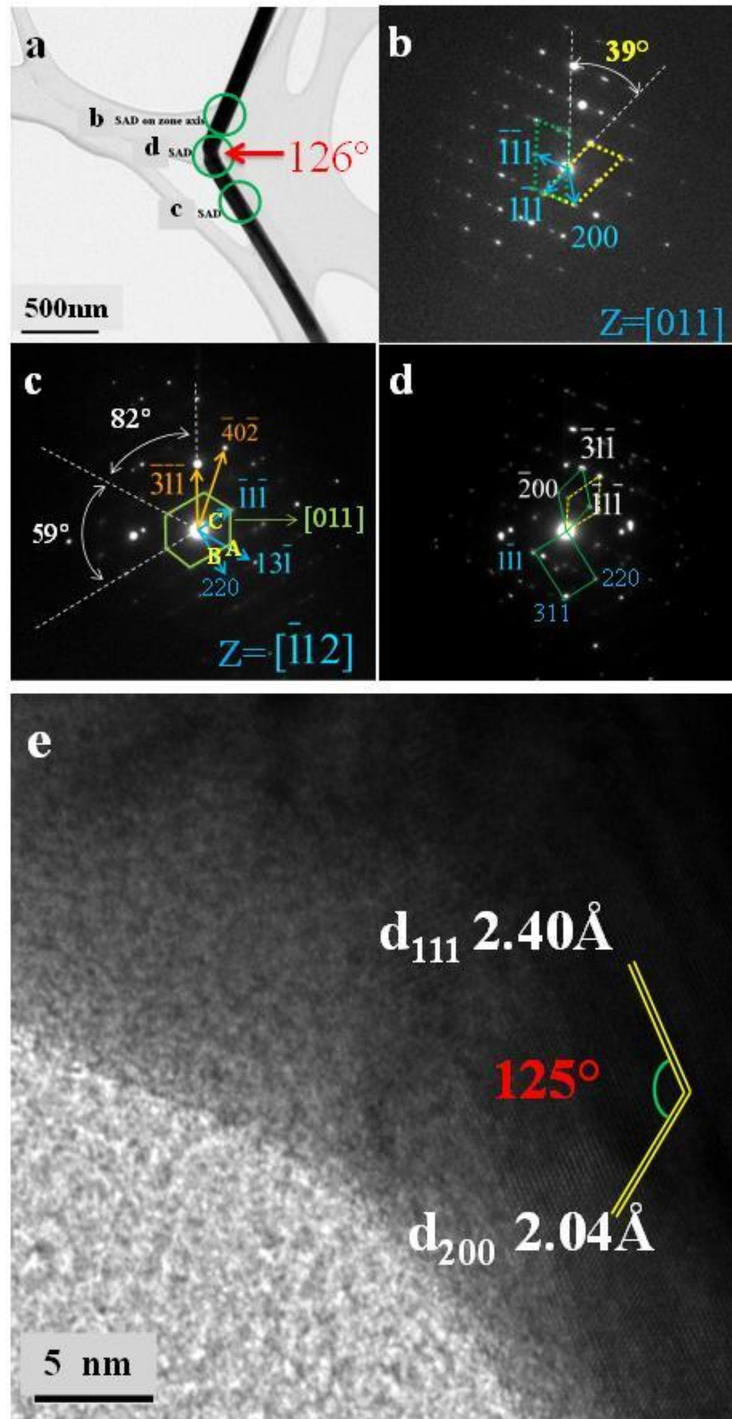

Figure 3.9 (a) Ag NW joint with 126° angle: the SAED patterns on (b) upper wire with [011] and (c) bottom wire with [$\bar{1}$12] zone axis, (d) right the joint region. (e) The HRTEM image of inner angle of the joint.

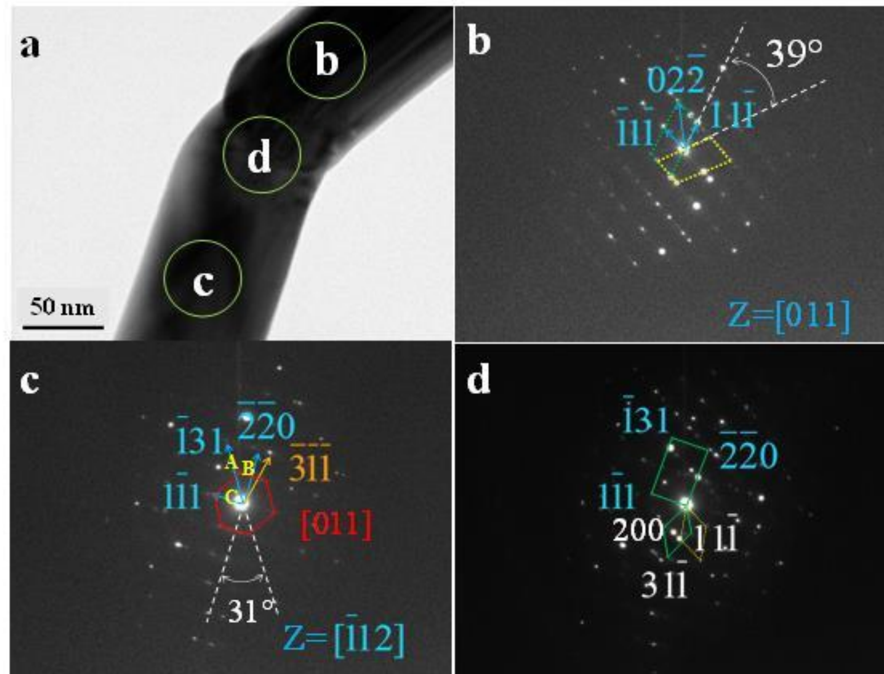

Figure 3.10 A typical joint of end-to-end Ag NWs: (a) TEM image of joint with a 126° angle; the SAED patterns of (b), (c) and (d) corresponding to two wires and joint shown in (a).

The joints with smaller angles were also investigated to determine the orientation relationships of these joints, such as 115° as depicted in Figure 3.11a. Figure 3.11b-c shows the diffraction patterns corresponding to the [011] and [$\bar{1}$12]/[011] zone axis as previous observation. Figure 3.11e displays the lattice fringes of the joint taken from exterior angle region, showing distances of the (111) planes from two Ag NWs were 2.4Å and connected with a 10° misorientation. The dashed circle highlights the defect contrast due to this misorientation. This 10° misorientation has also appeared in diffraction patterns of the joint region as shown in Figure 3.11d. As indicated in the angle measurements in Figure 3.7a, joints usually exhibit angles between 121 -130°. Here, the measured angle of two Ag NWs 115° in Figure 3.11a corresponds to a misorientation angle 10° away from the 125° angle expected between the orientation relationship proposed here. Therefore, it suggests that the joints were formed by connecting two Ag NWs through lattice matching on (111) planes. Further, the misorientation accounts for the fluctuating angles of these joints, in the range of 115 to 135°, as the statistical results suggested (see Figure 3.7a). The interfaces within 10° misorientation are low angle grain boundaries, resulting from the grain boundary diffusion in conjunction with surface diffusion which dominates during joining. One could speculate that the two

wires tend to be self-oriented to strive towards lattice matching on (111) planes during these diffusions.

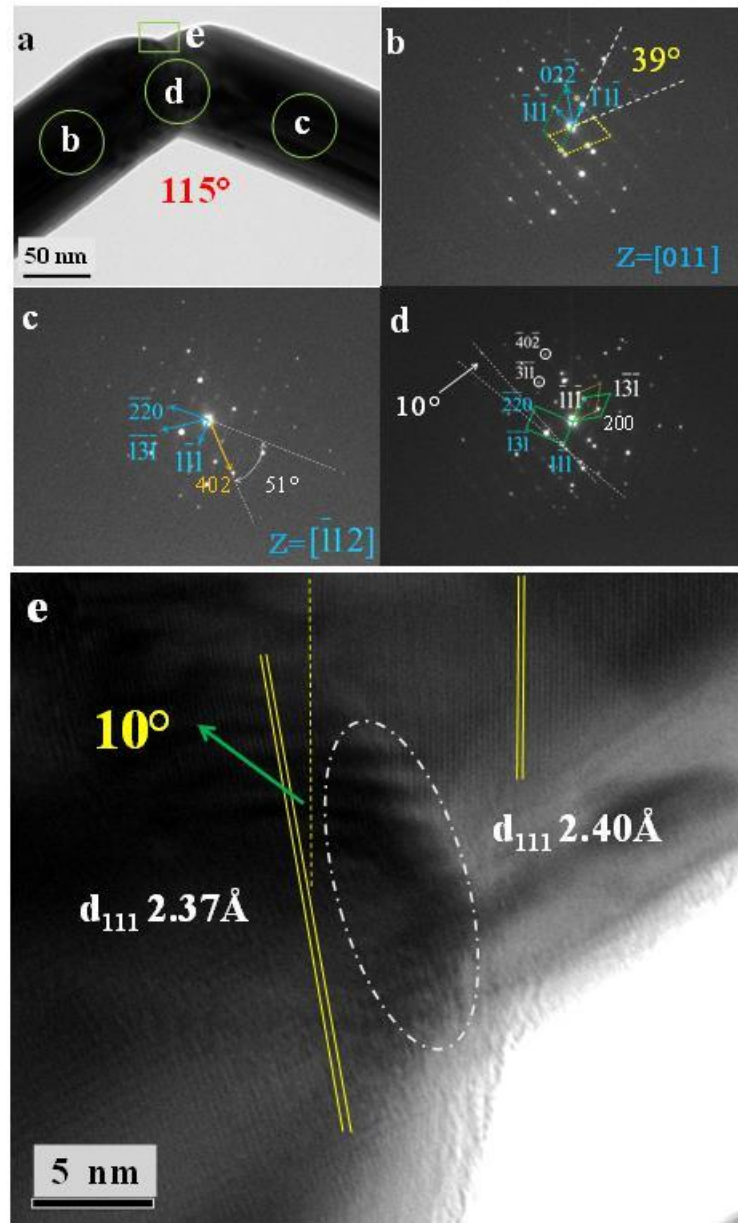

Figure 3.11 (a) Ag NW joint with 115° angle: the SAED patterns on (b) left wire with [011] and (c) right wire with $[\bar{1}12]$ zone axis, (d) right the joint region. (e) The HRTEM image of exterior angle of the joint, the (111) planes belong to two Ag NWs were matched with 10° mis-orientation. (The dashed circle indicating the contrasts from defects because of the mis-orientation).

3.4.3 Joining Mechanism: Self-Oriented Nanojoining

Low stacking fault energy of silver materials promotes the crystal growth in nanosize, as a result of twins [225]. In the case of Ag NWs, the twin boundaries run along the entire wire, and the Ag NWs with five-fold cross-section could be considered as five highly orientated single Ag crystals ("triangular prisms", highly oriented nanoscale grains) [226]. Each single prism is coherently twinned with another on the (111) plane and the end is covered by {111} facets. Joint formation has taken placed on these two {111} facets of the end of Ag NWs, see Figure 3.12a. Here, the joint was actually formed by the end of two single triangular prisms, and each of them was from the two joined wires. Since the extremity of the triangular prisms were (111) plane, the joint interface was $(111)_{NW1}//(111)_{NW2}$, or sometimes with a less than 10° mismatch. Therefore, a cleaned surface and identical lattice orientations are required for self-oriented joining of Ag nanowires at room temperature.

Considering the angle between {111} facets (on the end) and the axis of the NW is 54.74^o, the self-oriented joined NWs will not be straight. If two NWs connect with alignment such that the centres of the pentagonal shapes (as labelled with red color region in Figure 3.12a) come into contact, then the angle between two joined NWs with same orientations would be $2\times54.74^o=109.48^o$. This is an unfavourable angle as suggested in Figure 3.7a, and was not observed by TEM. It is worth noting that the centre point of the NW is the intersection location of the five twin boundaries, suggesting it is a high energy site as well. To minimize the energy of the system when two NWs contact, the edge-to-edge configuration would be not preferred compared to centre-to-centre configuration. Actually, these two configurations would be the same if two NWs have the same diameter, which would have low possibility in reality. Conversely, "centre-to-edge" configuration of two NWs will allow the (111) lattices to easily match by NW rotation when the two end facets are not same size (two NWs with different diameters) and introduce more contact edge sites between two NWs, yielding much larger diffusion rate because the curvature of the NW decreases from the edge to the centre, see Figure 3.12b. In this case, centre-to-edge configuration could obtain around 50% higher energy edge sites than that of centre-to-centre configuration (with the as assumed angle configuration), as red dashed lines indicated in Figure 3.12b, leading to faster diffusion and nanojoining between centre-to-edge aligned nanowire ends.

According to the lattice orientation relation of two Ag NWs, the atomic arrangement of the joint is reproduced in Figure 3.12c. The atomic arrangement indicates that the lattices of two joined "prisms" are well orientated and lattice matched. On each wire, the sides are terminated with a

coherent twin boundary and free surface, respectively. It suggests that this joint creates a V-shaped prism with a monocrystalline structure. It is well accepted that the properties of crystals could be influenced by defects such as such as grain boundaries and free surfaces. Here, the same orientated V-shaped joint with two boundaries, a coherent twin boundary and free surface, may be a novel candidate to investigate the homogeneous transport properties in nonlinear Ag NWs, for example light/wave guidance and electronic transport of these joints. Furthermore, it has been shown that twin boundary within the NW for *fcc* structure could produce anomalous strength and brittle fracture under loading because the five twin boundaries in this type of NW were intersected with all of the possible slip systems in *fcc* structure and the motion of dislocations is restricted by the twinning boundaries [227, 228]. Consequently, they are effectively grain boundary hardened materials [226] while these Ag NW joints with same orientations will be expected to gain good mechanical properties as that of original individual Ag NW.

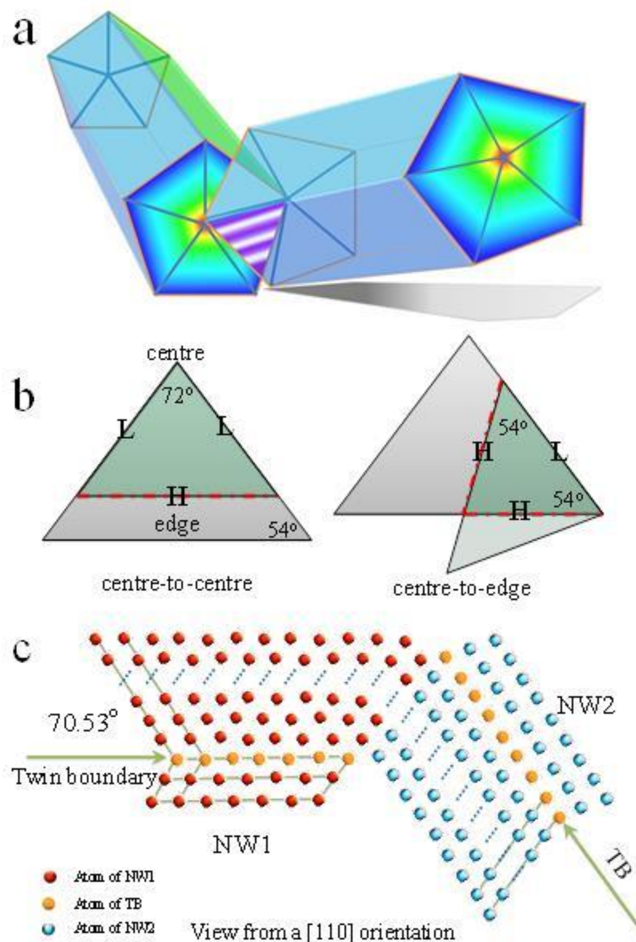

Figure 3.12 (a) Schematic illustration of end-to-end Ag NW joint, the cross-section of Ag NW is five-folded. (b) Two facets with different sizes attached via centre-to-centre and centre-to-edge configurations, letters H and L denote high and low diffusion sites belonging to different locations of Ag NWs. (c) The atomic arrangement of Ag NW join, when view from a [110] orientation that is on the coherent twin boundary with 70.53° angle of *fcc* Ag.

3.5 Summary and Remarks

In summary, the joining process and mechanisms during room temperature joining of individual silver nanowires due to nano size effects have been presented in this chapter. A repeated washing process was used to remove organics from the nanowire surfaces and selectively activated the surface of the silver nanowires. This provided an interface free of contamination which enhanced surface diffusion for nanojoining of silver nanowires end-to-end at room temperature.

Characterization of the joints by high resolution electron microscopy has revealed that a similar crystal orientation was maintained between the nanowires and diffusion along the boundary contributes to the nanojunction formation. A monocrystalline V-shaped or *zig-zag* silver prism was formed after nanojoining, terminated by twin boundaries and free surfaces. The simple selective activation process for nanojoining has potential applications for engineering electronic circuits, and may represent a useful structure for investigating the transport properties of electrons, light and vibration in bent silver nanowires.

This chapter has demonstrated that the end surface of Ag NWs could be activated with the removal of the thin layer of PVP. These activated end surface would be ready for room temperature joining due to nano size effect without external heat input; however it is only the small portions of the entire surface of Ag NWs. The dominant side surface of Ag NWs is still difficult to activate. If the organic layer on the side surface of the Ag NWs could be break down, the activated sites will increase dramatically and raise the room temperature joining possibility subsequently. The formation of end-to-side or side-to-side joining of Ag NWs will be able to push them into practical applications for nano-circuits or lead to new applications. For example, largely activated surfaces of Ag NWs could make three-dimensional networks feasible. These networks own excellent conductivities of silver and good thermomechanical properties due to their porous structure. They may join with other metals at a nano scale at room-temperature as well. These can make the silver nanowire networks as a good interconnector candidate for flexible electronics benefitting by low processing temperature and good thermal, electrical, mechanical properties. This study will be presented in next chapter.

Chapter 4

Joining Using Silver Nanowire Pastes[†]

4.1 Introduction

The atomic level interconnection of components to achieve metallurgical bonds is a key requirement for micro/nano-electronic devices since conductive joints are needed in transistors [229-231], sensors [232, 233], solar cells [234, 235] and display units [236-238]. Conventionally, external energy inputs are needed to accelerate diffusion and mixing of atoms at the interfaces for metallic bond formation. These excitation energies are generally applied through external sources during soldering & sintering [130, 173], laser welding [2, 239, 240], resistance welding [241], friction welding [242, 243], microwave sintering [244], pressure welding [245, 246], and delivered to the interfaces where connections are required. Generally, the interfaces are mostly in bulk size and the energy requirements are large in these conventional joining processes. Thermite welding is one category where heat is generated in-situ by an exothermic reaction, however the process results in high temperatures which also melt the bulk material. When the device and joint size reduce to micro- and/or nano-scale, the energy delivery should be more precise, efficient and controllable. Meanwhile, some drawbacks will arise if the energy is still delivered to the bulk surrounding material. For example, in the case of thermal heating, a typical lead-free soldering process reaches 200 to 300 °C to obtain conductive joints [130, 247], which severely restricts soldering for heat-sensitive components in electronic devices, such as flexible electronic paper, organic light-emitting devices [11, 134, 248] and some ferroelectric devices containing inorganic ferroelectric materials with low transition temperature or organic ferroelectric materials [136, 138, 249]. Regarding laser sources, a beam diameter below 1 μm is difficult to achieve, and energy density exponentially increases with decreasing beam size. Therefore, targeted energy delivery routes should be developed to better control energies in a localized region without affecting surroundings for micro/nano-electronic fabrication or flexible electronic device assembly.

Only a few new methods for delivering energy at the nanoscale for welding applications have been reported, such as nanoscale soldering of individual gold nanowires by electrical welding using metal solder [250], and light-induced plasmonic local heating to archive nanojunctions of silver nanowires [9]. The former directly adopted Joule heating in a nanosized region while the latter

[†] Portions of this study also appear in: Peng, P., et al., Room-temperature pressureless bonding with silver nanowire paste: towards organic electronic and heat-sensitive functional devices packaging. *Journal of Materials Chemistry*, 2012. 22(26): p. 12997-13001.

concentrated photon energy onto a nanosized "hot-spot" region with the help of plasmonic effects to generate heat locally. Similarly in these two methods, only a small amount of energy was delivered and focused onto nanoscale areas to induce local melting and then facilitate nanojoining. It is worth noting that one of the benefits at the nanoscale occurs in diffusion bonding of metallic nanomaterials, allowing joining at relatively low temperatures or even room-temperature due to the increased surface energy, sintering pressure and diffusion rates [13] when particle size is reduced < 100 nm. Thus, the energy requirement for solid state joining at the nanoscale is very limited. Even room-temperature joining without external energy input has been demonstrated by contacting two gold or silver nanowires [11, 251], where surface-atom diffusion and self-oriented attachment promotes nanojoining as suggested in Chapter 3.

To date, low temperature interconnection processes using metallic nanoparticle paste was demonstrated with silver [173, 182, 252], copper [18] and gold [19], and appears to be a promising alternative for lead-free electronic packaging and flexible electronic interconnections [16, 172, 253, 254]. However, there is no report of the use of nanowires as a filler material to form a bonded joint.

4.2 Experimental

4.2.1 Synthesis of Ag NW pastes

Ag NWs were prepared in a polyol solution with polyvinylpyrrolidone (PVP) as a structure directing reagent using a method modified from the literature [66, 67]. In this study, 330 mg polyvinylpyrrolidone or PVP ($(C_6H_9NO)_n$, K25, M.W.= 24000, Alfa Aesar) and 12.5 mg silver chloride (AgCl, Alfa Aesar) were mixed with 40 ml ethylene glycol (EG, Fisher Chemical) in a round-bottom flask. The mixture was heated to between 160 and170 ^{o}C. Then, 110 mg silver nitrate was dissolved in 10 ml ethylene glycol liquid and added into the mixed solution while stirring vigorously and continuing the reaction conditions for 4 hours. The Ag NWs were condensed by centrifugation at 4000 rpm using a 50 ml centrifuge pipe. The clean supernatants were removed from the centrifuge pipes using a pipette resulting in highly concentrated Ag NW pastes.

4.2.2 Thermogravimetric Analysis

Ag NWs were washed by deionized (DI) water to remove the ethylene glycol and PVP and condensed by centrifugation. Silver nanowire pastes with different washing processes were dried at room temperature. To study the organic contents in the pastes, thermal gravimetric analysis (TGA)

was performed by heating these silver nanowire pastes from room temperature to 500 ^{o}C in air with a heating rate of 5 ^{o}C/min.

4.2.3 Joining using Ag NW Pastes

Prior to joining, the copper wires with 0.25 mm thickness were cut into 60 mm pieces and ultrasonically cleaned in acetone for 3 minutes to remove the organics, diluted HNO_3 for 1 minute to remove the oxide layer and rinsed in ultrapure water (electrical resistivity approximately 18 MΩ·cm). A fine needle attached on a 10 ml syringe was used to locate the Ag nanopaste between two clean copper wires. After depositing 0.05 ml high concentrating Ag nanopaste, the assembly of copper wires and paste was put at room-temperature (18 ^{o}C) or heated at 60~200 ^{o}C in air for 1 hour without bonding pressure. Figure 4.1 illustrates the schematic diagram of the wire configuration during joining process and joint size measurement.

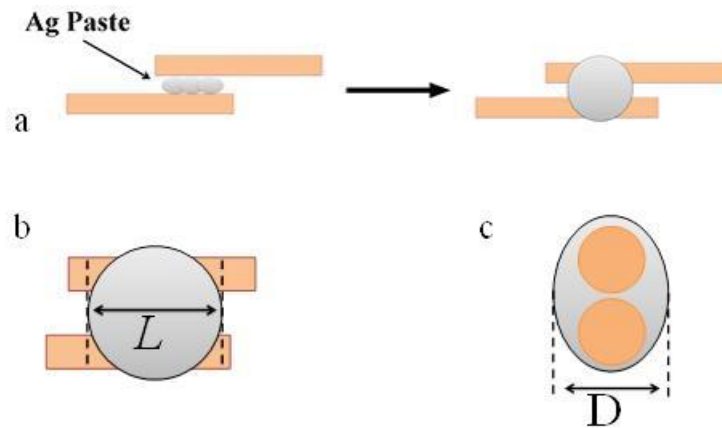

Figure 4.1 Schematic illustration of (a) wire configuration during joining, (b) side-view and (c) cros-section of Ag NW joint after heating. *L* and *D* denote the joining length and thickness of joint.

4.2.4 Tensile Testing

Tensile shear testing was conducted by loading the wires in the axial direction at a rate of 0.5 mm/min using a micro tensile tester (Instron 5548). Figure 4.2 shows the tensile shear test configuration and joint failure. After clamping each bonded sample into the grips, loading was applied. The measured strength of joints is the tensile shear strength due to the applied shear stress during the tensile testing, because two Cu wires were not coaxial. It was estimated by dividing the highest failure force value by the joining area, $\sigma = F_{max}/A$ (N/mm^2 or MPa). The fracture area of

samples was difficult to measure due to the unsymmetrical geometry of fracture region. Here, the average joining area was estimated to normalize the actual fracture area, which joining area A was calculated by multiplying the maximum joining length L by thickness D of the Ag NW filler material.

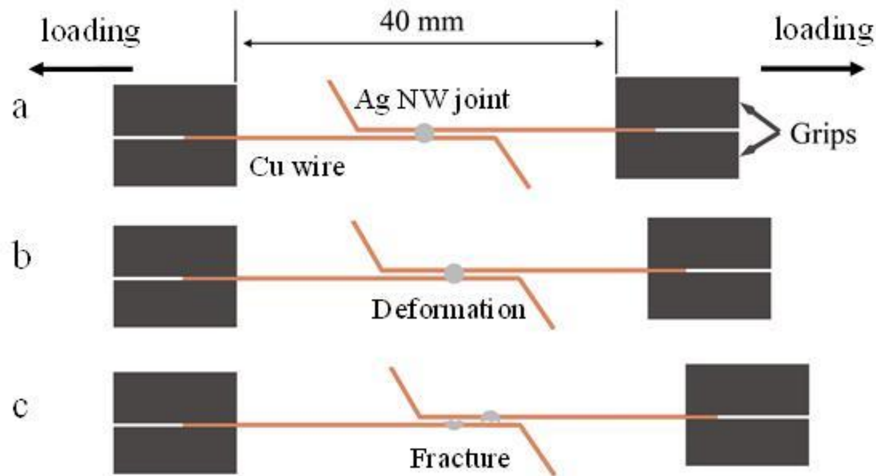

Figure 4.2 Schematic illustration of tensile shear strength testing of bonded samples.

4.2.5 Nanoindentation

The mechanical properties of silver npm were tested with a depth-sensing nanoindenter (Hysitron Triboindenter) equipped with a Berkovich tip. The tip was calibrated on fused silica. Indentations were performed on the mechanically polished flat surfaces in a load controlled mode. All nanoindentation experiments were performed using a constant loading rate of 60 μN/s, with loads of 600 μN. A minimum of 5 indents for each load were collected for each sample.

4.2.6 Resistivity Measurement

Resistivity of joint, ρ, was calculated using $\rho=A\times R/l$, where resistance (R) was measured by four probes low resistance Ohmmeter (DUCTER DLRO 10X), where A and l are the cross-section area and length of the joint.

4.2.7 Microstructural Characterization

Field-emission scanning electron microscope (FE-SEM, Zeiss LEO 1530 Gemini, Germany) were used to study the microstructure of interfaces and fracture surfaces of bonded samples. Energy-dispersive X-ray spectroscopy (EDX, EDAX Pegasus 1200) was employed for elemental analysis. An oscillating knife (DIATOM, Ultrasonic) in ultramicrotome was used to section the interfaces of room-

temperature bonded samples produced with Ag NW paste which was washed three times. The thin slice with 100 nm in thickness was observed using transmission electron microscopy (TEM, PHILIPS CM12) and high resolution transmission electron microscopy (HRTEM, JEOL 2010F).

4.2.8 Local Heat Measurement

The local heat measurement of Ag NW paste and copper substrate were conducted using two methods. The Ag NW paste and Cu powder was mixed and immediately transferred into a crucible to measure the temperature change from room-temperature to 60 ^{o}C using differential scanning calorimeter (DSC, Netzsch, 404C) at 0.5 kpm air condition with heating rate of 0.5 ^{o}C/min. Home-built data acquisition system was employed to measure the temperature change of Ag NW paste on Cu substrate as shown in Figure 4.3.

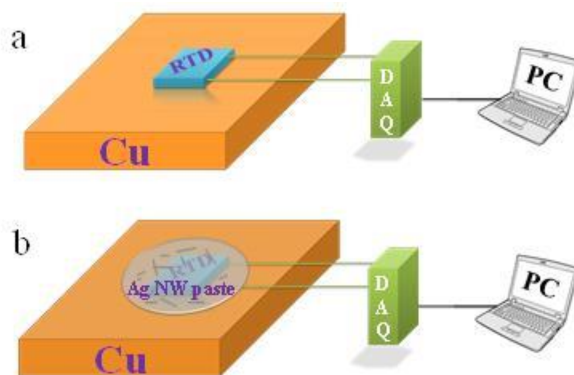

Figure 4.3 Schemes of temperature testing configurations of (a) bare Cu substrate and (b) Cu-Ag NW paste system at room temperature.

4.3 Results

4.3.1 Organic Content in the Pastes

Figure 4.4a shows the microstructure of Ag NWs where the highly concentrated paste exhibits a greenish-gray colour. The Ag NWs with a pentagonal shape are 8-20 μm in length and 50-200 nm in thickness, see Figure 4.4b. The TEM image in Figure 4.4c illustrates the coated organic shell (PVP) with a thickness of 3 nm on the as-synthesized Ag NW due to the stronger interaction between PVP and {100} facets than that between PVP and {111} facets [66, 67]. This residual PVP and EG from the synthesis process could be present at the interfaces of naowires and influence the sintering of the paste. It has been shown that the surface of Ag NPs may be free of organic coatings

after treating with organic solvent, and this yields a reactive interface which readily allows Ag atom interdiffusion during sintering [186]. Although these organics were dissolved in the water of paste and small portions of PVP were strongly absorbed on side surfaces of Ag NWs and does not readily decompose at below 300 ^{o}C [216, 217], the majority of these organic compounds can be removed during the process of washing with DI water as suggested in Cu NP paste [18]. As such, it would be expected that Ag NW interfaces less of organic layers would be reactive and easily allow Ag atom interdiffusion during sintering. Also being demonstrated in Chapter 3, if the bare surfaces of the Ag NW are free of PVP and come into contact there is a free path for surface diffusion and joint formation occurs because of a low activation energy and large driving force due to nano size effect.

Figure 4.5 shows the TGA testing curves conducted at room-temperature up to 500 ^{o}C. As washing times increase, the weight loss dramatically decreased from 20% for one washing cycle to only 0.4% for three cycles. A small fluctuation is evident on the derived weight change curves at 300 ^{o}C, which suggests the organics were readily removed almost. The as-synthesized paste could be stored for half a year and no precipitate was observed. However, when washed 3 times the pastes began precipitate after sitting for three weeks. If the Ag NW paste is washed twice, it is quite stable and only partial precipitation of nanowires was observed. It is worth mentioning that the paste which was washed for three cycles was prone to agglomeration and setting after three weeks but still work for joining after sonication. If continually stored for half year, the paste will completely precipitate and cannot be used for joining. Therefore, it is speculated that the three-time washed paste has a pot life of around six months. However, those pastes washed with one or two cycles could be stored for more than half year in practical applications.

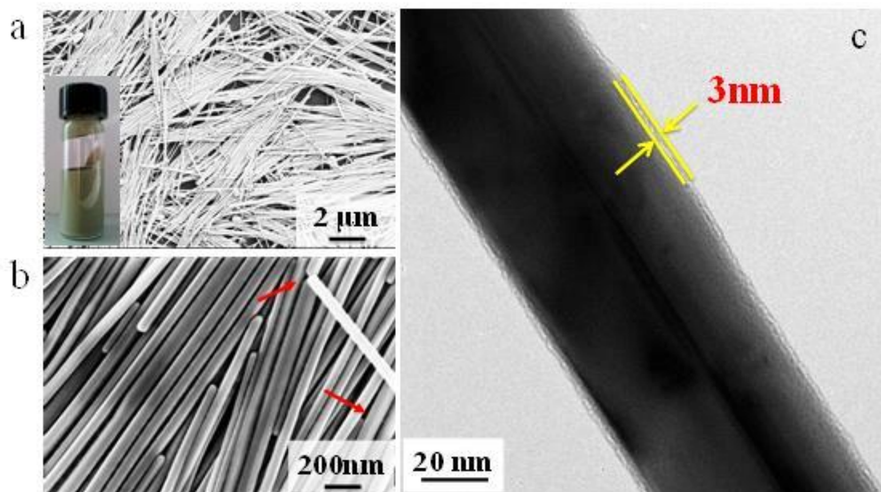

Figure 4.4 (a) SEM image of as-centrifuged Ag NW paste (inset photo is the greenish-grey paste). (b) SEM image of pentagon- shaped (as arrows indicated) Ag NW with 60 nm mean thickness. (c) TEM image displayed the organic coating on the side of Ag NW.

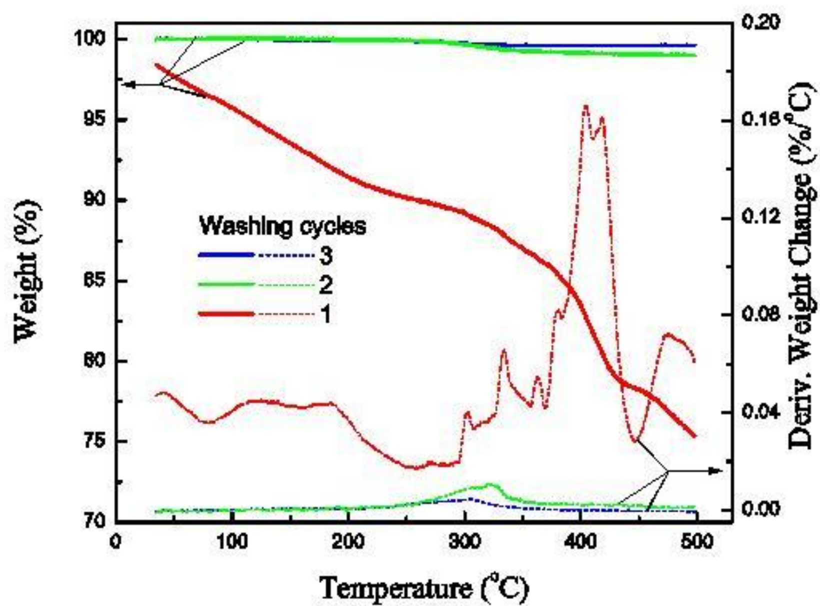

Figure 4.5 TGA curves of three pastes with different washing times using DI water. Solid lines are weight (%) and dashed for derivate weight change (%/°C).

4.3.2 Sintering Behaviors and Weldability of Pastes

To investigate the sintering behavior, the NW paste after washing three cycles was heated on silicon wafers and Cu foils in air, so that the two different substrates could be compared from the standpoint of their different chemical inertness and activity with the water-based Ag NW paste. On the Si wafer, no significant joining of Ag NWs was observed at temperatures below than 200 ^{o}C. Ag NWs show no changes after heating at 100 ^{o}C for 1 hour, while they started to connect to their nearest neighbors after sintering for 5 mins at 200 ^{o}C (as indicated by arrows in Figure 4.6a). After heating at 200 ^{o}C for 1 hour, some NWs became thinner and even broken due to long term solid state diffusion and growth. However, the Ag NW paste on a Cu substrate was found to join at room temperature with some wires interconnected to each other and formed cross-wire or tri-junction structures as shown in Figure 4.6b. The paste sample on Cu sintered at 200 ^{o}C for 1 hour (Figure 4.6c) shows no significant difference compared to that on Si. If the temperature increases to 300 ^{o}C, most of the Ag NWs were broken into pieces and bundled with others to form particles as illustrated in Figure 4.6d. It is worth noting that the Ag NW paste after two washing cycles was stable and no significant bridge paths of nanowires were observed after 1 hour heating at 100 ^{o}C on Si substrate. The adjacent Ag NWs could begin to bridge when the temperature increased to 200 ^{o}C on Si substrate or 60 ^{o}C on Cu substrate.

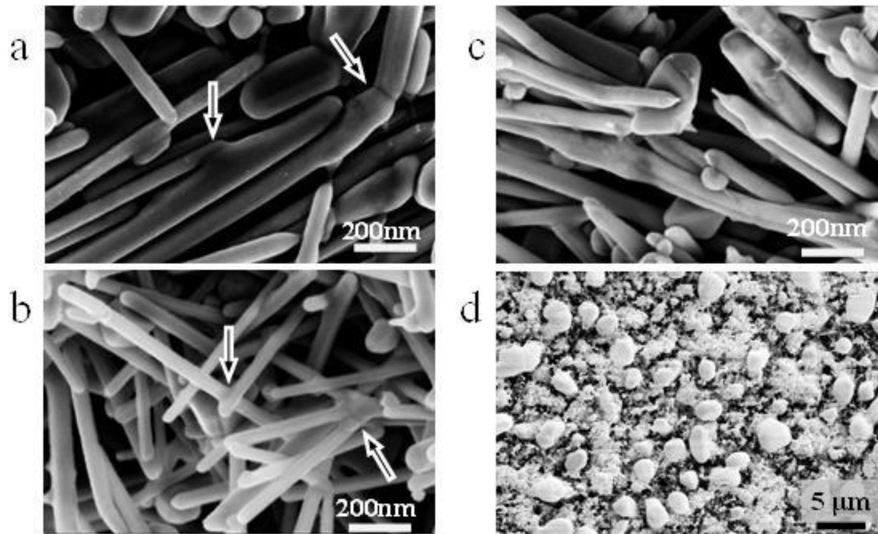

Figure 4.6 Microstructures of sintered Ag NW paste at (a) 200 ^{o}C for 5min on Si substrates; (b) Room-temperature, (c) 200 ^{o}C for 1hr and (d) 300 ^{o}C for 1 hr bonded Ag NW on Cu substrates.

The Cu substrate exhibited a higher activity than Si to promote joining of Ag NWs and lowers the joining temperature down to room-temperature, suggesting Ag NW pastes after three

washing cycles have a potential to bond with Cu based substrates at low temperatures. Therefore, it was used as filler materials to join various substrates without external heating and pressure. Figure 4.7a-e demonstrates the joints between a Cu wire and another Cu wire, a silver-plated copper pad, a gold-plated polyimide pad, and a tin-doped indium oxide (ITO) coated polyethylene terephthalate (PET) substrate. The samples with flexible substrates also displayed low resistance even after folding. The mechanical and electrical properties of Ag NW joints in the following section were measured based on the Cu wire-wire configuration (Figure 4.7a).

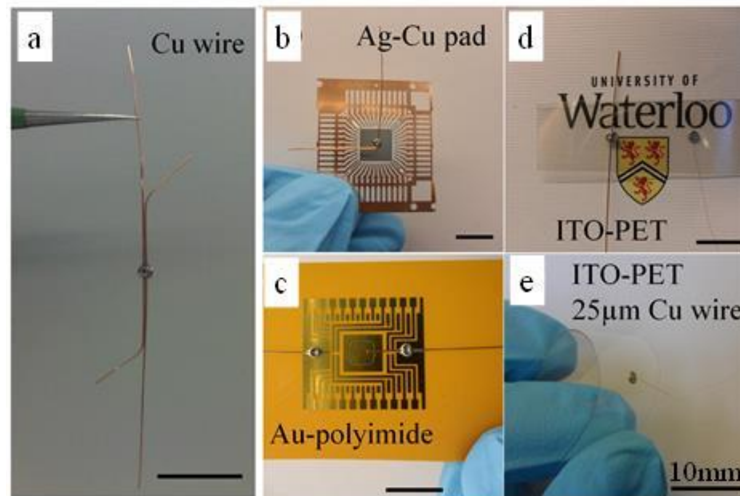

Figure 4.7 Photos of 250 μm copper wires bonded with (a) copper wire, (b) silver coated copper pad, (c) gold coated polyimide and (e) ITO plated PET. (f) 25 μm copper wire bonded on flexible ITO-PET. (scale bars are 10 mm).

4.3.3 Mechanical Properties of Ag NW Joints

A plot of the joint strength of bonded Cu wires as a function of joining temperature using washed pastes following pressureless joining is shown in Figure 4.8. The sample bonded at 60 ^{o}C using paste following one washing cycle resulted in poor strength. With increased washing times the strength increased significantly due to the reduction of organics from the interface of the Ag NWs, since the organics hamper the sintering process by limiting Ag atom interdiffusion. Two Cu wires were bonded at room-temperature to achieve a joint strength of 5.7 $\pm$ 0.5 MPa when three paste washing cycles were employed. Compared to other published works, Cu NP [18] and Ag NP [172] begin to bond only when the temperatures reach 150 ^{o}C, resulting in strengths of 1 to 2 MPa at when a 5 MPa joining pressure is applied because the nanoparticles need to be sintered first and then form

discontinuous networks for joining which temperature is usually larger than 150 °C [186, 255, 256]. Herein, it is believed that the washed nanowires have interconnected and formed discontinuous networks during joining at room-temperature or with the application of moderate (< 150 °C) temperatures. Due to the more intense sintering of Ag NWs which occurs at higher temperatures, the strength increased to 9.1 $\pm$ 0.4 MPa when the temperature increased to 150 °C, which is a higher strength than joints bonded with Cu NP and Ag NP using 5 MPa of pressure [18, 172]. The strength decreased as joining temperature further increased, due to the aforementioned break-up of Ag NWs at high temperature (see Figure 4.6c).

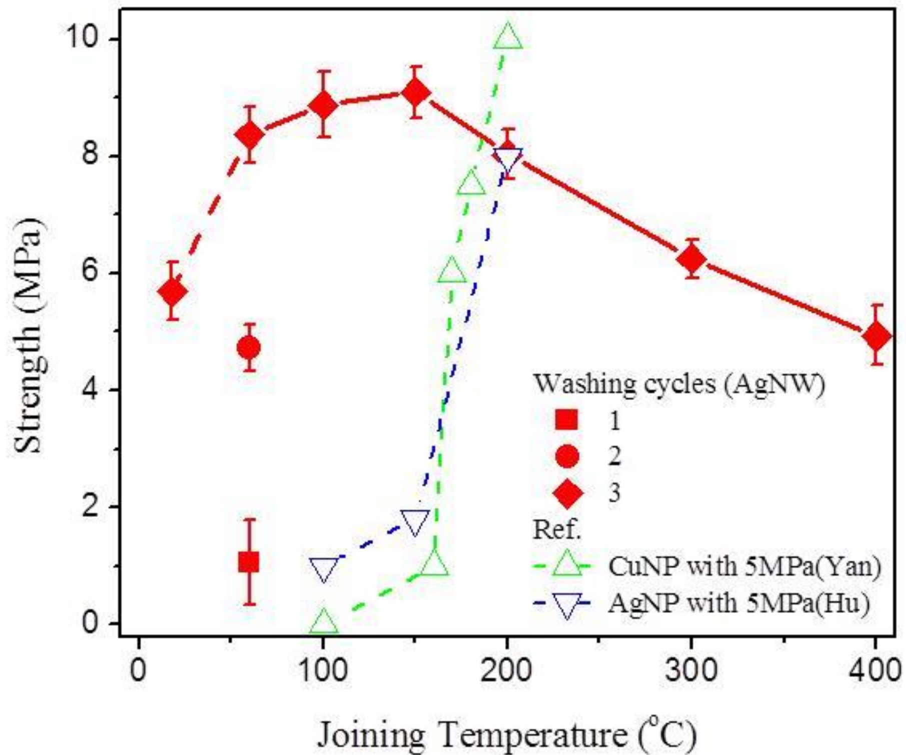

Figure 4.8 Tensile shear strength of bonded Cu-Cu wires with Ag NW paste as a function of joining temperature, the pastes washed once and twice for joining were compared (data of Cu NP are from [18] and data of Ag NP are from [172]).

The load-displacement curves of bonded samples using Ag NW and Ag NP (joining method was the same as Ag NW paste) were compared as shown in Figure 4.9. Typically, the load-displacement curves of the joints produced using Ag NP paste failed with a drop in force by about

65% of the peak force while the Ag NW joints only exhibited a 45% load drop even though similar maximum failure forces are produced, see Figure 4.9. It is speculated that the lower drop in force during failure in Ag NW samples is due to the interlocking of nanowires inside the porous joint. The quality of the joints can also be evaluated by comparing the bonding energy per unit area or fracture energy [257], *i.e.*, the integrated area under the force-displacement curve shown in divided by bonding area (the unit is thus in J/m^2 or N/m). It was found that the fracture energy of the Ag NW bonded at 60 ^{o}C was larger than that of the Ag NP joint, although they had similar maximum failure load and bonding area. A larger integrated area requires more energy dissipation during fracture and thus yields higher quality of joints which are more damage tolerant [258, 259]. The Ag NW joint also has a larger strain before failure than Ag NP joint, indicating that Ag NW could absorb more strain energy and undergo larger deformation in practical applications.

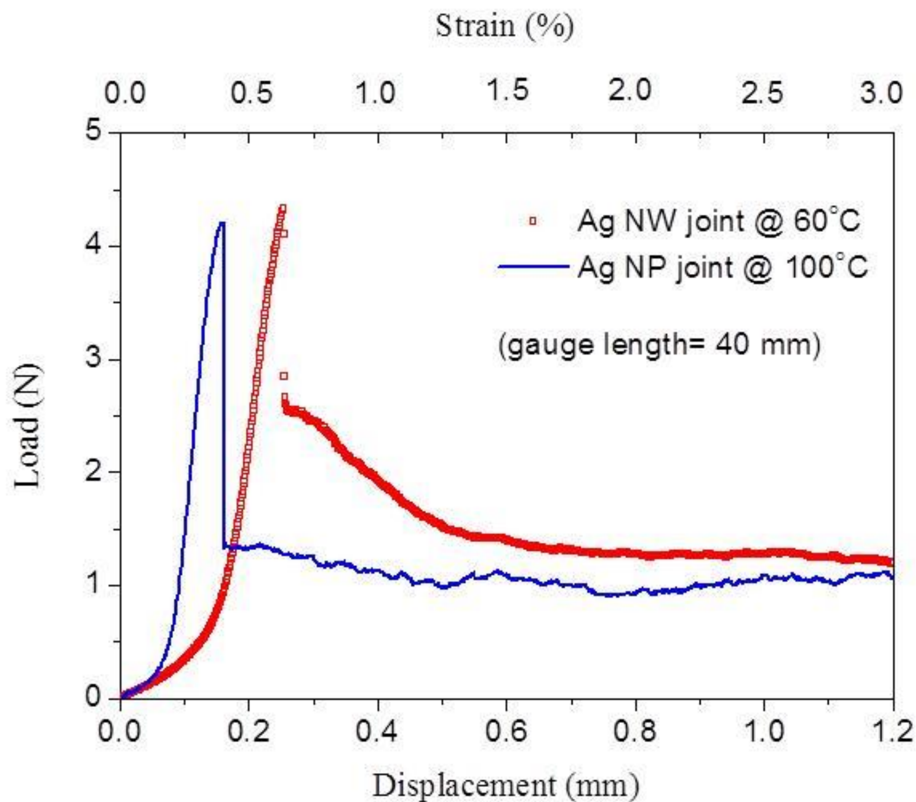

Figure 4.9 Tensile testing load-displacement curves of bonded copper wires with Ag NP and Ag NW pastes.

4.3.4 Mechanical Properties of Ag NW Porous Materials

To examine the mechanical properties of Ag NW porous materials, the elastic modulus and nanohardness were measured with nanoindentation on mechanically polished Ag NW joints. The load-depth curves are shown in Figure 4.10. Ag NW porous material exhibited maximum depth at 600 μN load compared with Ag NP porous material. It could be explained that Ag NPs had higher packing density than NWs due to the nature of their shape difference. Since the slop of unloading curve of Ag NW porous material was smaller than that of Ag NP porous material and Ag bulk, Ag NW porous material is expected to have very low elastic modulus.

Measured elastic modulus was obtained from the recorded reduced modulus, E_r, in nanoindentation according to the Oliver and Pharr method [110, 260, 261] using Eq. 4.1,

$$\frac{1}{E_r} = \frac{1-\nu^2}{E} + \frac{1-\nu_i^2}{E_i} \qquad 4.1$$

where, ν is the Poisson's ratio of silver (ν = 0.37) [104, 262, 263]; ν_i refers to the Poisson's ratio of indenter, here is diamond (ν_i =0.07); E_i is modulus of indenter (E_i = 1141 GPa) [110, 111, 261]. The relative density was calculated using measured modulus according to the relation of $\rho/\rho_{bulk} = (E/E_{bulk})^{1/2}$ [118]. The results of relative density, elastic modulus and nanohardness are listed in Table 4.1. It is found that the elastic modulus of Ag NW porous materials was 14 GPa which was only half of that of Ag NP. It is because of its higher porosity compared with Ag NP when both of them were fabricated at same temperature without joining pressure. This low elastic modulus of Ag NW porous materials is very close to the modulus of 8 GPa for polyimide based substrates[264] and 11 GPa for PET/glass fiber substrates [265]. Meanwhile, the nanohardness of Ag NW porous materials was 0.51 GPa approaching to that of polyimide (0.45 GPa [266]) and PET (0.33 GPa [267]). These close mechanical properties between the Ag NW porous material and widely used flexible substrates make them mechanically compatible during deformation. This matching will help to relieve the thermomechanical stress by taking advantage of the porous structure [17] in practical applications.

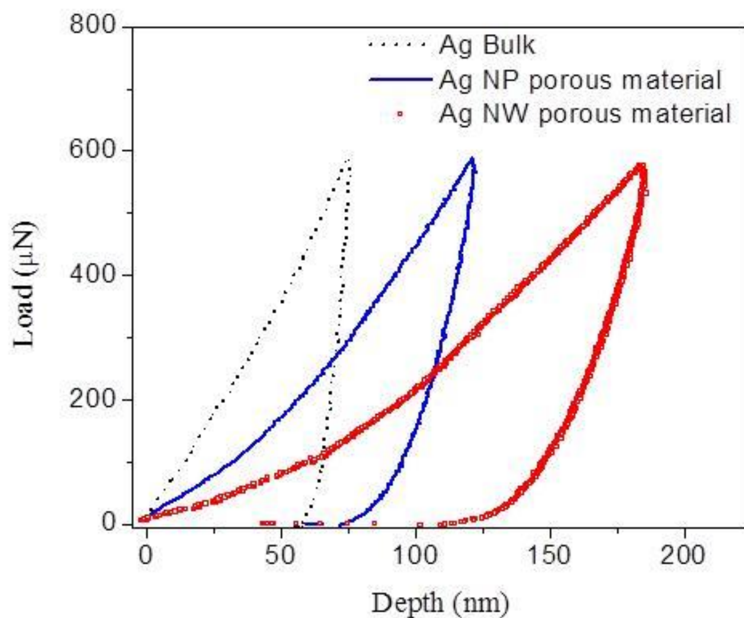

Figure 4.10 Typical load-depth curves Ag NP and NW porous materials (bulk Ag for comparison).

Table 4.1 Relative density, elastic modulus and hardness of Ag NP and NW porous materials (joining at 60°C).

Materials	Relative Density (%)	Elastic Modulus (GPa)	Nanohardness (GPa)
Ag NW	38 ± 7	14.33 ±0.48	0.51 ±0.04
Ag NP	54 ±11	27.74 ±1.23	1.01 ±0.05
Bulk Ag	1	95.08 ±4.43	1.81 ± 0.15

4.3.5 Electrical Property of Ag NW Joints

The effects of PVP have been minimized in the present study through the application of repeated water washing in order to achieve joining at room-temperature. In addition, this promoted high conductivity as a secondary benefit from PVP removal. As shown in Figure 4.11, the room-temperature bonded Cu wire joints exhibited ultralow relative resistivity (101.27 ± 0.05 nΩ·m) because of the metallic bonding of Cu-Ag and Ag NW-NW. This value is two orders of magnitude lower than the value reported for a Cu NPs joint (8×10^4 nΩ·m), and similar to that obtained after

prolonged times in cured and reflowed Ag nanocomposites (60 nΩ·m) [18, 268]. The resistivity measured here was the relative resistivity of Cu-Ag joint with the configuration shown in the inset image of Figure 4.11.

For comparison, the resistivity of the Cu wire was plotted which presents a linear relationship with temperature because of temperature coefficient of resistance [269]. This coefficient accounts for the slightly increasing of resistivity of bonded joint from 18 °C to 150 °C. The further sintering of the Ag NWs at elevated temperatures results in the enhancement of conductivity. At 250 °C, the joint obtained the lowest resistivity 37.83 ± 0.04 nΩ·m which is comparable with 35.58 ± 0.12 nΩ·m observed for a pure Cu wire. However, because of broken nanowires and oxidation of Cu after 250 °C, grown temperature introduced the increasing of resistivity.

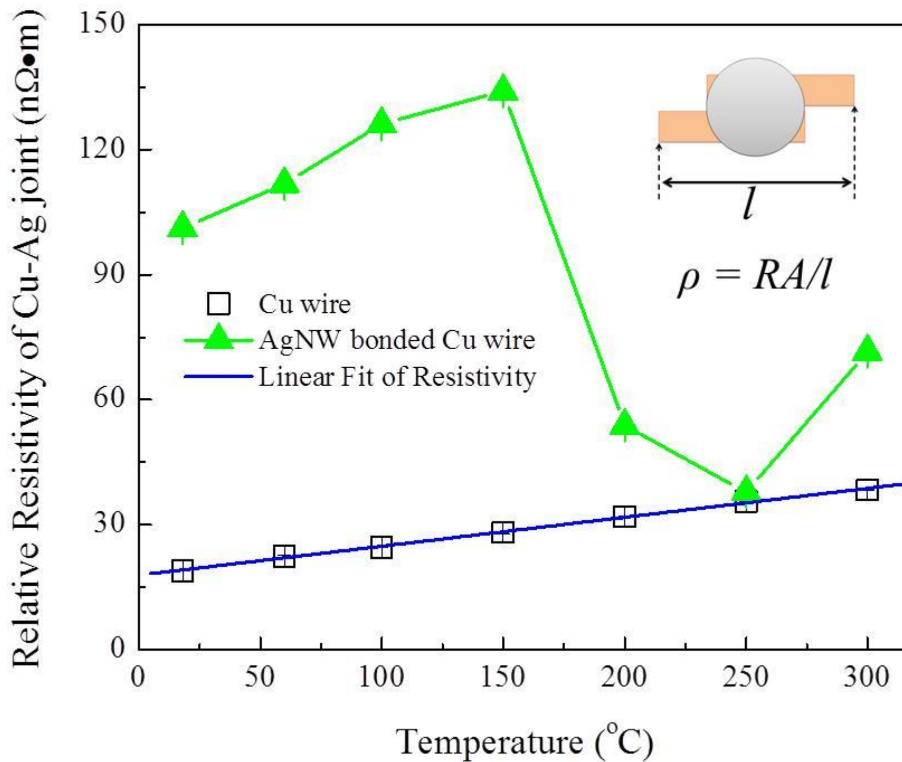

Figure 4.11 Relative resistivity of bonded Cu wire joint with Ag NW paste washed three times as a function of sintering and testing temperatures. Bulk resistivity of pure Cu wire was compared. Inset: the configuration of measured joint, relative resistivity was calculated using $\rho=RA/l$ with the measured resistance (R), cross-section area of joint (A), and length for measuring voltage drop (l).

4.3.6 Microstructure Characterization

Two Cu wires can be identified with a 20 μm gap and the interface between Cu and Ag matrix is very sharp in Figure 4.12a. The structure of filler material was less of micropores (Figure 4.12b) as in the case of Ag metallo-organic NPs joint [173], however, the joint was nanoporous because no pressure was applied during the joining process. In the interface as shown in Figure 4.12c, the metallurgical bond between the Cu wire and the Ag paste was found to be continuous. The EDX line scan shows the Ag and Cu elements could form a ~0.5 μm transition layer by diffusion.

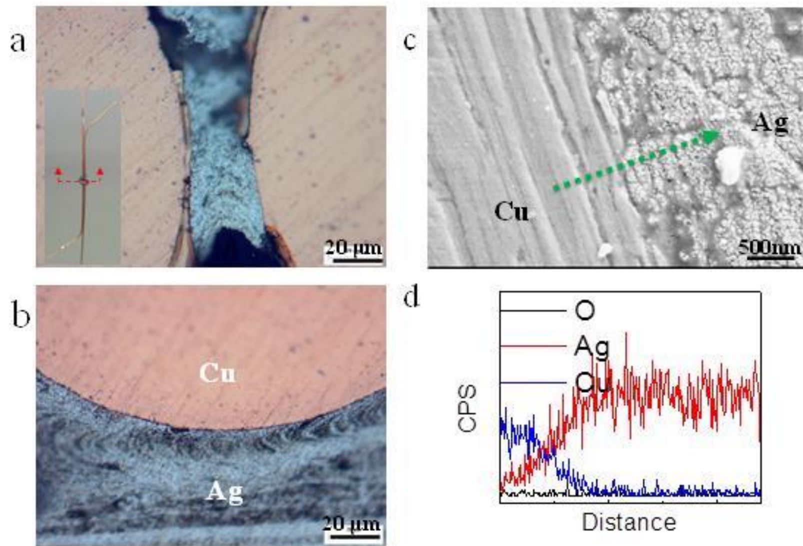

Figure 4.12 Microstructures of cross sections of Ag NW paste bonded Cu-Cu joints at room temperature: (a) Two Cu wires can be identified with a 20 μm gap filling with Ag NW paste with the bonded wires shown in the inset; (b) Optical microscope image of clear interface of Cu and Ag matrix; (c) SEM image of bonded interface of cross section shows the bond is continuous and formed metallurgical bond between the Ag nanomaterials and Cu wire; Dashed arrow indicating (d) the EDX line scanning direction, Ag and Cu elements formed a 0.5 μm transition layer by atoms diffusion.

The fracture surfaces of bonded samples before and after testing have been observed to investigate the joining behavior of Ag NW pastes. At room-temperature, no testing sample depicts the straight Ag NWs well interconnected and formed three-dimensional Ag discontinuous networks in Figure 4.13a aforementioned. In TEM images Figure 4.13b, the Ag NWs are joined together in either an end-to-end, end-to-side, or side-to-side manner. After testing, some interconnected Ag NWs were broken as highlighted with circles in Figure 4.13c. The Ag NWs were distorted because of the strain under loading which indicates the Ag NW discontinuous networks are good for absorbing mechanical

stress. This high strength of nanowires due to the nano-scale effects [102] and the good mechanical property of discontinuous networks accounts for the fracture strength of joints. However, at high joining temperature, Ag NWs transformed into particles and the failure points of filler materials were difficult to identify (see Figure 4.13d).

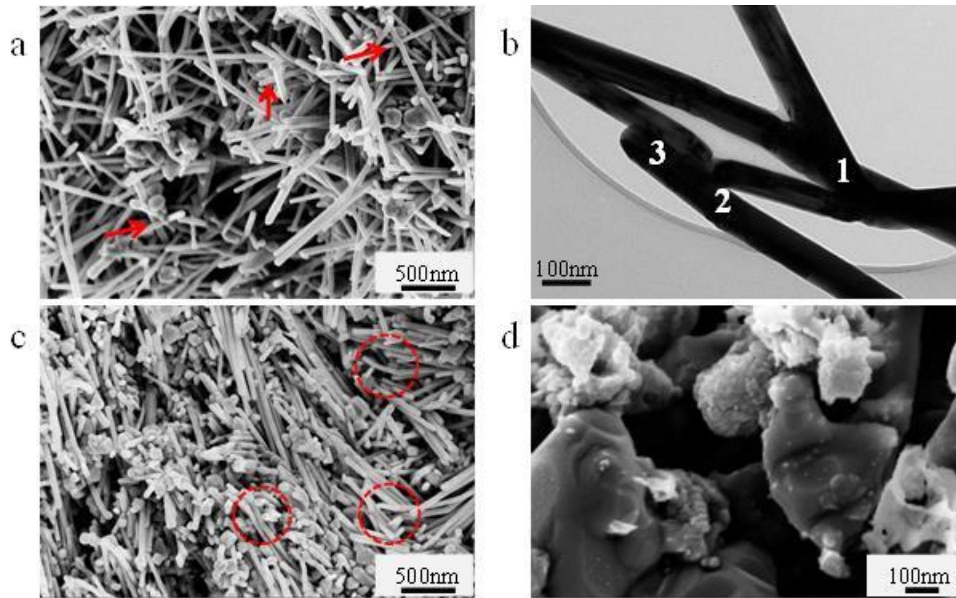

Figure 4.13 SEM (a) and TEM (b) images of three-dimensional Ag discontinuous networks formed at room-temperature. Arrows indicating the Ag-Ag junctions, numbers 1, 2 and 3 showing end-to-end, end-to side and side-to-side three different joining modes of Ag NWs. Fracture surface of joints formed at (c) room-temperature and (d) 300 ^{o}C. Circles indicated the failure of Ag NWs.

It is interesting to note that the Cu wire fracture surface of joint bonded at room-temperature was covered by a residual thin layer of Ag NW after testing as shown in Figure 4.14a. This indicates that the fracture of the joint is not in the interface of Cu-Ag, but rather the Ag NW discontinuous networks close to the Cu interface. The high-magnification SEM images of Ag network matrix is depicted in Figure 4.14b showing 100% pure Ag in EDX results. Some particles mixed with and grew on Ag NWs which are in the folded thin layer in Figure 4.14c and on the Cu surface in Figure 4.14d. This thin layer contains 18 at.% O and 20 at.% Cu (see Figure 4.14c) while the Cu surface is 23 at.% O in Figure 4.14d. Therefore, the particles were CuO which originated from the oxidation of Cu on the surface. Those CuO nanoparticles might be from the Cu surface because of incomplete cleaning or oxidation of Cu during joining. However, those nanoparticles dramatically decreased on the Cu surface when joining temperatures increased to 100 ^{o}C, see Figure 4.14e. If the joining temperatures

continue to increase to 150 ^{o}C, no CuO particles are observed obviously, but only well interconnected and distorted Ag NWs appear on the Cu surface, see Figure 4.14f. In addition, the presence of CuO might serve as a beneficial co-bonding material in local areas during the room-temperature joining and contribute to the good mechanical properties of joints.

Here, one should consider that the bonds of the PVP could be terminated with hydroxyl groups due to the presence of hydrogen peroxide and water in polymerization during fabrication process [270]. Hence, PVP can be used as not only a stabilizer but also a reducing agent [271] as it has been successfully used to synthesis noble metal nanomaterials [272-274]. It is believed that the residual PVP on the surface of Ag NWs or in the water of paste could prevent the formation of CuO and/or deoxidize CuO to Cu and further clean the Cu-Ag interface and provide better conditions for interdiffusion and joining. This "*in-situ* cleaning" mechanism is proposed as follows: hydroxyl groups terminated PVP reacts with copper oxide and generates copper in an "*in-situ* cleaning" process during joining, or prevent the formation of copper oxide shown in Figure 4.15. This phenomenon will be discussed later in detail.

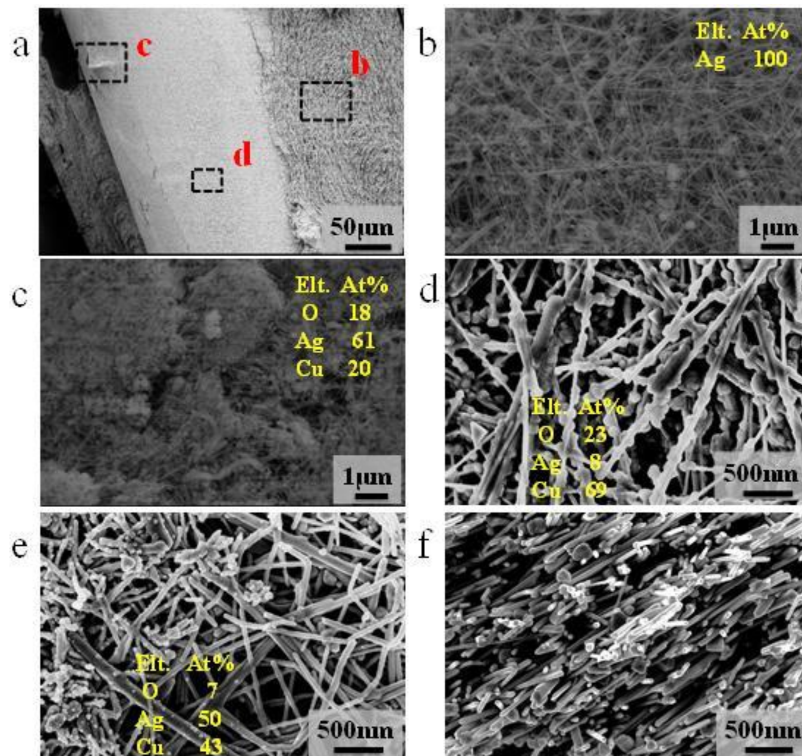

Figure 4.14 SEM images of (a) failure joint bonded at room-temperature, the high-magnification images of squares corresponding to (b) Ag matrix surface, (c) folded Ag NW layer, with particles

attached on AgNW and (d) Cu wire surface with EDX results. The Cu wire surface of failure joint bonded at (e) 100 ^{o}C and (f) 150 ^{o}C.

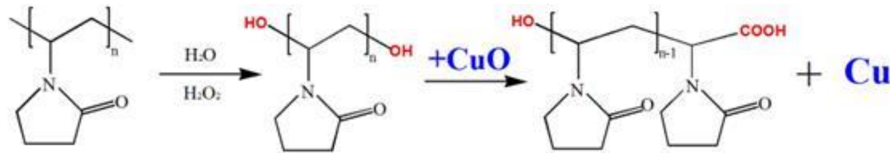

Figure 4.15 “In-situ cleaning” behavior of PVP during joining.

4.4 Discussion

4.4.1 Self-generated Local Heat

It has been shown that the end surface of Ag NWs can be free of PVP but the side surface of them is still covered by PVP after washing in Section 3.4.1. Without the assistant of energy, it will stay at the interface to impede the joining of Ag NWs. To verify if there is any self-generated heat which promoted joining of Ag NWs at room-temperature in the Cu-Ag NW system, the Ag NW paste and Cu powder was mixed and immediately transferred into a crucible to measure the temperature change from room-temperature to 60°C using DSC. The results in Figure 4.16a show two exothermal peaks located at round 32 and 60°C, respectively. The first one might be due to the oxidation of Cu and second one may be associated with the surface area reduction during joining of Cu to Ag, or Ag to Ag. A further assessment of this possible heating was done by monitoring the temperature change using resistance temperature detector (RTD) once the Ag NW paste was dropped onto a Cu substrate as configured in Figure 4.3. The temperature profiles of water-Cu compared to NW paste-Cu systems are shown in Figure 4.16b. After dropping water or water-based paste onto the substrates, the temperatures all decreased because of heat absorption and evaporation of water and finally reached a constant temperature at around 22 ^{o}C. However, the temperature history in the sample containing the Ag NW paste shows a peak feature at the end of decreasing tail, highlighted in the dashed box of Figure 4.16b. This slight increase in temperature is evidence that heat is generated within the Cu and Ag NW paste system, which represents the local heating, measurable in the macro-scale system. The local heating would dissipate through various heat sinks in the Cu - Ag NW paste system, including heat transfer to surroundings through the Cu substrate, paste and the evaporation of water. Although the measurable temperature difference is only a 0.5-1 ^{o}C reading from the curve, the localized thermal

energy per volume is likely to be much higher since it is generated at the nanosized interfaces and transferred to macro components. The experiments demonstrated that this self-generated local heating would be sufficient to promote joining of Ag NWs and Ag NWs to Cu substrates. However, it only behaves as a slight temperature increase, and thus does not affect the heat sensitive substrate during joining process, which makes it a very promising approach for room-temperature joining.

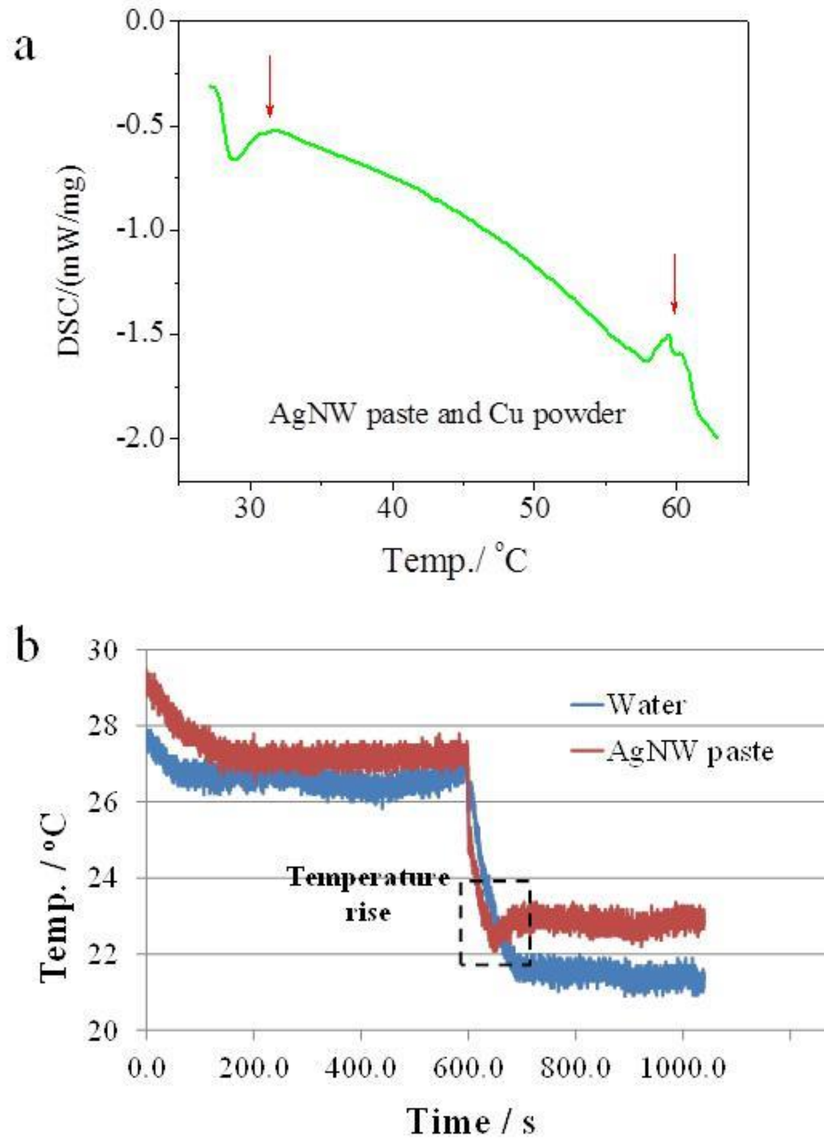

Figure 4.16 (a) DSC curve of Ag NW paste with Cu powder heating in air. (b) Temperature profiles of pure water and Ag NW paste with Cu substrate.

4.4.2 Local Heat: Lumped Capacity Model

To calculate this local heating energy, the lumped capacity model [275] was used at the interfaces based on measured temperatures. In this model, the paste and copper are two parallel contacted plates and the temperature difference inside each plate is negligible, see configurations in Figure 4.17a. Since the heat generations mostly occurred in the NW paste side close to interfaces and the temperature profile of Cu substrate was not measured, the heat energy is only calculated on NW paste side. The evaporation of water and absorption by components of system were not considered. Thus, according to Newton's Law of Cooling, the rate of heat loss of the plates (NW paste) is proportional to the temperature difference between them and their surroundings. Thus, the first-order differential equation is,

$$\frac{dQ}{dt} = hA\left(T(t) - T_{\infty}\right) = hA\Delta T(t) \qquad 4.2$$

where Q is the thermal energy; h is the heat transfer coefficient between the plate and air, typically h for air is approximately 1 - $2\ Wm^{-2}K^{-1}$ for free convection [276]. A is the interfaces of the heat being transferred, T is the temperature, a function of time t in the paste plate; T_{∞} is the temperature of surrounding, here $T_{\infty} = T_{air}$ was taken. The time-dependent thermal gradient $\Delta T(t)$ corresponds to the difference $T(t) - T_{air}$, between the plate and air.

$$Q = \int \frac{dQ}{dt} dt = hA\int \Delta T(t)dt = hA\int \left(T(t) - T_{air}\right)dt \qquad 4.3$$

$$\Delta Q = Q_{paste} - Q_{water} \qquad 4.4$$

$$\Delta Q = hA\int \Delta T_{p-w}(t)dt \qquad 4.5$$

Therefore, the transferred heat energy Q is calculated by integrating dQ/dt as indicated in Eq. 4.3. In this case, the local heat ΔQ is the difference between the Cu - NW paste and Cu - water system (here Cu - water system is a reference for calculating how much heat generated due to the applying of NW paste), which can be calculated as shown in Eq. (4.4, 4.5) by integrating the area of two temperature profiles (Figure 4.16b) and taking the difference of them, $\int \Delta T_{p-w}(t)dt$. In this lumped capacity model, the heat sink on Cu plate side was not calculated. Therefore, this calculation only captured a portion of the generated heat as schematically indicated in Figure 4.17b (shaded area). Here, only a nanosized interface is considered: one single nanowire flat on Cu surface. The width of one side of the Ag NW is 100 nm (which is the side length of a NW with an overall thickness of 162 nm due to the pentagon shape of its cross section); and the length of the Ag NW is 15 μm, while the length of

the Cu surface is 20 μm since the Cu surface was not fully covered as shown in Figure 4.17c. This coverage value corresponds to 46% in this case, which is close to the range of 40-50% based on TEM images. Therefore, $A = 162\ nm \times 20\ \mu m$ is the projection area of the single NW - Cu nano-interface system on paste-air interface (based on the parallel plate assumption). The minimum heat transfer coefficient of still air at room temperature was assumed to be $1\ Wm^{-2}K^{-1}$ to calculate the minimum transferred heat energy. The difference between the two curves is around $433\ K{\cdot}s$ (from the peak temperature after applying paste/water at $730\ s$ to the stable temperatures at $1038\ s$). Then, the local heat ΔQ will be $1.40\ nJ$ (on the NW paste side for a thin slice with cross section area of A).

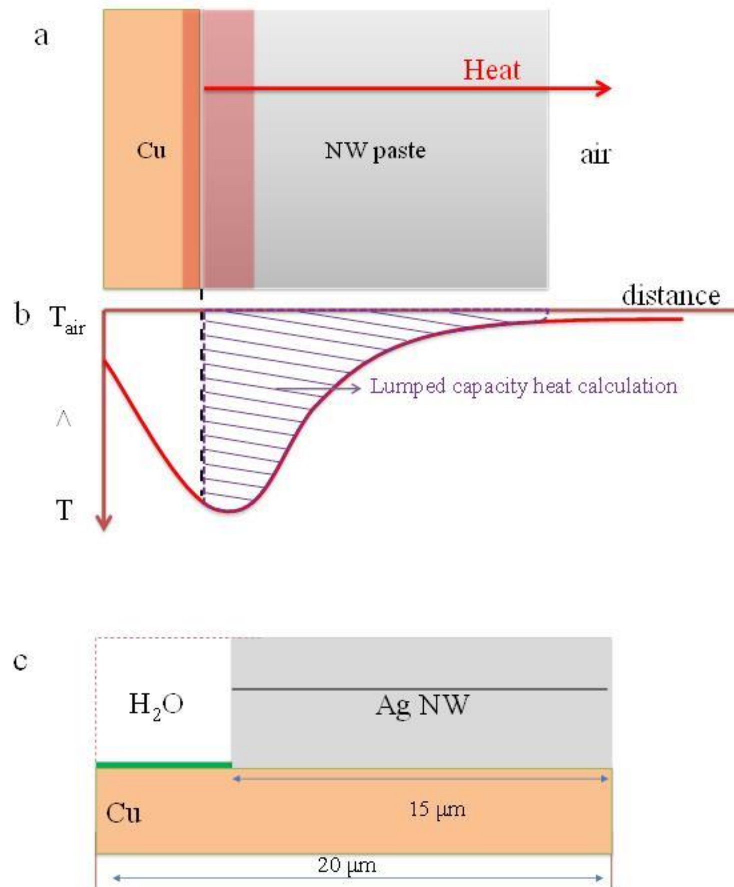

Figure 4.17 (a) Cu and NW paste plate assembly for heat energy calculation using lumped capacity model and (b) its schematic of temperature profile with calculated localized heat energies at the nanoscale. (c) Side view of localized interface with size configurations.

4.4.3 Interfacial Reaction

The cross-section shows that the Cu and Ag NW were in close contact on the round interface, without obvious unbounded interfaces. Due to the nature of liquid in the Ag NW paste, it can flow around the Cu wire and fill the gap between two components to make a complete connection around the circumference. SEM analysis with an EDX line scan across the interface indicates only Cu and Ag with undetectable oxygen (see Figure 4.12d). On the fracture surface, a thin Ag NW layer on Cu wire surface was observed as shown in Figure 4.18a. The Ag NWs were interconnected at room-temperature in the filler Ag NWs (Figure 4.18b) similar to the previous sintering results indicate in Figure 4.6d. Meanwhile, many nanoparticles were clearly observed on the surface of Ag NW within this thin layer (Figure 4.18c) close to the Ag-Cu interface. These nanoparticles show darker contrast than Ag NWs if compared to the in-lens and backscattering images in Figure 4.18d, suggesting that they contain lighter elements compared with Ag, in this case Cu. Figure 4.18e clearly illustrates the nanoparticles grew on the surface of Ag NWs. According to XRD, EDX analysis via HRTEM, these nanoparticles have been identified as CuO [277]. The difference in chemical potentials of Cu and Ag implies that Cu would be oxidized to Cu ions and migrate to defect areas on the surface of the Ag NWs, and combine with oxygen to grow Cu_2O which later transforms to CuO.

According to the observation of the fracture surfaces of samples bonded at room-temperature without further heat treatment and with heating at higher temperatures, the untreated sample contained a high density of CuO nanoparticles on the surface of Ag NWs (shown in Figure 4.14d or Figure 4.18c). However, CuO nanoparticles decreased significantly after heat treatment (see Figure 4.14e-f). After treating at 150°C, the present nanoparticles on the surface of Ag NWs can only be observed under high magnified SEM image as illustrated in Figure 4.19. The morphology of them is different with the observed CuO nanoparticles as noted in Figure 4.19b. It is confirmed that the residual PVP served as reducing agent to react with CuO and obtain Cu nanomaterials as scheme suggested in Figure 4.15. To reproduce this process, the CuO-Ag NW composite was heated in water solutions containing PVP at a higher temperature of 80°C as studied by Xiong *et al.* [278]. At room-temperature, most of these CuO nanoparticles grown on the surface exhibit an amorphous structure under TEM observation, see Figure 4.20a-b. After heating in PVP solution, the CuO nanoparticles became much smaller and more agglomerations were observed in Figure 4.20c. HRTEM image indicates that the amorphous structures decreased and more crystalline nanoparticles were observed after reaction, see Figure 4.20d. Based on lattice diffraction and EDX results, most of the CuO nanoparticles on the surface of the Ag NWs were found to have transformed to Cu nanocrystals. This

suggested that at higher temperatures PVP on Ag NW surfaces could clean the CuO formed during the joining process at room-temperature. It can reduce or prevent the oxidation of Cu and Ag during joining process because of self-generated local heating, demonstrating a "self-cleaning" mechanism among Cu-PVPs-Ag system as previously discussed in Section 4.3.6.

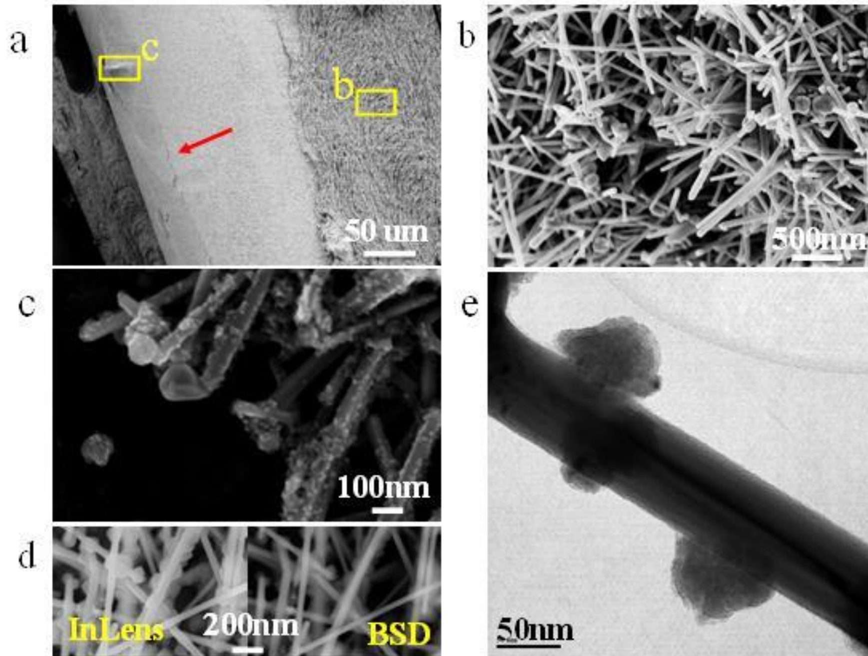

Figure 4.18 SEM images of (a) fractured sample and (b) fractured surface on Ag NW side. (c) Nanoparticle decorated Ag NW layer. (d) Comparison of InLens and Back-scatting images of NP decorated NWs, indicating the NPs have different composites with Ag NWs. (e) TEM micrograph of NP grow on the surface of Ag NW taken from Cu-Ag interface of bonded sample.

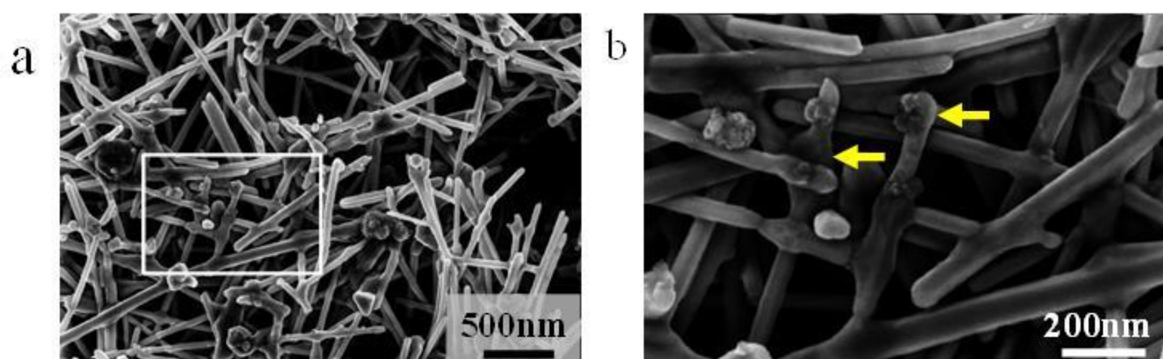

Figure 4.19 SEM micrographs of fractured interfaces of joint formed at room-temperature: (a) heated at 150°C for 1 hr and its high resolution image (b).

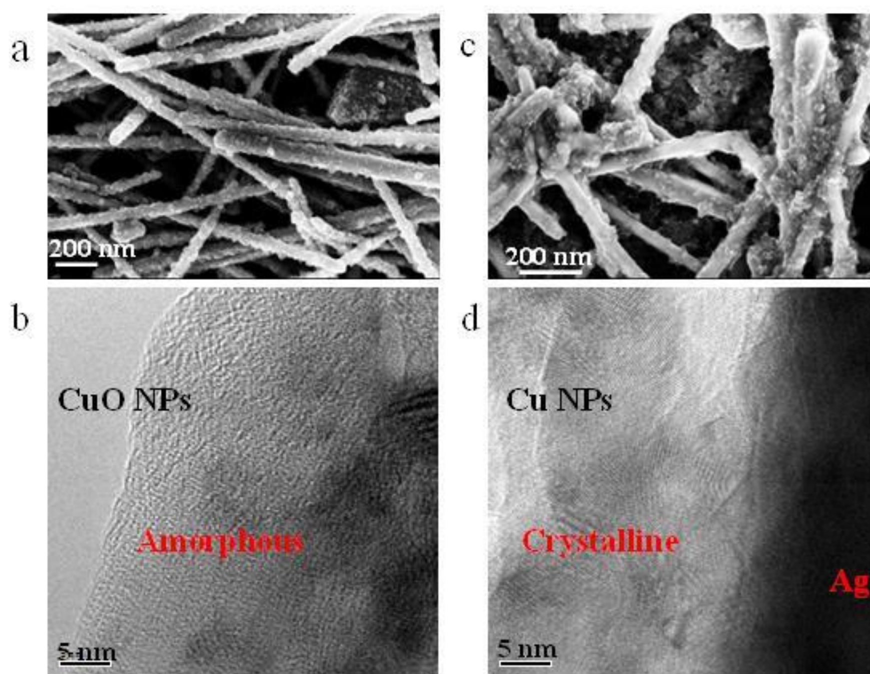

Figure 4.20 SEM and TEM images of (a, b) CuO grown on the surface of Ag NW at room-temperature with large portions of amorphous structures and (c, d) changing to Cu nanocrystalline structures after heating at 80°C for 3 hrs.

4.4.4 Local Temperature

It is worth noting that the local heating may originate from the oxidation of copper and the reaction of PVP on the Cu-Ag interfaces, the reduction of surface during joining of Ag-Ag or Cu-Ag could contribute to the generation of heat as well. To understand mechanism of this self-generated

local heating induced nanojoining at the nanoscale, some simple calculations of the temperature rise can be made base on the enthalpy of reactions. First, the oxidation of Cu will release heat ΔH_1 as shown in Eq. 4.6. Due to the long term oxidation of Cu during the joining time scale of a few seconds to minutes, the heat energy is difficult to calculate because of a heat sink effect. However, this reaction will produce CuO and supply the initial heat for CuO reacting with PVP, which could generate heat ΔH_2 (Eq. 4.7). Meanwhile, the removal of PVP at the interface and the generated heat can promote the interdiffusion of Ag and Cu to form metallic bonds, see Figure 4.21a-b. This reaction is shown in Eq.4.8 and ΔH_3 is the released heat calculated according to reduced surfaces of Cu and Ag because the composition of Ag_xCu and its reaction heat is difficult to be identified. Here, both of the surfaces of Cu and Ag are considered and they are the (100) plane and surface energies of them can be found in literature [279]. The heats from the enthalpy change of the first two reactions Eq. 4.6, 4.7 can be obtained from thermochemical data handbooks [280]. Since the thermodynamic data of PVP is difficult to obtain, one can simplify the long chain R as methyl.

$$2Cu + O_2 \rightarrow 2CuO + \Delta H_1 \qquad 4.6$$

$$2CuO + R - CH_2OH \rightarrow 2Cu + R - COOH + H_2O + \Delta H_2 \qquad 4.7$$

$$xAg + Cu \rightarrow Ag_xCu + \Delta H_3 \qquad 4.8$$

Due to a layer of CuO coated on Cu and Ag surface in the single NW-Cu localized system and the CuO-PVP reaction mainly occurring on the Ag NW surface, the heat ΔH_2 will directly conduct to Ag NW to heat it up. It is difficult for this heat to transfer to the surrounding water / air because of their small thermal conductivities, $K_{H2O} = 0.58\ W\cdot m^{-1}\cdot K^{-1}$, $K_{air} = 0.024\ W\cdot m^{-1}\cdot K^{-1}$ [281]. The presence of CuO at Cu-Ag interface (Figure 4.21a) will block the heat transfer from Ag to Cu substrates since its thermal conductivity, $K_{CuO} = 20\ W\cdot m^{-1}\cdot K^{-1}$ [282], which is 20 times smaller than that of Ag, $K_{Ag} = 427\ W\cdot m^{-1}\cdot K^{-1}$ [281]. If the CuO coated Ag NWs are away from Cu-Ag interface, the surroundings water and air also act as a thermal barrier to keep the heat inside the Ag NWs. Therefore, one can calculate the temperature raise of one single Ag NW as indicated in Eq.4.9:

$$\Delta T_{Ag} = \frac{\Delta H_2}{c_{Ag} m_{Ag}} \qquad 4.9$$

where c is the specific heat capacity of Ag ($c_{Ag} = 0.240\ J\cdot g^{-1}\cdot {}^{o}C^{-1}$) [283] and m_{Ag} stands for mass of Ag NW. As mentioned previously in Section 4.4.1, one side of the Ag NW is 100 nm and length of Ag NW is 15 µm (Figure 4.21), yielding $m_{Ag} = 2.706\times10^{-12}\ g$. Here, It is assumed that the CuO layer with 10 nm thick and 100% coverage on Ag NW was completely reacted, and that, ΔH_2 is $0.314\ nJ$. Since

ΔH_1 and ΔH_3 are excluded here, this local heat value is smaller than the calculated value of total local heat ΔQ using lumped capacity model (Section 4.4.1). However, they are quite close. Considering the single Ag NW, $\Delta T_{Ag} = 484\ ^oC$, finally (that is, temperature of Ag NW will be 504 ^{o}C when room temperature is 20 ^{o}C). This high temperature is striking, however one should note that this calculation is based on the assumptions of perfect surface area coverage of CuO, and that there is sufficient PVP content in the paste to support the reaction. Furthermore, the CuO-PVP reaction in Eq. 4.7 was assumed as a static process and would generate heat instantaneously. However, this reaction in reality is a dynamic process with different rates of reaction depending on the concentration gradient of chemicals, temperature, pressure and the use of catalyst. Since the complexity of reaction conditions in this study, especially in the single Ag NW- Cu system as depicted in Figure 4.21, there is no data of their reaction rate available in present literatures for such nano scale system and it is also too difficult to be measured experimentally. Therefore, this calculated high temperature is a predicted instant maximum value. In fact, the reaction would probably last for few minutes during joining process, meaning that the heat was released gradually and accumulated in a local area because of low thermal conductivities of surroundings. Considering the long-term time scale during the actual joining process, the maximum local temperature of Ag NW would be lower than 504 ^{o}C because of the limiting kinetics of the CuO-PVP reaction and heat sink effects. To generally predict the local temperature of Ag NW in this study, both the heat generation from the reaction and heat transfer into Ag NW are instantaneous as assumed previously. It suggests that the Ag NW is substantially heated above room temperature after the CuO-PVP reaction, see Figure 4.21b. The reaction will consume the residual PVP in the water of paste and on the surface of Ag NWs, leading the less PVP in the interfaces and making the side surface of Ag NWs exposed and activated as well for joining similar as the end surface activation in Chapter 3. Also, this temperature rise will trigger the nanojoining of Ag NWs when they are in contact and induce a significant sintering of nanomaterials system [172, 284] to form networks. It is also sufficient to supply the energy for Cu and Ag atomic diffusion at Ag NW-Cu interface.

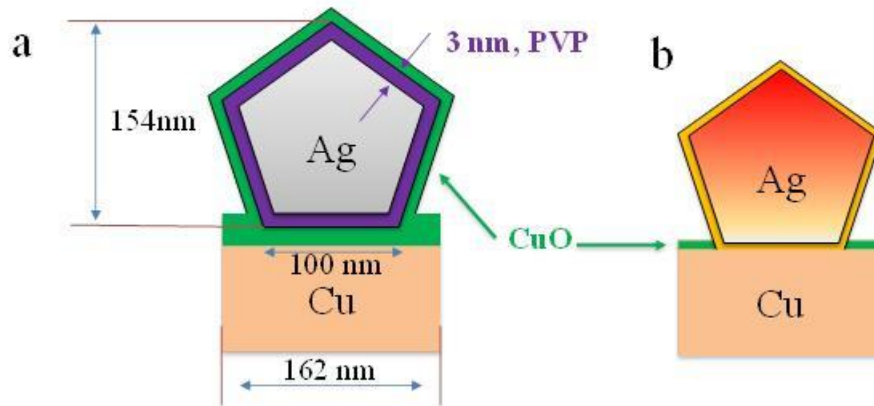

Figure 4.21 Schematic illustration of cross-section view of simplified Cu-Ag localized interface (a) before and (b) after temperature rise due to CuO-PVP reaction.

It is worth noting that this temperature is supposed to be the transient maximum value of Ag NW since the heat which would be conducted out was ignored and the reduction heat from Eq. 4.7 is the maximum due to the 100 % coverage setup of CuO on Ag NW surface. Obviously, although this calculated temperature is a preliminary estimate, it provides some insights as to how the local heating effect contributes to joining, even though surrounding components remained near room-temperature. The estimation shows that the negligible heat energy at bulk size cannot be ignored at a nanoscale. On the contrary, if it can be manipulated well, such weak heat energy can be collected and adopted for many new applications. It is also notable that the heat is self-generated and in-situ delivered to the interfaces at a nanoscale where the interconnections are required.

The locally generated heat mainly from Cu-to-CuO-to-Cu cycle reactions would cause atom diffusion at the Cu-Ag interfaces of Ag NWs and substrate joining. It also conducts throughout the paste and promotes the joining of Ag NWs. The reduction of Ag NW surface energy due to Ag NW joining could release energy and cause secondary local heating at Ag-Ag interface for atom interdiffusion, suggesting it is also an acceleration factor to form three dimensional Ag NW networks for interconnecting the substrates.

Another considerable effect playing positive role for joining of Ag NWs in the water-based paste is the capillary force during water evaporation process. It could bring two or more NWs into close contact with their neighboring NWs. At a nanoscale, this force can generate considerable pressure at the interface of two NWs even it is fairly weak at micro scale. In terms of pressure here, it comes from the internal system originating from the capillary force or surface tension of water rather than the external pressure applying to the system to assist the joining process. Therefore, the self-

pressed process by solvent/water evaporation during joining is worth to be noted here. However, only local heating effects have been comprehensively studied in this study.

4.4.5 Local Heating Effects Induced Nanojoining

Beside of the elevated local temperature can accelerate diffusion for joining, one can expect that the reduction of organics in the pastes will also have its contribution. As suggested above, the local heating is partially from the CuO-PVP reaction by consuming the residual PVP in the water of paste to further reduce the organic content in the paste. It also consumes the PVP protection layer on the side surface of Ag NWs to activate the side surfaces. These all can reduce the organics to provide cleaner interfaces of Ag NW-NW and Ag NW-Cu for joining. Further, the local heating can also break down the unreacted PVP on the surfaces of Ag NWs to activate more clean sites for joining.

To examine if these local heating effects are sufficient to induce atomic diffusion and metallic bond formation, the interfaces of Cu-Ag and Ag-Ag were characterized using HRTEM. Figure 4.22a shows the porous structure of the interface of Cu and Ag, formed by the room-temperature pressureless joining process. The interfacial regions where the Cu surface was bonded with Ag, and Ag to Ag NW bonds formed are indicated by arrows in Figure 4.22a. The HRTEM image indicates that the Cu and Ag NW were metallurgically bonded, with the (100) plane of Ag and (111) of Cu connected in Figure 4.22b. Ag NW bonded on Cu surface and the (111) plane of Ag and (200) of Cu well matched and formed metallic bond as well, see Figure 4.22c-d, similar to that observed when using Ag nanoparticle paste as the filler material [16, 172, 173] and connected with CuO particles.

Figure 4.23a depicts the end-to-end joining of Ag NWs and the square area corresponding to Figure 4.23b. The distances of lattice fringes are 2.32 Å and 1.96 Å in agreement with (111) and (200) planes of silver [285, 286]. Ag NWs were interconnected via end-to-side or side-to-side manner and formed metallurgical bonds as well, and Figure 4.23c illustrates a tri-junction of these Ag NWs. Usually, the tips of Ag NWs have a thinner layer of PVP organics [287] which could more readily join with others because of a smaller barrier gap and higher surface energy for atomic diffusion. Although the washing process can remove or break the thin layer of PVP on the ends of Ag NWs to make it activated for joining, the side surfaces of Ag NWs are difficult to active as discussed in previous Chapter 3. Here, with the help of local heating effect, the sides of Ag NWs also started to connect under room temperature joining process as shown in the inset image of Figure 4.23d, where (200) and (220) lattices were continuous. Therefore, the local heating could break down the localized organic

layer on the side surface of the Ag NWs and promote the interdiffusion of atoms and form the joints at even room-temperature when a Cu substrate is present. The clear metallic bonding at the atomic level accounts for the good bond strength and conductivity observed during testing.

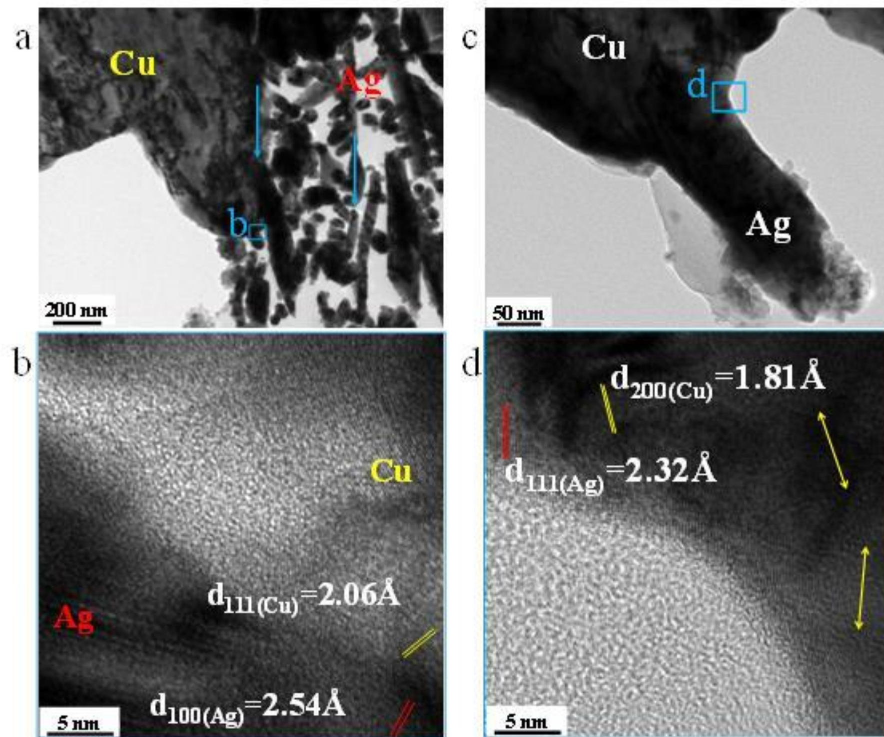

Figure 4.22 TEM images of (a) nanoporous Cu-Ag interface (arrows indicating the joining of Ag-Cu and Ag-Ag), (b) lattice image of Cu (111) -Ag (100) interface; (c) Cu-Ag interface and corresponding high-resolution image (b): lattice fringes showing the (111) plane of Ag and (200) of Cu well matched. Arrows indicating the lattice directions of polycrystalline Cu.

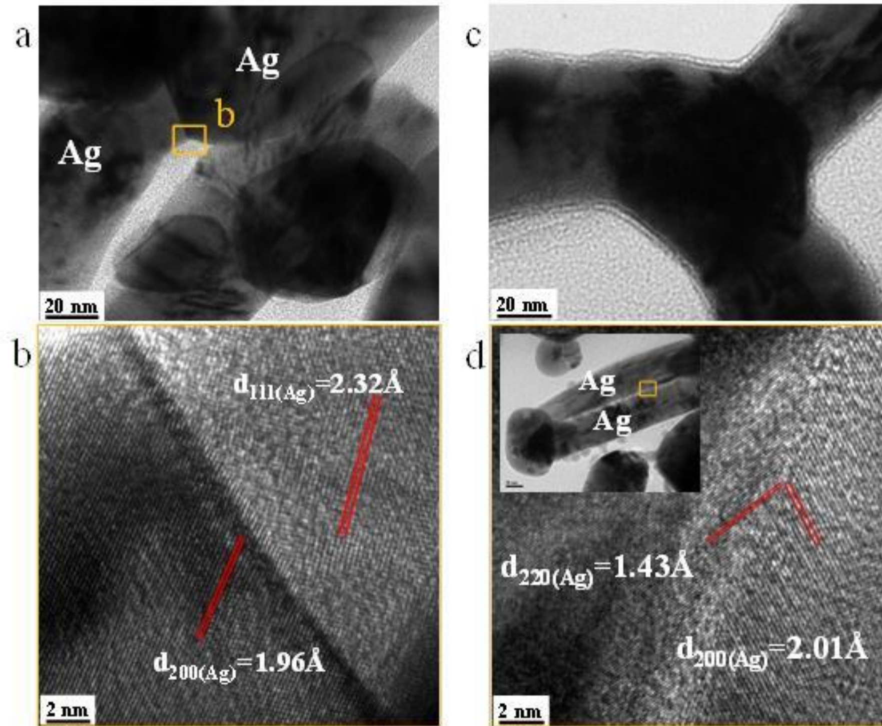

Figure 4.23 TEM images of the interface of two AgNWs of joint bonded at room-temperature (a) with end-to-end joining and square area corresponding to the high-resolution image (b); (c) tri-junction of Ag NWs and (d) lattice image of side-to-side Ag-Ag interface.

4.5 Summary and Remarks

In summary, this chapter considered the feasibility of room-temperature pressure-free joining of copper wires using water-based silver nanowire paste. A novel mechanism of self-generated local heating within the silver nanowire paste and copper substrate system promoted the joining of silver-to-silver and silver-to-copper without any external energy input. The CuO-PVP reaction could consume the residual PVP on the side surface of Ag NWs and in the water of paste to further reduce the organic content in the washed paste. The localized heat energy has been delivered in-situ to the interfaces and promoted atomic diffusion and metallic bond formation with the bulk component temperature stays near room-temperature. This local heating effect has been detected experimentally and confirmed by calculation. The use of chemically generated local heating would be an alternative method for energy in-situ delivery at micro/nanoscale.

This chapter has also shown that three-dimensional silver networks exhibit good conductivity and strength for flexible electronics packaging. Due to the porous structure, Ag NW joints have lower modulus in close to that of flexible substrates. Low modulus makes it more compatible with flexible substrates and has more capacity to absorb mechanical stresses under strain. Consequently, next chapter will focus on the mechanical properties of Ag NWs reinforced NP joints. In Particular, the improvement of strength and the mechanical behaviors of silver nanowires in NP matrix under loading will be studied.

Chapter 5
Reinforcement of Silver Nanoparticle Joints with Nanowires‡

5.1 Introduction

The use of lead alloy solder materials in the electronics industry has raised much concern due to health, environmental and safety issues worldwide [130-133]. With the development of nanotechnology, environmentally-friendly and flexible electronic products are becoming more feasible in the near term [8, 11, 135, 248, 288]. The use of metallic nanoparticles (NPs) combined with ink-jet printing processing for flexible electronics manufacturing, is a well-known technique in which the deposition and patterning are simultaneously accomplished by printing a solution of the active materials (e.g. Metallic NPs or conductive polymers), and has been widely studied [289-292]. The material deposited using an ink-jet typically consists of gold or silver NPs encapsulated within protective shells and dispersed in a liquid solvent [293, 294]. Recently, nanoscale diffusion bonding using metallic nanomaterials has displayed significant advantages over conventional soldering or adhesive bonding, such as lower bonding temperatures and higher diffusion rate [13]. Hence, low temperature interconnection processes using metallic NP paste appears to be a promising alternative for Pb-free electronic packaging and flexible electronic interconnections [172, 295]. For example, several studies have focused on low temperature joining technology for lead-free packaging or power modules using NPs made from silver [173, 296], copper [297] and gold [19], respectively. The sintering of silver NPs and their bonding to copper wires and substrates to form a 3-dimensional bonded network which can withstand higher working temperatures through further sintering has been reported by Hu *et al.* [172] and Alarifi *et al.* [16]. The typical sintering temperature ranges from 150 ~ 300 ℃ are lower than the melting point of the corresponding bulk materials, due to the size effect of NPs [71]. However, pressure is required to facilitate the bonding processing in these studies, which is still inconvenient for industrial applications.

Recently, there is increasing interest in applications of one dimensional micro-sized / nano-sized materials, for example, developing multifunctional composite materials incorporating second phase fibers and/or whiskers [298-304]. Mullite fibers were added in carbon materials, which fibers bend and fracture to several fragments that could partially carry the applied loading [305]. For a solder

‡ Portions of this study also appear in: Peng, P., et al., Reinforcement of Ag nanoparticle paste with nanowires for low temperature pressureless bonding. *Journal of Materials Science*, 2012. 47(19): p. 6801-6811.

material, Coughlin *et al.* reported that Ni-Ti shape memory alloy fibers embedded into a Sn rich solder alloy could improve fatigue and mechanical shock properties of the materials by a super-elasticity transformation property of the fibers on loading [306]. Ongoing efforts are being made to study the sintering of nanowires, nanorods and nanobelts, in order to further exploit the unique properties of these materials [307-311]. However, few have examined the behavior of metallic joints when nanowires are introduced as a second phase in the bonding material.

This section will focus on a low temperature pressureless joining process for robust wire to wire bonding of copper by introducing silver nanowires (Ag NW) into a silver nanoparticle (Ag NP) paste as filler materials. The sintering behaviors of Ag NP/NW binary pastes and mechanical properties of bonded joints, furthermore, the reinforcement effect of Ag NW in the joints will be discussed.

5.2 Experimental

5.2.1 Synthesis of Ag NPs and NWs

All the chemicals and reagents were of analytical grade and used in the as received form without any purification. The synthesis of the Ag NP material involved reacting silver nitrate ($AgNO_3$, Alfa Aesar) and sodium citrate ($C_6H_5O_7Na_3 \cdot 2H_2O$, Alfa Aesar) at 80~90$^oC$ [16]. Ag NWs were prepared in a polyol solution with polyvinylpyrrolidone (PVP) as a structure directing reagent using a method modified from the literature [66, 67]. In this study, 330 mg polyvinylpyrrolidone or PVP ($(C_6H_9NO)_n$, K25, M.W.= 24000, Alfa Aesar) and 12.5 mg silver chloride (AgCl, Alfa Aesar) were mixed with 40 ml ethylene glycol (EG, Fisher Chemical) in a round-bottom flask. The mixture was heated to between 160 and170 ^oC. Then, 110 mg silver nitrate was dissolved in 10 ml ethylene glycol liquid and added into the mixed solution while stirring vigorously and continuing the reaction conditions for 4 hours. The Ag NPs and Ag NWs were condensed by centrifugation at 4000 rpm using a 50 ml centrifuge pipe. The clean supernatants were removed from the centrifuge pipes using a pipette resulting in highly concentrated Ag NP and Ag NW pastes. The excess PVPs in Ag NWs could be washed and removed by deionized (DI) water and repeated centrifugation. 0%, 10%, 20% and 30% volume fractions of Ag NW paste were mixed with Ag NP paste in 20 ml glass vials by stirring and are designated as AgNP, AgNP/10NW, AgNP/20NW and AgNP/30NW, respectively.

5.2.2 Joining using Ag NP-NW Binary Pastes

The copper wires (99.9 % purity) used in this work, from Arcor Electronics, Northbrook, IL, were 250 μm in diameter. Prior to bonding, the wires were cut into 60 mm pieces and ultrasonically cleaned in acetone for 3 minutes to remove the organics, 1% diluted $AgNO_3$ for 1 minute to remove the oxide layer and rinsed in ultrapure water (electrical resistivity approximately 18 MΩ·cm). A fine needle attached on a 10 ml syringe was used to place the Ag nanopaste between two clean copper wires on a 60 °C hotplate surface. After depositing 0.05 ml Ag nanopaste, the assembly of copper wires and paste was heated at 60~200 °C in air for 1 hour without bonding pressure.

5.2.3 Tensile Testing

Tensile shear testing was conducted by loading the wires in the axial direction at a rate of 0.5 mm/min using a micro tensile tester (Instron 5548, UK). Figure 5.1 illustrates the schematic diagram of the tensile shear test samples used to investigate the mechanical performance of the bonded samples. After clamping each bonded sample into the grips as shown in Figure 5.1, loading was applied. The measured strength of joints is the tensile shear strength due to the applied shear stress during the tensile testing, because two Cu wires were not coaxial. It was estimated by dividing the highest failure force value by the bonding area [297, 312, 313] $\sigma = F_{max}/A$ (N/mm^2 or MPa). The fracture area of samples was difficult to measure due to the unsymmetrical geometry of fracture region. Here, the average bonding area was estimated to normalize the actual fracture area, which bonding area A was calculated by multiplying the maximum bonding length L by thickness D of the Ag bonding material.

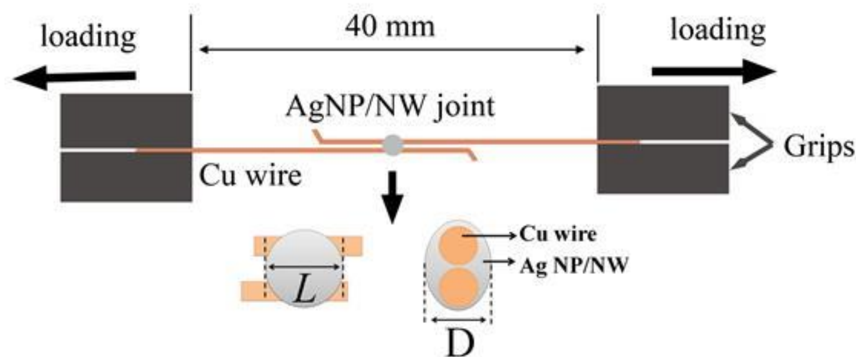

Figure 5.1 Schematic illustration of tensile shear strength testing of bonded samples. The starting distance between the grips was fixed at 40 mm, L and D denote the bonding length and thickness of joint.

5.2.4 Nanoindentation

The mechanical properties of silver npm were tested with a depth-sensing nanoindenter (Hysitron Triboindenter) equipped with a Berkovich tip. The tip was calibrated on fused silica. Indentations were performed on the mechanically polished flat surfaces in a load controlled mode. All nanoindentation experiments were performed using a constant loading rate of 60 μN/s, with loads of 600 μN. A minimum of 5 indents for each load were collected for each sample.

5.2.5 Microstructure Characterization

The cross sections of bonded samples were mounted using epoxy resin and polished with 1 μm Al_2O_3 powder. Optical microscopy (Olympus BX 51M, Japan) and field-emission scanning electron microscope (Leo 1530 FE-SEM; Zeiss, Germany) were used to study the microstructure of cross sections, interfaces and fracture surfaces of bonded samples. Energy-dispersive X-ray spectroscopy (EDX, EDAX Pegasus 1200) was employed for elemental analysis. The sintered Ag NPs and Ag NP/NW were also observed using SEM.

5.3 Results

5.3.1 Microstructures of Sintered Ag NPs and Ag NWs

Figure 5.2 shows the microstructures of Ag NP and Ag NW pastes after centrifuging. Figure 5.2 a and b are low magnification SEM images of as-centrifuged Ag NP and Ag NW pastes. The Ag NPs were 50 to 100 nm in size, with polyhedron morphology as shown in Figure 5.2c. The Ag NWs had a pentagonal shape as shown in Figure 5.2d with lengths of 8 to 15 μm and 50 to 100 nm in thickness. Few Ag NPs were also observed in the Ag NW paste synthesized by the polyol method.

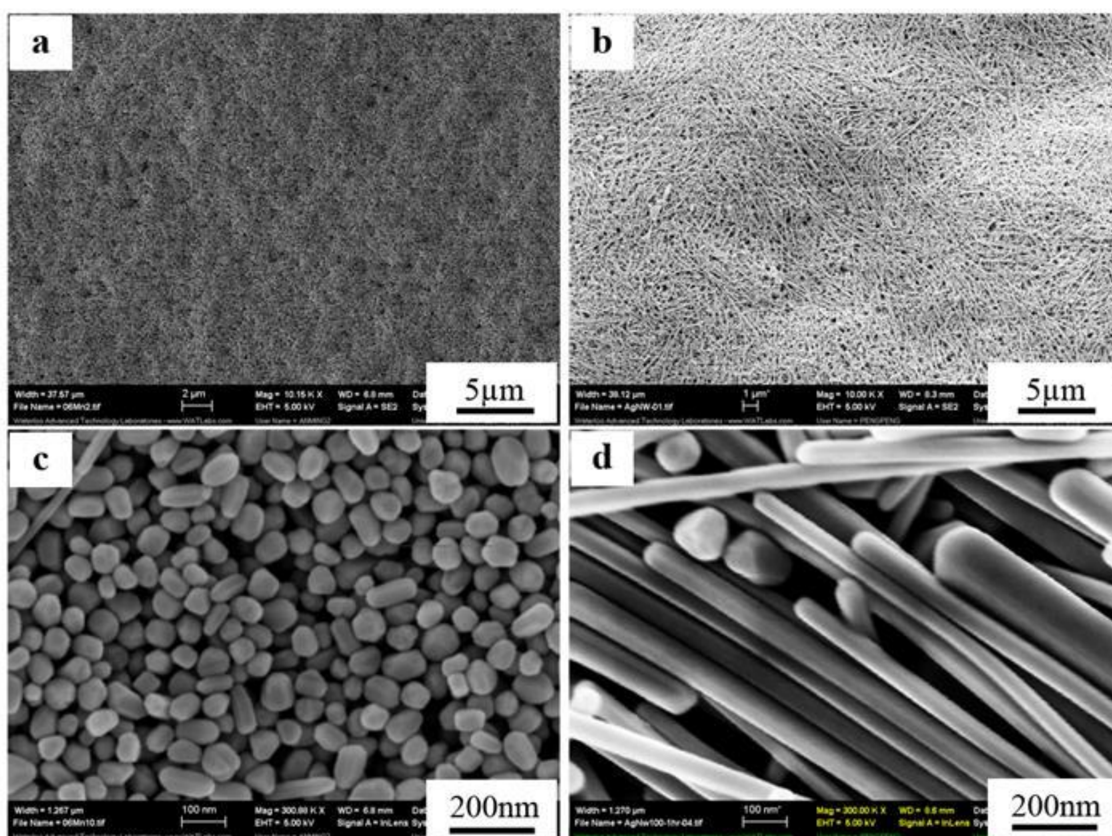

Figure 5.2 Microstructure of condensed (a) AgNP and (b) AgNW paste after centrifuging. High magnification SEM images of (c) polyhedron shaped Ag NPs and (d) pentagon shaped Ag NWs with length of 10-20 μm and 50-100 nm thickness.

The Ag NP/NW pastes were sintered at different temperatures to investigate the sintering behaviours of these mixtures at low temperature as shown in Figure 5.3. For comparison, unsintered Ag NP/20NW binary paste is shown in Figure 5.3a. The microstructures of Ag NP/20NW binary pastes sintered at 60 ^{o}C, 100 ^{o}C, 150 ^{o}C and 200 ^{o}C for 1 hour, respectively are shown in Figure 5.3b-e. The average width of bridge paths between adjacent Ag NP-NP and Ag NP-NW grew from 26$\pm$2 to 54$\pm$4 nm (average of five measured values) as temperature increasing from 60 to 200 ^{o}C as indicated by the arrows in Fig. 2b and 2e; which is consistent with the increased rate of solid state diffusion and growth of bridge paths expected when the temperature increases. It is worth mentioning that residual PVP from the synthesis process of the Ag NWs, and amorphous citrate complexes from the synthesis process of Ag NPs could be present at the interfaces of the particles and influence the sintering of the paste. Although PVP does not readily decompose below 300 ^{o}C [216, 217], the majority of this material

would be removed during the process of washing with DI water as previously shown when the PVP coating was washed from Cu NPs [297]. As such, it would be expected that the particle surface free of PVP is active for low temperature sintering. The amorphous citrate complexes on the surfaces of the Ag NPs will readily vaporize and decompose (at temperatures above 90 ^{o}C) and should completely disappear during low temperature sintering [172, 314, 315]. This accounts for the rapid formation and growth of bridges even at temperatures of 100 to 150 ^{o}C. Sintered Ag NP/NW mixed pastes with various additions of Ag NWs at 150 ^{o}C are also shown in Figure 5.3f, g, i, corresponding to 0%, 10% and 30% Ag NWs by volume in the pastes (20% is shown in Figure 5.3d). Based on the dispersion of the Ag NWs, it is clear they did not aggregate together and were uniformly dispersed in the Ag NP paste by stirring. The inset images of Figure 5.3g and 2i illustrate the morphology of 10% Ag NW and 30% Ag NW at a low magnification. Introducing a large fraction of Ag NWs can change the packing of the nanomaterials in joints since spherical particles can be packed more densely than long wires. This leads to the presence of a higher degree of porosity in the sintered 30% NW paste as shown in the inset Figure 5.3j, compared with the paste containing 10% Ag NW(see Figure 5.3h).

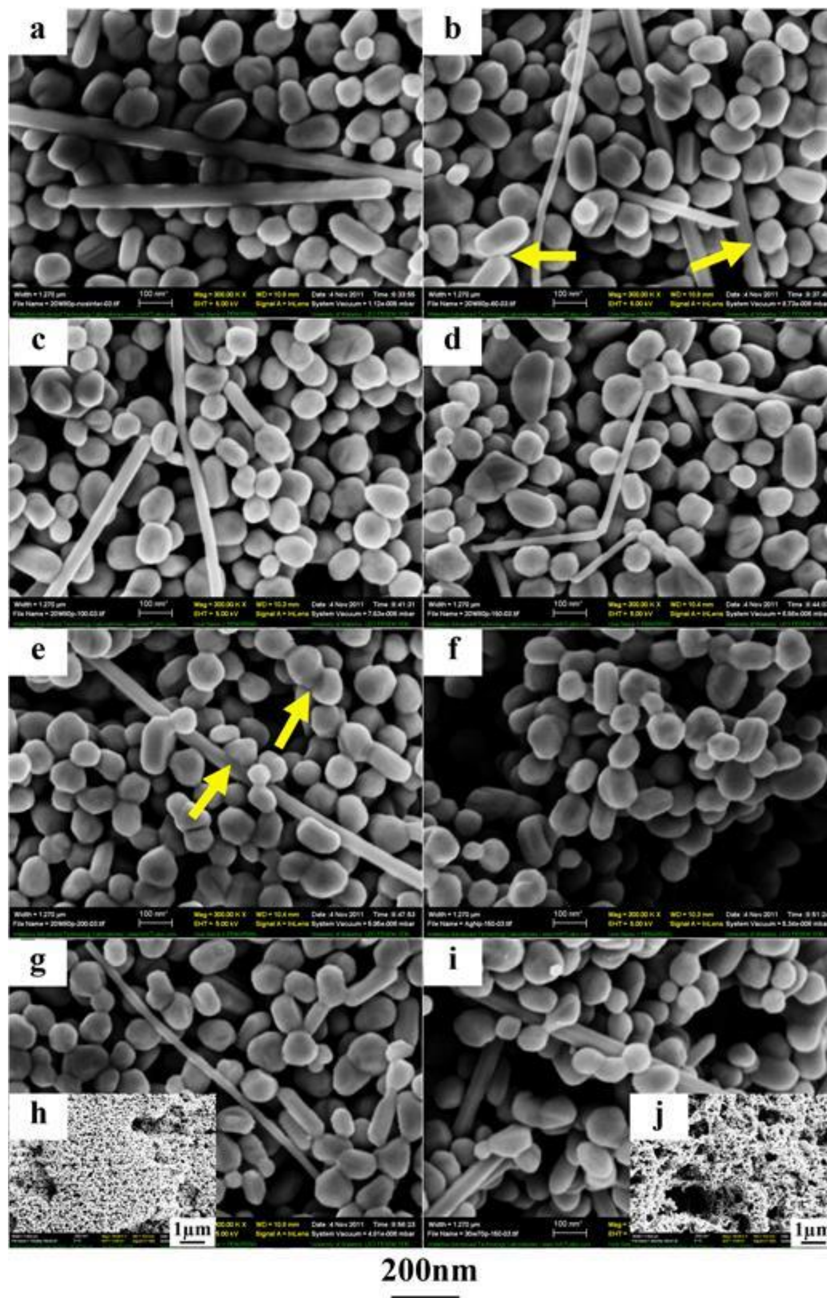

Figure 5.3 SEM images of Ag NP/NW paste sintered at different temperatures: (a) unsintered Ag NP/20NW paste, and sintered Ag NP/20NW paste at (b) 60 ^{o}C, (c) 100 ^{o}C, (d) 150 ^{o}C and (e) 200 ^{o}C for 1 hour with arrows highlighting the bridge paths between NP-NP and NP-NW. Sintered paste with different Ag NW volume additions (f) 0 vol.%, (g) 10 vol.% and (i) 30 vol.% after sintering at 150 oC for 1 hour. Inset low magnification image (h) and (j) are corresponding to Ag NP/10NW and Ag NP/30NW pastes.

5.3.2 Mechanical Properties

Two predominant fracture modes were observed during testing, one being filler material fracture (failure of the sintered AgNP/NW) as shown in Figure 5.4a, and the other was interfacial fracture at the Cu-Ag interface with one wire being pulled out of the sintered Ag bond material under loading, as shown in Figure 5.4b. The fracture modes of all test samples bonded at different temperatures are summarized in Table 5.1. Filler material fracture was usually observed when 0% and 30% Ag NW was introduced. The samples tested using Ag NP paste with 10 or 20% NW all involved failure by interfacial debonding. In addition to these failure modes, fracture of the Cu wire occurred in the sample bonded using Ag NP/20NW paste which was sintered at 200 °C.

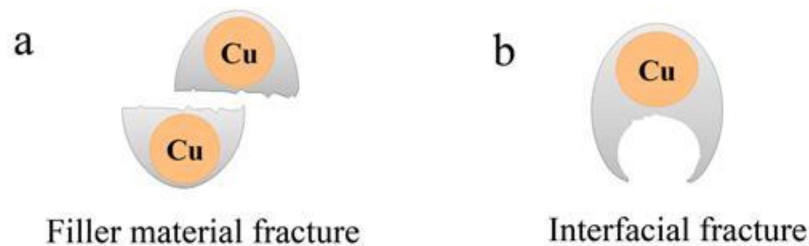

Figure 5.4 During testing, two fracture modes for various NW contents: (a) filler material fracture and (b) interfacial fracture on the Cu wire and Ag nanopaste joint interface.

Table 5.1 The fracture modes for bonded joints with various AgNW contents at different temperatures.

Temperature	Ag NP	Ag NP/10NW	Ag NP/20NW	Ag NP/30NW
60℃	F*	I	I	F
100℃	F, I	I	I	F, I
150℃	F	I	I	F
200℃	F, I	I	I, W	F

(* F, I and W denote the filler material fracture, interfacial fracture and wire fracture.)

The strength of bonded samples as a function of Ag NW volume fraction in the silver paste at different bonding temperatures is presented in Figure 5.5a. The remarkable improvement in joint tensile shear strength is suggested to be the result of reinforcement provided by the Ag NWs when 100 and 150 °C sintering temperatures are used. The addition of 10 or 20% volume fraction of Ag NW to the Ag NP paste increased the joint strength by 18 to 81% when the same sintering temperatures are applied. However, the strength decreased considerably when 30% Ag NWs were

used due to the porous structure produced in the joint, as shown in Figure 5.3j. The highest strength increase was obtained using 20% Ag NWs by volume, providing an improvement of 50 to 80% after sintering at 60 and 100 ^{o}C bonding temperatures. Figure 5.5b shows the strength of bonded joints with AgNP/20NW binary pastes and Ag NP paste as a function of bonding temperature. The presence of 20% NW in the bonded joints clearly increased the failure strength compared to those without Ag NW addition at all bonding temperatures investigated. For comparison, the Cu wires were also joined by soldering (using commercial 60Sn-40Pb solder) at 200 ^{o}C, and this joint achieved a strength of 9.9$\pm$0.4 MPa compared to 16.4$\pm$0.4 MPa and 13.9$\pm$0.5 MPa achieved using AgNP/20NW binary pastes and Ag NP paste respectively. Prior studies investigating bonding with other paste materials have also reported lower strengths when using Cu NPs (10 MPa) [297] or Ag NPs (8 MPa) applied with 5 MPa pressure [172]. A mean tensile shear strength of 3.2$\pm$0.8 MPa was obtained near room-temperature (60 ^{o}C) using Ag NP/20NW binary pastes. The incorporation of 10 to 20% Ag NWs improved the strength of joints and shifted the failure area to the Cu-Ag interface instead of within the sintered silver, due to the reinforcement of the sintered material by the nanowires.

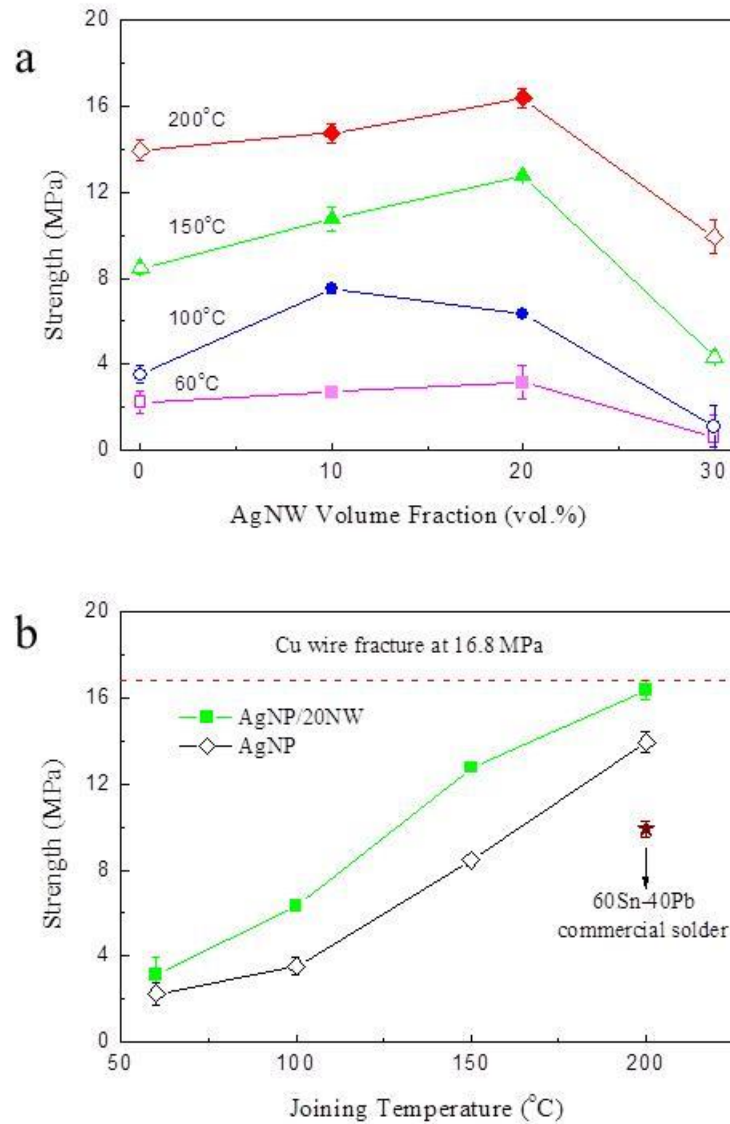

Figure 5.5 (a) Bond strength of bonded samples as a function of Ag NW volume fraction at different bonding temperatures. Squares, circles, triangles and diamonds represent tested samples bonded at 60°C, 100°C, 150°C and 200°C, respectively. Open and closed symbols, representing the filler material fracture and interfacial fracture, indicate the dominated fracture mode of bonded samples with various Ag NW contents. The dashed line denotes the fracture strength of copper wires. (b) The fracture strength of bonded samples of Ag NP/20NW and Ag NP pastes as a function of joining temperature. Star represents 60% Tin/40% lead commercial solder joint soldered at 200°C.

The elastic modulus and nanohardness of these porous materials were characterized by nanoindentation on mechanically polished Ag NP-NW joints. The typical load-depth curves are shown in Figure 5.6. The maximum depth increased with increasing of Ag NW fraction because high porosity was induced by adding more NWs. The relative density, elastic modulus and nanohardness decreased with increasing of Ag NW fraction, see Table 5.2. The reduced elastic modulus and nanohardness of Ag NP-NW porous materials suggests a good mechanical compatibility with flexible substrates, which would aid in relieving the thermomechanical stress during practical applications (as previously discussed in Section 4.3.4).

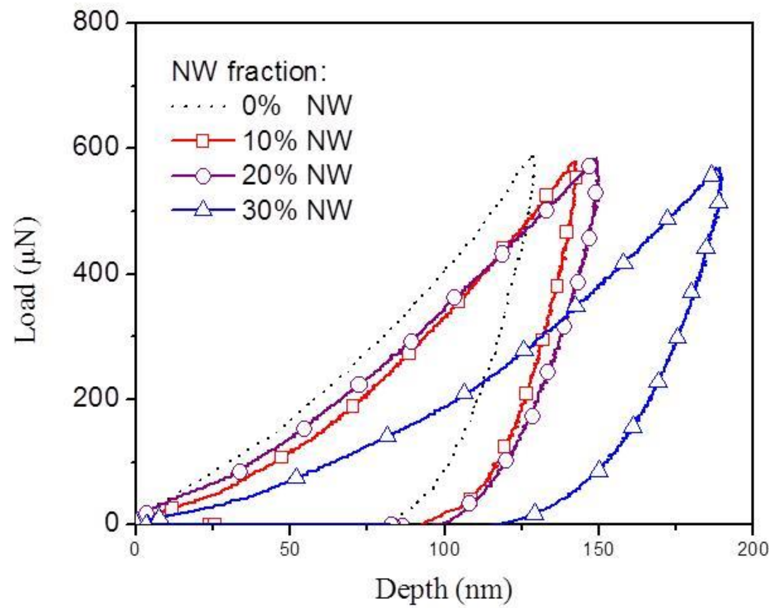

Figure 5.6 Typical load-depth curves of Ag NP-NW porous materials with different NW fractions.

Table 5.2 Relative density, elastic modulus and nanohardness of Ag NP-NW porous materials (joining at 60°C).

NW Fraction (vol.%)	Relative Density (%)	Elastic Modulus (GPa)	Nanohardness (GPa)
0	54 ±11	27.74 ±1.23	1.01 ±0.05
10	53 ±19	27.27 ±3.42	0.99 ±0.20
20	48 ±15	22.57 ±2.09	0.79 ±0.04
30	43 ±17	17.55 ±2.95	0.64 ±0.12

5.3.3 Fracture Behaviours of Joints

To investigate the fracture mechanism of the sintered Ag NP/NW material, the fracture surfaces were examined by SEM. Figure 5.7a-d show the SEM images of the secondary cracks produced perpendicular to the fracture surfaces in joints bonded at 150 °C with Ag NW volume fractions from 0% to 30%. The regions reveal the role of the NW in the fracture of the bonding material, since the primary crack cannot be readily characterized after failure. With the volume fraction of Ag NWs increasing from 10% to 30%, progressively more crack bridging by the nanowires occurs. Crack propagation is suppressed by bridging of the nanowires, in a similar way to fibre reinforced composites [305]. Since each Ag NW was bonded with several Ag NPs, this reduced the tendency for pull out of the NW. Clear evidence of plastic deformation of individual Ag NW was observed as shown in Figure 5.7c. The fractured joints with 30% Ag NW addition exhibited a much lower density of particles than those with 10 to 20% Ag NW addition, due to the highly porous sintered structure discussed earlier (see Figure 5.3 h&j). This accounts for the dramatically decreased bond strength when a 30% Ag NW volume fraction was used (see Figure 5.5a), which also hampered the sintering process at lower temperatures. Moreover, the weaker bond strength between Cu wire and Ag NW compared to Cu and Ag NP is likely attributed to the lower interfacial bonded area resulting from the high porosity.

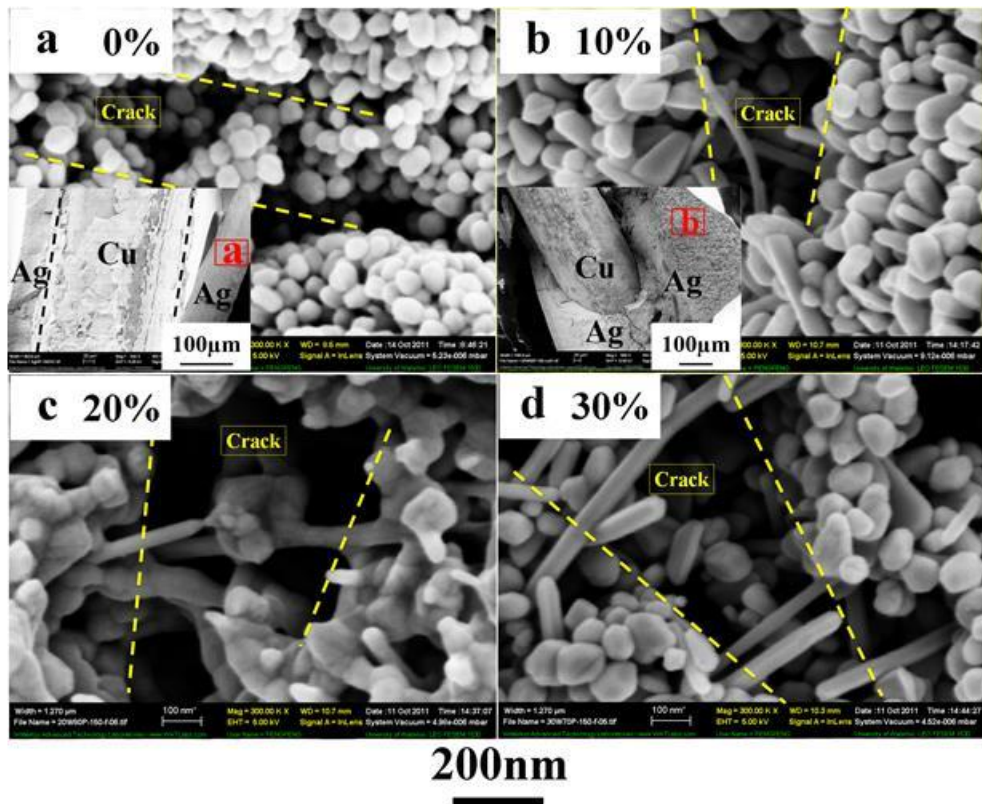

Figure 5.7 Microstructure of fracture Ag surface of NW reinforced Ag NP joints bonded at 150℃ with various Ag NW contents from (a) 0 vol.%, (b) 10 vol.%, (c) 20 vol.% to (d) 30 vol.%. Cracks are indicated by dashed lines.

The cross-sections of fractured joints bonded with Ag NP/20NW paste are shown in Figure 5.8. Figure 5.8 (a-c) are taken by optical microscopy while Figure 5.8 (d-f) are SEM images of the bonded interface. In Figure 5.8a, pull-out of the Cu wire is clearly identified by the dashed circle indicating the original location of the second Cu wire. Some residual Ag can be observed on the surface of the Cu wire after testing as indicated in Figure 5.8b. The bond interface of Cu-Ag is clearly shown in Figure 5.8c and the pores observed may be due to a locally unbonded area resulting from air bubbles introduced in the paste during bonding or an oxide layer on the Cu surface. A joint cross section free of microporosity using Ag NP/20NW binary pastes was observed, see Figure 5.8d, similar to the pressure bonded joints using Ag NPs [16, 180]. However, the presence of nanopores is general in the joint with low temperature pressureless bonding. In the interface as shown in Figure 5.8e, the metallurgical bond between the Cu wire and the Ag paste was found to be continuous. The backscattered electron SEM image Figure 5.8f indicates continuity along the Cu / Ag interface. A

region below the dashed line with 1 μm in thickness which is actually raised from the surface considering the scratches on the surface formed during the polishing process. This surface relief is common in metallographic samples where a phase is slightly harder, such as an intermetallic compounded, and is not removed as much as the softer Ag or Cu. It is believed that the interdiffusion of Ag and Cu atoms occur along the interface formed a mixed region or interphase boundary layer at the interface [259].

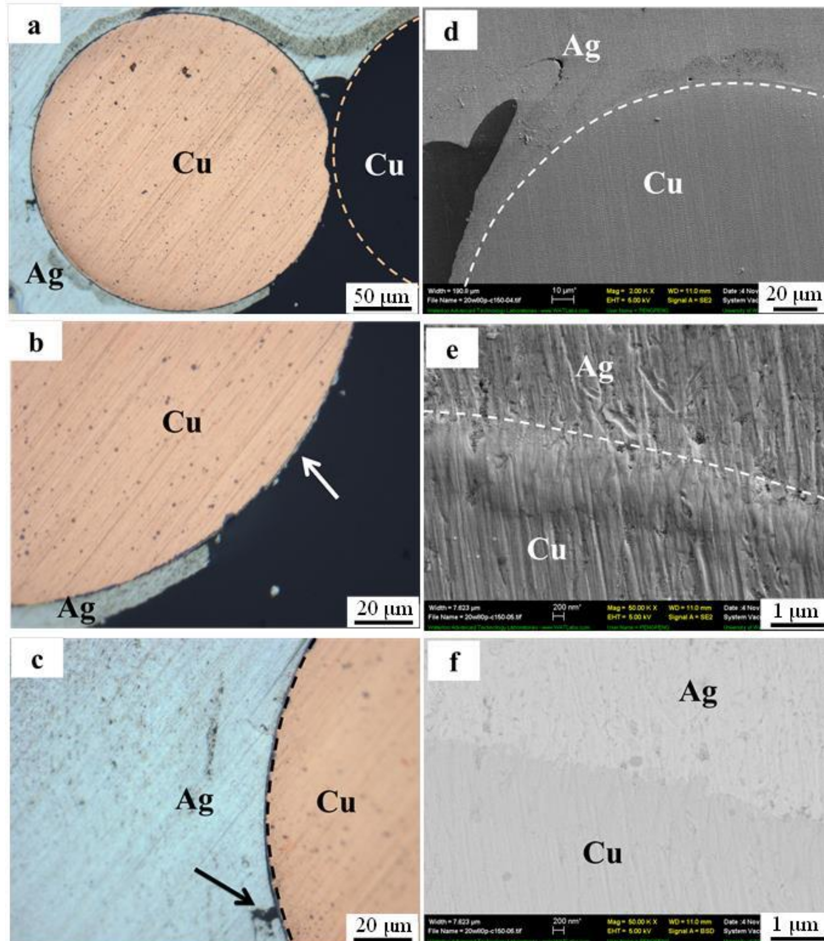

Figure 5.8 Microstructures of cross sections of AgNP/20NW paste bonded Cu-Cu joints: The pulled out Cu wire can be identified by dashed line in an optical microscope image (a). (b) Ag matrix attached on the surface of bare Cu wire and (c) bonded interface of Cu-Ag with pore highlighted by arrow. Right column: (d) SEM image of bonded interface of cross section; (e) High magnification of interface shows lack of gap or debonding area between the Ag sintered nanomaterials and Cu wire; (f) The backscattered electronic SEM image for the interface, dark area denoting the Cu and bright area for Ag.

To further study the Cu-Ag interface characteristics, the fractured joints bonded with Ag NP/20NW binary pastes were investigated by SEM and EDX. Figure 5.9a was taken from the fractured interface on Ag filler material side (as schematic illustrated in Figure 5.4b) and Figure 5.9b was from the surface of pulled-out Cu wire with residual Ag NPs and Ag NWs. Three different spots with different microstructures on both sides were studied using EDX. The results shown in Table 5.3 indicated that Cu and Ag elements existed on both sides, which supports the notion that interdiffusion occurred and metallic bonding is present at the Ag and Cu interface during low temperature pressureless sintering, similar to previous findings [172].

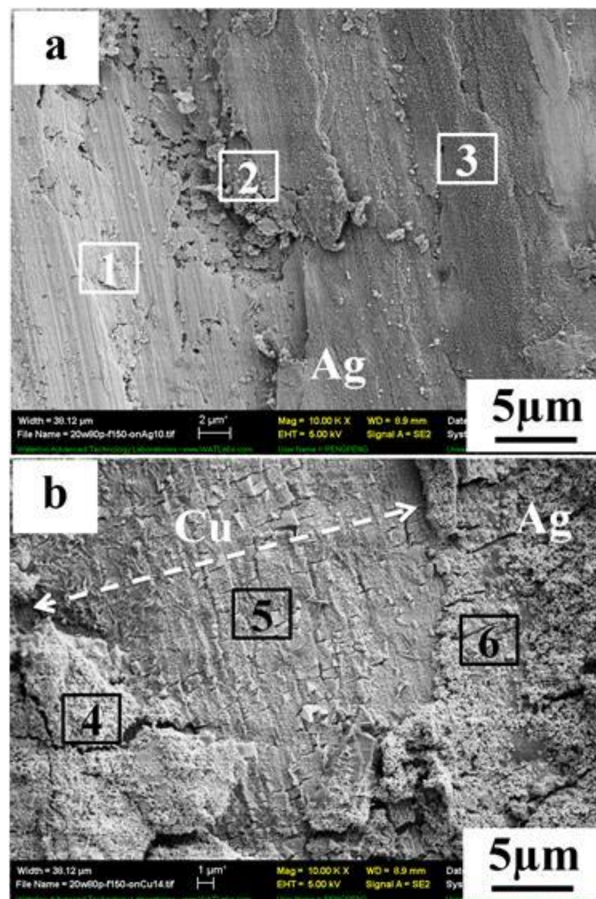

Figure 5.9 SEM images of Cu-Ag interface: (a) AgNP/20NW paste side with labelled 1, 2, 3 three points of interest, (b) Cu wire side with 4, 5, 6 points of interest, dotted line with arrows indicating the Cu wire.

Table 5.3 EDX results of selected points on two different sides of the interface of a joint bonded with AgNP/20NW paste at 150 ^{o}C

Interface	Numbers	O (At%)	Cu (At%)	Ag (At%)
Ag side	1	11	6	83
	2	--	34	66
	3	15	66	19
Cu side	4	--	7	93
	5	--	98	2
	6	--	78	22

5.4 Discussion

5.4.1 Fracture Energy

The load-displacement curves of bonded samples using Ag NP and Ag NP/NW also reveal some key aspects which control the bonding strength. Typically, the load-displacement curves of the joints produced using Ag NP/10NW paste developed a stepwise profile, and were distinct from that of Ag NP paste bonded joints even though similar maximum failure forces are produced, see Figure 5.10. It is speculated that the stepwise failure is due to the integrative effects of debonding on Ag NP-NP, NW-NP and NW-NW interfaces, and breaking of the Ag NWs. The quality of the joints can also be evaluated by comparing the bonding energy per unit area or fracture energy [257], i.e., the integrated area under the force-displacement curve shown in Figure 5.10 divided by bonding area (the unit is thus in J/m^2 or N/m). It was found that the fracture energy of the Ag NP/10NW bonded at 60 ^{o}C was about three times larger than that of the Ag NP joint, although they had similar maximum failure load and bonding area. A larger integrated area requires more energy dissipation during fracture and thus yields higher quality of joints which are more damage tolerant [258, 259].

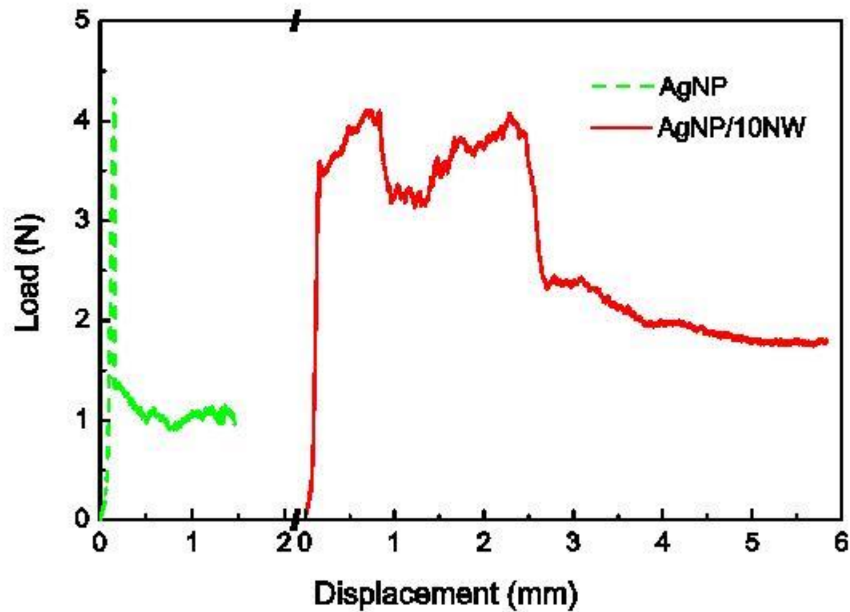

Figure 5.10 Typical load-displacement curves of bonded joints: solid line for AgNP/10NW and dashed line for Ag NP.

5.4.2 Reinforcement Mechanisms

To study the behaviour of Ag NWs in joints bonded with Ag NP/NW pastes, the fracture surfaces of tested joints were characterized by SEM. Four different morphologies of Ag NWs were identified on the fracture surfaces and crack areas in Figure 5.11. The Ag NWs can be bent (Figure 5.11a) and pulled out (Figure 5.11b). In Figure 5.11b, some residual nanoparticles highlighted by arrows attached to the end of a pulled-out Ag NW indicate that the debonding of Ag NP-NW actually occurs within the paste matrix. This demonstrates that the Ag NP and Ag NW bonding strength is relatively weak. Morphological features found on the fracture surface included necking of the Ag NWs as highlighted by the arrows in Figure 5.11c and even breaking as shown in the circles of Figure 5.11d. These phenomena are all likely to occur simultaneously due to the wide range of stress distributions in the NW which are randomly oriented. In Figure 5.11e a pair of bent and fractured Ag NW fragments is evident, and even bending and plastic deformation zones in a NW are observed in Figure 5.11f, with the necked regions highlighted by arrows. Due to the nano-scale effects, one would expect that the wires should have extremely high strength, and that little plastic deformation will occur since the slip process will be limited [102]. Overall, a rather small area reduction was observed at

the NW fracture surfaces, and this appears consistent with numerical modelling of 20 nm thick NW also suggests that fracture will be rather brittle when their length is over 1.5 μm [316]. Nevertheless, the NW second phase has a high strength, and is crucial for reinforcement in these bonded joints.

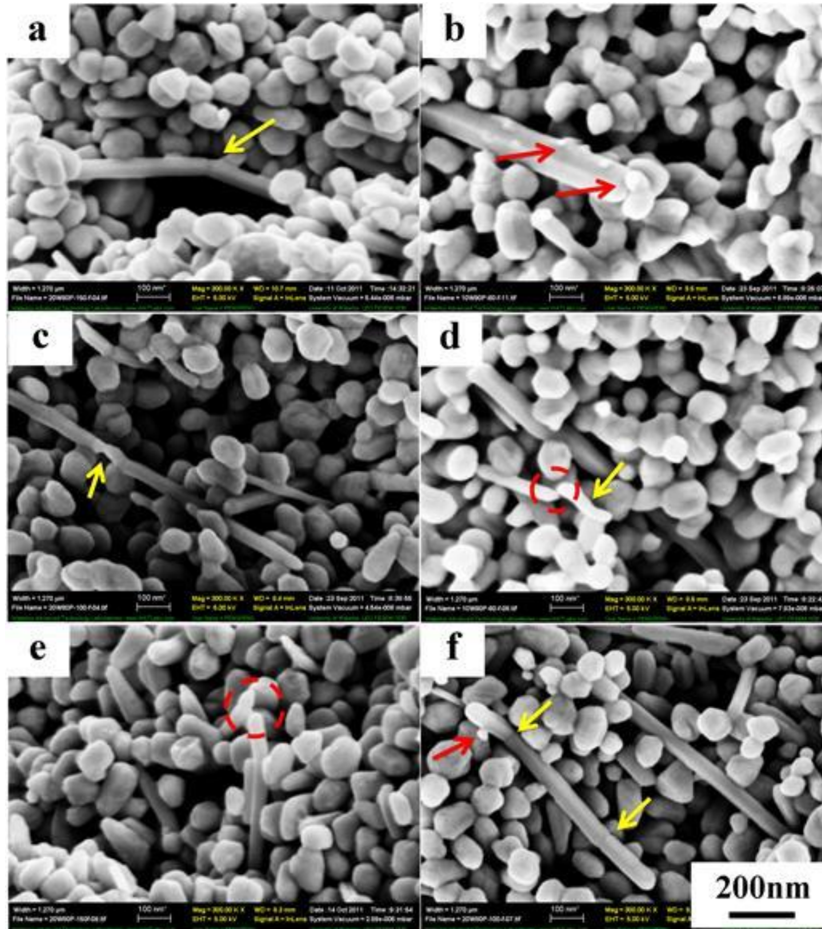

Figure 5.11 SEM images of silver nanowires in joints after testing: (a) NW bent under stress with arrow indicating the bend region; (b) NW pullout, arrows highlighting residual NPs attached on the top and wall of NW; (c) Plastic deformation of NW with deformation regions highlighted by arrows; (d) NWs broken under stress, deformation region in the NW is shown. Not individually, the combined actions of Ag NWs are illustrated: (e) Bent NW was broken into two wires under stress, the fracture areas stayed in the circle; (f) NW was bent and pulled out, plastic deformation zones are highlighted by arrows. Dashed lines indicate the cracks.

In comparison, the 0% NW sample exhibited fracture surface dominated by NP with few bonded points, and so the above noted behaviours of Ag NWs were not available to dissipate the

fracture energy during loading, leading to inferior strength and toughness. A schematic representation of the mechanisms occurring during fracture is illustrated in Figure 5.12 which summarizes the reinforcement mechanisms provided by NWs in the bonded joints. In Figure 5.12a, the inter-particle forces cause crack blunting by NP-NP debonding and crack widening if the stress on at the crack tip is larger than the NP-NP debonding force [317, 318]. While the crack grows in the vicinity of NWs, the crack-opening stress could be released along the NW and form a local compressive stress which bends the NW as shown in Figure 5.12b. The strain and energy required for bending of a NW will suppress the propagation of cracks or cause the crack deflection effectively reinforcing the joint [319, 320]. If the bonding strength of NP-NW is larger than the yield strength of NW, then deformation or even breakage of the NW could occur under loading (Figure 5.12c). In the case that bonding with the NP matrix is poor around a NW, it could also be pulled out by the debonding of NP-NW and NP-NP interfaces in Figure 5.12d. After an NW has been pulled out, a new smaller crack is easily to be generated and propagated along the debonding plane. Both crack closure and creation will dissipate the external fracture energy and thereby improve the strength of joint [321-323].

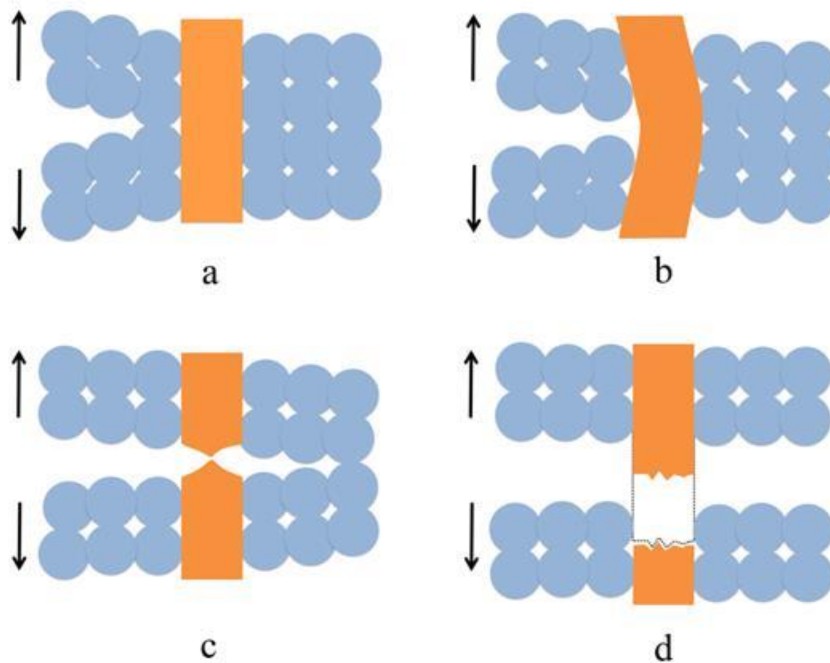

Figure 5.12. Schematic mechanisms of AgNWs reinforcement in AgNP/NW joints: (a) Energy absorption causing crack closure by NP-NP debonding and crack propagation. (NP-NP bond < stress on crack tip); (b) While the crack grows in front of AgNW, the deformation splits along the NW and forms a compressive stress then bends the NW. The dispersed strain and energy consumption of bending NW stops the crack propagation or causes crack deflection. (Stress on crack tip < NW yield strength < NP-NW bond); (c) Deformation or even breaking of NW. (NW yield strength < Stress on crack tip < NP-NW bond); (d) NW being pulled out by debonding of NP-NW and further diversion of the crack. (NP-NW bond < Stress on crack tip). New generated smaller crack can propagate in the debonded areas.

5.5 Summary and Remarks

In summary, a unique method for interconnecting of copper wires using silver nanoparticle and nanowire binary pastes has been examined in this chapter, in which joining was accomplished from 60 to 200 ^{o}C and yet without the application of pressure. Joining was facilitated by solid state sintering of Ag nanomaterials and metallic bonding between Cu-Ag interfaces. The effects of different additions of Ag nanowires in joints were studied, in which addition of 20 vol.% Ag nanowires improved joint strength after low temperature joining by 50~80% compared with Ag nanoparticle paste. A mechanical reinforcement effect due to introduction of Ag nanowires has been

confirmed by observation of the fracture path propagation, where necking, breakage and pullout of nanowires occur on loading. This low temperature pressure-free joining technology has the potential for wide use for interconnection in lead-free microcircuits and flexible electronic packaging.

This chapter has demonstrated that Ag NWs could be introduced into the NP matrix to function as a second phase to reinforce both the strength and fracture toughness even with a low weight percentage. It helps with understanding the mechanical behavior of Ag NWs under loading. The low temperature pressure-free joining process with Ag NP/NW mixed pastes appears to be an alternative for conventional lead alloy solders for flexible electronics interconnections and lead-free microelectronics packaging.

Chapter 6
Conclusions and Recommendations for Future Work

6.1 Conclusions

As concluding remarks, the objective of this thesis work has been to study the joining of silver nanowires (Ag NWs) at low temperatures and their applications, with reference to joining processes and mechanical properties as the two main metallurgical issues. Room-temperature joining of Ag NWs was performed to examine the joining behaviors associating with individual Ag NWs and Ag NW pastes. The mechanisms contributing to metallic bond formation between Ag NWs and Ag NWs to copper (Cu) substrates were investigated. The mechanical properties were studied including Ag NW joints and Ag NWs in nanoparticle (NP) matrices for establishing a processing-structure-property relationship of Ag NW materials.

Based on the experimental studies, the conclusions can be drawn as follows:

(1) A new strategy has been discovered to interconnect individual Ag NWs through selective surface activation process. Ag NW joints with similar angles have been obtained through selectively activating of contacting surfaces by washing processes using water, ethanol and acetone. Due to the weaker adsorption of PVP on {111} facets, it could be removed from the end surface of Ag NWs which made the {111} facets exposed and activated for joining. Due to the high surface diffusion rate at nanoscale due to nano size effect, much smaller separation gap and unimpeded diffusion channels by removal of PVP barrier layers, bared Ag NW ends could self-orientationally attach and join with counterparts in centre-to-edge configuration through action of obtain high diffusion rate edge sites. Monocrystalline V-shaped or *zig-zag* prisms terminated by twin boundaries and free surface have been formed by self-oriented joining. This surface selective activation process for joining of Ag NWs has potential applications for building up nano-circuits. These joined regions have similar crystal orientations and will be a novel structure for investigating the one dimensional transport properties in curved Ag NWs.

(2) Water-based Ag NW paste has been successfully used as a filler material for flexible electronic packaging at room temperature without joining pressure. Organic contents were reduced from the Ag NW pastes through washing processes, decreasing the joining temperature of Ag NW pastes. The joints processed at room-temperature achieved a tensile strength of 5.7 MPa and exhibited ultralow resistivity in the range of 101 nΩ•m. The residual PVP was found to prevent the formation

of CuO and promote joining by 'in-situ cleaning' behavior at elevated temperatures. The failure of Ag NWs accounted for the fracture of joints. The modulus and nanohardness of Ag NW porous materials were 14 GPa and 0.51 GPa respectively, close to those of flexible substrates which are widely used in electronic industry. Such good mechanical compatibility would reduce the mechanical stresses at the interfaces between Ag NW porous materials and flexible substrates during deformation. The porous structure could relieve the thermo-mechanical stresses as well during practical applications.

(3) The local heating effects have been found for the first time in a Cu-Ag paste system and promoted the room-temperature joining process. The reaction energy of the Cu-Ag reaction, Cu oxidation and CuO deoxidation at nanoscale close to the interfaces elevated the local temperature of Ag NW to significantly above room temperature. The lumped heat capacity model has also confirmed that locally generated heating occurred during joining. The CuO-PVP reaction could consume the residual PVP in the water of paste thus further reducing the organic content in the paste. It also consumed the PVP protection layer on the surfaces of the Ag NWs to activate the side surfaces for joining. All these effects reduced the organic contents to provide cleaner interfaces of Ag NW-NW and Ag NW-Cu for joining. The local heating could break down the localized organic layer on the side surface of the Ag NWs as well and promote the interdiffusion of atoms. The Ag NWs formed three dimensional networks via end-to-end, end-to-side and side-to-side joints and metallurgically bonded with reactive assembly substrates, such as Cu at room temperature as a result of benefitting from local heating effects at the nanoscale. These metallic bonds contributed to good tensile shear strength and conductivity of interconnected Cu wires. The local heating effects discovered in this work induced nanojoining because of chemical reaction at a nano scale and reduction of surface areas. This process provides insight for design of reactive nano pastes for various joining/packaging systems.

(4) Ag NWs have been introduced into NP matrices to examine their mechanical behavior during loading. Joints with high strength and fracture energy were produced by low temperature thermal sintering of Ag NP/NW mixed pastes in a pressureless joining method. The addition of 20 vol.% Ag NW improved the strength of joints bonded at low temperature (60 to 150 ^{o}C) by 50% to 80%. When the NW volume fraction was increased to 30% the joining paste became highly porous and the mechanical properties severely degraded. Interfacial fracture dominated at the Cu/Ag interface at the Cu wire surface when Ag NWs were added into the paste. Cu and Ag were found to form a metallic bond during the low temperature pressureless joining process. The addition of Ag NWs decreased the

elastic modulus and nanohardness of NP-NW nanoporous composites leading to better mechanical compatibility with flexible substrates. The Ag NWs inside NP matrix provided crack deflection and fracture energy absorption during loading of the joints via mechanisms of Ag NW bending, deformation, breaking and pull-out.

6.2 Recommendations for Future Work

This dissertation reveals several key insights on the joining of Ag NWs and the processing-structure-mechanical property relationships in the silver porous materials, aiming to develop new methods for low temperature joining of nanomaterials and understand their properties. Although many insightful findings have been obtained, these works can be further extended along the following lines.

(1) V-shaped or *zig-zag* Ag NWs processed at room-temperature have similar crystal orientation in the joined region, suggesting a novel structure for investigating the one-dimensional transport properties in curved Ag NWs. Accordingly, the atomic level investigation of the joining process using molecular dynamics simulations will help to enhance the understanding of joining mechanisms. Meanwhile, the understanding of thermal, optical, and electrical transport properties in joined Ag NWs including end-to-end, end-to-side or side-to-side configurations through experimental or simulation works will be of much interest and significance.

(2) The nano size effect has been studied previously by others based on gold nanoporous materials fabricated by a dealloying technique, suggesting that the yield strength has a nonlinear correlation with ligament thickness. Silver nanoporous materials composed of NPs have a similar relation, however the scaling relations have not been established so far. Thus, the scaling law incorporating the size effect of NPs will hopefully be able to predict the strength of silver nanoporous materials. Nanoporous materials produced by low-temperature joining of Ag NWs are different from those composed of NPs. Since the long axis of Ag NWs is in the micron range which is also fairly small, the size scale including both thickness and length of Ag NWs would contribute to the strength enhancement. In this sense, investigation of the mechanical behavior of Ag NW porous materials by tuning the thickness and length could help to clarify the mechanical properties of one-dimensional nanostructures. Hopefully, the scaling relation could be established as well.

(3) Regarding room-temperature joining using Ag NW pastes, the size of Ag NWs could also affect the properties of joints. This size involves thickness and length of NWs. Therefore, the aspect

ratio (= length/ thickness) of NWs could be tuned to optimize the properties of joints. Since the porosity of joints is relative to the sizes of NWs in 3D structures, broader size distribution of NWs in the paste could help to gain higher density of joint if no external pressure is applied compared with that with uniform size distribution. Furthermore, the mechanical properties of individual Ag NWs have strong relationship with their sizes, suggesting that the as-expected scaling relation as mentioned above would be able to help to design the sizes of NWs to further optimize the mechanical properties of Ag NW joints.

(4) Various metal NWs have been characterized under tensile conditions but their compressive strengths have received little attention. Ag NWs can undergo a different stress concentration under bending condition because of their one-dimensional shape. Experimental bending tests could help in understanding the mechanical properties of single Ag NWs, such as yield strength and modulus. Simulation work with proper technique could also reveal the underlying deformation mechanisms.

(5) In practice, to push Ag NW pastes into industrial use, the stability and rheological properties of the pastes should be studied. Ag NWs can also be used for conductive adhesives and thin conductive films or electrodes. Two-dimensional Ag NW networks have been found to have excellent conductivity without losing the transparency of thin films. They will have a wide application in flexible electronics or solar cells. With the improved understanding of one-dimensional transport properties in Ag NWs as mentioned previously, the properties of such Ag NW networks can be optimized to meet the demands of practical applications.

(6) Whether the present sintering mechanisms, such as surface diffusion, evaporation-condensation, grain boundary diffusion and lattice diffusion, would be available at a nanoscale is still veiled. The available models for describing the sintering behaviors are based on spherical particles. Since other shaped nanomaterials such as nanowires and nanobelts are different from the spherical case, the models may not be suitable for them as well. Accordingly, study of nanoscopic sintering of different shaped nanomaterials will extend the knowledge to a nanoscale and offer some understanding of nanojoining processes and will stimulate new processing technologies and practical applications.

Reference

1. S. Seob áLee and S. Hwan áKo: *Nanoscale*, 2012, **4**, 6408-6414.
2. P. Peng, A. Hu and Y. Zhou: *Applied Physics a-Materials Science & Processing*, 2012, **108**, 685-691.
3. J. A. Spechler and C. B. Arnold: *Applied Physics A*, 2012, **108**, 25-28.
4. L. Dong, X. Tao, L. Zhang, X. Zhang and B. J. Nelson: *Nano Letters*, 2007, **7**, 58-63.
5. C. Chen, L. Yan, E. S.-W. Kong and Y. Zhang: *Nanotechnology*, 2006, **17**, 2192.
6. Y. Peng, T. Cullis and B. Inkson: *Nano Letters*, 2008, **9**, 91-96.
7. F. Gao and Z. Gu: *Nanotechnology*, 2010, **21**, 115604.
8. Q. Cui, F. Gao, S. Mukherjee and Z. Gu: *Small*, 2009, **5**, 1246-1257.
9. E. C. Garnett, W. S. Cai, J. J. Cha, F. Mahmood, S. T. Connor, M. G. Christoforo, Y. Cui, M. D. McGehee and M. L. Brongersma: *Nature Materials*, 2012, **11**, 241-249.
10. Z. Pereira and E. Da Silva: *The Journal of Physical Chemistry C*, 2011, **115**, 22870-22876.
11. Y. Lu, J. Y. Huang, C. Wang, S. H. Sun and J. Lou: *Nature Nanotechnology*, 2010, **5**, 218-224.
12. A. Hu, P. Peng, H. Alarifi, X. Zhang, J. Guo, Y. Zhou and W. Duley: *Journal of Laser Applications*, 2012, **24**, 042001.
13. Y. Zhou: *Microjoining and Nanojoining*. Woodhead, England, 2008.
14. P. R. Couchman and W. A. Jesser: *Nature*, 1977, **269**, 481-483.
15. K. Nanda, S. Sahu and S. Behera: *Physical Review A*, 2002, **66**, 013208.
16. H. Alarifi, A. M. Hu, M. Yavuz and Y. N. Zhou: *Journal of Electronic Materials*, 2011, **40**, 1394-1402.
17. G. Bai: *Low-temperature sintering of nanoscale silver paste for semiconductor device interconnection*, Virginia Polytechnic Institute and State University 2005.
18. J. F. Yan, G. S. Zou, A. M. Hu and Y. N. Zhou: *Journal of Materials Chemistry*, 2011, **21**, 15981-15986.
19. T. Bakhishev and V. Subramanian: *Journal of Electronic Materials*, 2009, **38**, 2720-2725.
20. J. Aizenberg, J. C. Weaver, M. S. Thanawala, V. C. Sundar, D. E. Morse and P. Fratzl: *Science*, 2005, **309**, 275-278.
21. N. Kröger: *Current opinion in chemical biology*, 2007, **11**, 662-669.
22. S. J. Hollister: *Nature Materials*, 2005, **4**, 518-524.
23. S. V. Madihally and H. W. Matthew: *Biomaterials*, 1999, **20**, 1133-1142.
24. K. Rezwan, Q. Chen, J. Blaker and A. R. Boccaccini: *Biomaterials*, 2006, **27**, 3413-3431.
25. D. W. Bruce, D. O'Hare and R. I. Walton: *Porous materials*. Wiley. com, 2011, **vol. 13**.
26. N. Kanellopoulos: *Nanoporous materials: advanced techniques for characterization, modeling, and processing*. Taylor & Francis US, 2011.
27. S. S.-Y. Chui, S. M.-F. Lo, J. P. Charmant, A. G. Orpen and I. D. Williams: *Science*, 1999, **283**, 1148-1150.
28. C. Xu, J. Su, X. Xu, P. Liu, H. Zhao, F. Tian and Y. Ding: *Journal of the American Chemical Society*, 2007, **129**, 42-43.
29. L. Qian, X. Yan, T. Fujita, A. Inoue and M. Chen: *Applied Physics Letters*, 2007, **90**, 153120-153120-153123.
30. M. Hakamada and M. Mabuchi: *Scripta Materialia*, 2007, **56**, 1003-1006.

31. J. Biener, A. M. Hodge, J. R. Hayes, C. A. Volkert, L. A. Zepeda-Ruiz, A. V. Hamza and F. F. Abraham: *Nano Letters*, 2006, **6**, 2379-2382.
32. L. J. Gibson and M. F. Ashby: *Cellular solids: structure and properties*. Cambridge university press, 1999.
33. A. Hodge, J. Biener, J. Hayes, P. Bythrow, C. Volkert and A. Hamza: *Acta Materialia*, 2007, **55**, 1343-1349.
34. K.-N. Tu and K. Zeng: *Materials Science and Engineering: R: Reports*, 2001, **34**, 1-58.
35. S. Wiese and K.-J. Wolter: *Microelectronics Reliability*, 2007, **47**, 223-232.
36. W. Dreyer and W. H. Müller: *International Journal of Solids and Structures*, 2001, **38**, 1433-1458.
37. M. Dudek and N. Chawla: *Acta Materialia*, 2009, **57**, 4588-4599.
38. R. Darveaux: *Journal of Electronic Packaging*, 2002, **124**, 147-154.
39. Y. Li and C. Wong: *Materials Science and Engineering: R: Reports*, 2006, **51**, 1-35.
40. T. Zhou, X. Wang, X. Liu and D. Xiong: *Carbon*, 2010, **48**, 1171-1176.
41. J. N. Coleman, U. Khan and Y. K. Gun'ko: *Adv Mater*, 2006, **18**, 689-706.
42. D. Webster: *Metallurgical Transactions A*, 1982, **13**, 1511-1519.
43. T. Nieh, C. Henshall and J. Wadsworth: *Scripta Metallurgica*, 1984, **18**, 1405-1408.
44. B. H. Hong, S. C. Bae, C.-W. Lee, S. Jeong and K. S. Kim: *Science*, 2001, **294**, 348-351.
45. J. K. Mbindyo, T. E. Mallouk, J. B. Mattzela, I. Kratochvilova, B. Razavi, T. N. Jackson and T. S. Mayer: *Journal of the American Chemical Society*, 2002, **124**, 4020-4026.
46. X. He, X. Zhao, Y. Li and X. Sui: *J. Mater. Res*, 2009, **24**, 2201.
47. D. M. Ledwith, A. M. Whelan and J. M. Kelly: *Journal of Materials Chemistry*, 2007, **17**, 2459-2464.
48. J. Chen, B. J. Wiley and Y. Xia: *Langmuir*, 2007, **23**, 4120-4129.
49. M. Maillard, S. Giorgio and M.-P. Pileni: *Adv Mater*, 2002, **14**, 1084.
50. S. H. Im, Y. T. Lee, B. Wiley and Y. Xia: *Angew Chem*, 2005, **117**, 2192-2195.
51. M. A. El-Sayed: *Acc Chem Res*, 2001, **34**, 257-264.
52. C. J. Murphy: *Science*, 2002, **298**, 2139-2141.
53. W. Wang, S. Efrima and O. Regev: *Langmuir*, 1998, **14**, 602-610.
54. Y. Badr, M. Wahed and M. Mahmoud: *Applied Surface Science*, 2006, **253**, 2502-2507.
55. X. Sun and Y. Luo: *Materials Letters*, 2005, **59**, 3847-3850.
56. Y. Tan, Y. Li and D. Zhu: *J Colloid Interface Sci*, 2003, **258**, 244-251.
57. H. Lu, H. Zhang, X. Yu, S. Zeng, K.-T. Yong and H.-P. Ho: *Plasmonics*, 2012, **7**, 167-173.
58. M. S. Gudiksen, L. J. Lauhon, J. Wang, D. C. Smith and C. M. Lieber: *Nature*, 2002, **415**, 617-620.
59. L. Sun, P. Searson and C. Chien: *Applied Physics Letters*, 2001, **79**, 4429-4431.
60. A. Govindaraj, B. Satishkumar, M. Nath and C. Rao: *Chemistry of Materials*, 2000, **12**, 202-205.
61. R.-L. Zong, J. Zhou, Q. Li, B. Du, B. Li, M. Fu, X.-W. Qi, L.-T. Li and S. Buddhudu: *The Journal of Physical Chemistry B*, 2004, **108**, 16713-16716.
62. D. Zhang, L. Qi, J. Ma and H. Cheng: *Adv Mater*, 2002, **14**, 1499-1502.
63. K. Caswell, C. M. Bender and C. J. Murphy: *Nano Letters*, 2003, **3**, 667-669.
64. Z. Wang, J. Liu, X. Chen, J. Wan and Y. Qian: *Chemistry-A European Journal*, 2005, **11**, 160-163.

65. L. Gou, M. Chipara and J. M. Zaleski: *Chemistry of Materials*, 2007, **19**, 1755-1760.
66. Y. Sun, B. Mayers, T. Herricks and Y. Xia: *Nano Letters*, 2003, **3**, 955-960.
67. Y. Sun, Y. Yin, B. T. Mayers, T. Herricks and Y. Xia: *Chemistry of Materials*, 2002, **14**, 4736-4745.
68. L. Marks: *Reports on Progress in Physics*, 1994, **57**, 603.
69. H. Huang, X. Ni, G. Loy, C. Chew, K. Tan, F. Loh, J. Deng and G. Xu: *Langmuir*, 1996, **12**, 909-912.
70. Y. Gao, L. Song, P. Jiang, L. Liu, X. Yan, Z. Zhou, D. Liu, J. Wang, H. Yuan and Z. Zhang: *Journal of Crystal Growth*, 2005, **276**, 606-612.
71. P. Buffat and J. P. Borel: *Physical Review A*, 1976, **13**, 2287.
72. S. S. Brenner: *Journal of applied physics*, 1956, **27**, 1484-1491.
73. E. Arzt: *Acta Materialia*, 1998, **46**, 5611-5626.
74. N. Fleck, G. Muller, M. Ashby and J. Hutchinson: *Acta Metall Mater*, 1994, **42**, 475-487.
75. J. R. Greer, W. C. Oliver and W. D. Nix: *Acta Materialia*, 2005, **53**, 1821-1830.
76. J. R. Greer and J. T. M. De Hosson: *Progress in Materials Science*, 2011, **56**, 654-724.
77. W. D. Nix and H. Gao: *Journal of the Mechanics and Physics of Solids*, 1998, **46**, 411-425.
78. K. Kinoshita: *Journal of the Electrochemical Society*, 1990, **137**, 845-848.
79. M. Valden, X. Lai and D. W. Goodman: *Science*, 1998, **281**, 1647-1650.
80. M. Smithard: *Solid State Communications*, 1973, **13**, 153-156.
81. Y. He, Y. Miao, C. Li, S. Wang, L. Cao, S. Xie, G. Yang, B. Zou and C. Burda: *Physical Review B*, 2005, **71**, 125411.
82. F. Vollertsen: *Production Engineering*, 2008, **2**, 377-383.
83. T. Zhu and J. Li: *Progress in Materials Science*, 2010, **55**, 710-757.
84. E. Hall: *Proceedings of the Physical Society. Section B*, 1951, **64**, 747.
85. N. Petch: *J. Iron Steel Inst.*, 1953, **174**, 25-28.
86. A. Chokshi, A. Rosen, J. Karch and H. Gleiter: *Scripta Metallurgica*, 1989, **23**, 1679-1683.
87. T. Nieh and J. Wadsworth: *Scr Metall Mater*, 1991, **25**, 955-958.
88. N. Hansen: *Scripta Materialia*, 2004, **51**, 801-806.
89. C. Carlton and P. Ferreira: *Acta Materialia*, 2007, **55**, 3749-3756.
90. J. Schiøtz, F. D. Di Tolla and K. W. Jacobsen: *Nature*, 1998, **391**, 561-563.
91. J. Schiøtz, T. Vegge, F. Di Tolla and K. W. Jacobsen: *Physical Review B*, 1999, **60**, 11971.
92. J. Schiøtz and K. W. Jacobsen: *Science*, 2003, **301**, 1357-1359.
93. H. Bei, Y. Gao, S. Shim, E. P. George and G. M. Pharr: *Physical Review B*, 2008, **77**, 060103.
94. D. Dimiduk, M. Uchic and T. Parthasarathy: *Acta Materialia*, 2005, **53**, 4065-4077.
95. T. Zhu, J. Li, A. Samanta, A. Leach and K. Gall: *Physical Review Letters*, 2008, **100**, 025502.
96. T. Zhu, J. Li, S. Ogata and S. Yip: *Mrs Bulletin*, 2009, **34**, 167.
97. X. Chen and A. Ngan: *Scripta Materialia*, 2011, **64**, 717-720.
98. Y. Huang, F. Zhang, K. Hwang, W. Nix, G. Pharr and G. Feng: *Journal of the Mechanics and Physics of Solids*, 2006, **54**, 1668-1686.
99. T. Filleter, S. Ryu, K. Kang, J. Yin, R. A. Bernal, K. Sohn, S. Li, J. Huang, W. Cai and H. D. Espinosa: *Small*, 2012, **8**, 2986-2993.

100. Y. Zhu, Q. Qin, F. Xu, F. Fan, Y. Ding, T. Zhang, B. J. Wiley and Z. L. Wang: *Physical Review B*, 2012, **85**, 045443.
101. M. T. McDowell, A. M. Leach and K. Gall: *Nano Letters*, 2008, **8**, 3613-3618.
102. A. M. Leach, M. McDowell and K. Gall: *Advanced Functional Materials*, 2007, **17**, 43-53.
103. B. Wu, A. Heidelberg, J. J. Boland, J. E. Sader, X. Sun and Y. Li: *Nano Letters,* 2006, **6**, 468-472.
104. S. Cuenot, C. Frétigny, S. Demoustier-Champagne and B. Nysten: *Physical Review B,* 2004, **69**, 165410.
105. Y. Chen, B. L. Dorgan, D. N. McIlroy and D. Eric Aston: *Journal of applied physics*, 2006, **100**, 104301-104301-104307.
106. G. Jing, H. Duan, X. Sun, Z. Zhang, J. Xu, Y. Li, J. Wang and D. Yu: *Physical Review B,* 2006, **73**, 235409.
107. B. Wu, A. Heidelberg and J. J. Boland: *Nature Materials*, 2005, **4**, 525-529.
108. A. Heidelberg, L. T. Ngo, B. Wu, M. A. Phillips, S. Sharma, T. I. Kamins, J. E. Sader and J. J. Boland: *Nano Letters*, 2006, **6**, 1101-1106.
109. A. C. Fischer-Cripps: *Nanoindentation*. Springer, 2011, **vol. 1**.
110. W. C. Oliver and G. M. Pharr: *Journal of materials research*, 1992, **7**, 1564-1583.
111. X. Li, H. Gao, C. J. Murphy and K. Caswell: *Nano Letters*, 2003, **3**, 1495-1498.
112. G. Pharr: *Materials Science and Engineering: A*, 1998, **253**, 151-159.
113. B. Bhushan and X. Li: *International Materials Reviews*, 2003, **48**, 125-164.
114. C. Carlton and P. Ferreira: *Micron,* 2012, **43**, 1134-1139.
115. J. R. Greer and R. A. Street: *Journal of applied physics*, 2007, **101**, 103529-103529-103525.
116. A. Korsunsky, M. McGurk, S. Bull and T. Page: *Surf Coat Technol*, 1998, **99**, 171-183.
117. A. Panin, A. Shugurov and K. Oskomov: *Physics of the Solid State,* 2005, **47**, 2055-2059.
118. R. Dou, B. Xu and B. Derby: *Scripta Materialia*, 2010, **63**, 308-311.
119. L. J. Gibson and M. Ashby: *Proceedings of the Royal Society of London. A. Mathematical and Physical Sciences*, 1982, **382**, 43-59.
120. S. Buzzi, M. Dietiker, K. Kunze, R. Spolenak and J. Löffler: *Philosophical Magazine*, 2009, **89**, 869-884.
121. D. Christopher, R. Smith and A. Richter: *Nanotechnology*, 2001, **12**, 372.
122. Y. Zhou and A. Hu: *The Open Surface Science Journal*, 2011, **3**, 32-41.
123. J. Goldak, A. Chakravarti and M. Bibby: *Metallurgical transactions B,* 1984, **15**, 299-305.
124. T. Nishimura, M. Mitomo, H. Hirotsuru and M. Kawahara: *Journal of materials science letters,* 1995, **14**, 1046-1047.
125. J. Perelaer, B. J. de Gans and U. S. Schubert: *Adv Mater,* 2006, **18**, 2101-2104.
126. T. Imholt, C. Dyke, B. Hasslacher, J. Perez, D. Price, J. Roberts, J. Scott, A. Wadhawan, Z. Ye and J. Tour: *Chemistry of Materials*, 2003, **15**, 3969-3970.
127. E. Siores and D. Do Rego: *Journal of materials processing technology*, 1995, **48**, 619-625.
128. M. L. Pantoya and J. J. Granier: *Propellants, Explosives, Pyrotechnics*, 2005, **30**, 53-62.
129. Y. Zhou, W. Gale and T. North: *International Materials Reviews*, 1995, **40**, 181-196.
130. Y. Li, K. S. Moon and C. P. Wong: *Science*, 2005, **308**, 1419-1420.
131. K. Tu, A. Gusak and M. Li: *Journal of applied physics*, 2003, **93**, 1335-1353.
132. D. Frear and P. Vianco: *Metallurgical and Materials Transactions A*, 1994, **25**, 1509-1523.

133. J. Coughlin, J. Williams, G. Crawford and N. Chawla: *Metallurgical and Materials Transactions A*, 2009, **40**, 176-184.
134. Q. Z. Cui, F. Gao, S. Mukherjee and Z. Y. Gu: *Small*, 2009, **5**, 1246-1257.
135. X. Y. Zeng, Q. K. Zhang, R. M. Yu and C. Z. Lu: *Adv Mater*, 2010, **22**, 4484-4488.
136. K. T. Ko, M. H. Jung, Q. He, J. H. Lee, C. S. Woo, K. Chu, J. Seidel, B. G. Jeon, Y. S. Oh, K. H. Kim, W. I. Liang, H. J. Chen, Y. H. Chu, Y. H. Jeong, R. Ramesh, J. H. Park and C. H. Yang: *Nature Communications*, 2011, **2**.
137. P. Ravindran, A. Delin, B. Johansson, O. Eriksson and J. Wills: *Physical Review B*, 1999, **59**, 1776.
138. S. Horiuchi and Y. Tokura: *Nature Materials*, 2008, **7**, 357-366.
139. A. Gerlich, P. Su, M. Yamamoto and T. North: *Science and Technology of Welding & Joining*, 2008, **13**, 254-264.
140. H. Bhadeshia and T. DebRoy: *Science and Technology of Welding & Joining*, 2009, **14**, 193-196.
141. G. G. Harman: *Wire bonding in microelectronics: materials, processes, reliability, and yield*. McGraw-Hill New York, 1997, **vol. 21**.
142. J. F. Lancaster: *Metallurgy of welding*. Abington Pub., 1999.
143. L. Vitos, A. Ruban, H. L. Skriver and J. Kollar: *Surface Science*, 1998, **411**, 186-202.
144. G. Ouyang, X. Tan and G. Yang: *Physical Review B*, 2006, **74**, 195408.
145. Y. Zhu, J. Lian and Q. Jiang: *The Journal of Physical Chemistry C*, 2009, **113**, 16896-16900.
146. A. Chernyshev: *Materials Letters*, 2009, **63**, 1525-1527.
147. W. Qi and M. Wang: *Materials chemistry and physics*, 2004, **88**, 280-284.
148. H. A. Alarifi, M. Atiş, C. Ozdogan, A. Hu, M. Yavuz and Y. N. Zhou: *The Journal of Physical Chemistry C*, 2013, **117**, 12289-12298.
149. M. Kuzenkova, P. Kislyi, B. Grabchuk and N. Bodnaruk: *Journal of the Less Common Metals*, 1979, **67**, 217-223.
150. K. Lu: *International Materials Reviews*, 2008, **53**, 21-38.
151. M. Mayo, D. Hague and D.-J. Chen: *Materials Science and Engineering: A*, 1993, **166**, 145-159.
152. S. H. Risbud, A. Mukherjee, M. Kim, J. Bow and R. Holl: *Journal of materials research*, 1995, **10**, 237-239.
153. Z. Fang and H. Wang: *International Materials Reviews*, 2008, **53**, 326-352.
154. J. Guo, C. Xu, A. Hu, K. Oakes, F. Sheng, Z. Shi, J. Dai and Z. Jin: *Journal of Physics and Chemistry of Solids*, 2012, **73**, 1350-1357.
155. J. Guo, C. Xu, A. Hu, Z. Shi, F. Sheng, J. Dai and Z. Li: *Journal of Nanoparticle Research*, 2012, **14**, 1-12.
156. E. Marzbanrad, A. Hu, B. Zhao and Y. Zhou: *The Journal of Physical Chemistry C*, 2013, **117**, 16665-16676.
157. L. Ding, R. L. Davidchack and J. Pan: *Computational Materials Science*, 2009, **45**, 247-256.
158. A. W. Searcy: *Journal of the American Ceramic Society*, 1985, **68**, C - 267-C - 268.
159. F. Wakai and Y. Shinoda: *Acta Materialia*, 2009, **57**, 3955-3964.
160. R. M. German: *Sintering Theory and Practice, by Randall M. German, pp. 568. ISBN 0-471-05786-X. Wiley-VCH, January 1996.*, 1996, **1**.

161. R. Coble: *Journal of applied physics*, 1961, **32**, 787.
162. H. Ch'ng and J. Pan: *Acta Materialia*, 2007, **55**, 813-824.
163. H. Schwarzbauer and R. Kuhnert: in *Industry Applications Society Annual Meeting, 1989., Conference Record of the 1989 IEEE*. IEEE, 1989, 1348-1351.
164. Y. Morisada, T. Nagaoka, M. Fukusumi, Y. Kashiwagi, M. Yamamoto and M. Nakamoto: *Journal of Electronic Materials*, 2010, **39**, 1283-1288.
165. J. Provance and K. Allison: "Particle size effects on viscosity of silver pastes: a manufacturer's view" Ferro Corp., Santa Barbara, CA (USA), 1983.
166. S. Rane, T. Seth, G. Phatak, D. Amalnerkar and B. Das: *Materials Letters*, 2003, **57**, 3096-3100.
167. J. Lin and C. Wang: *Materials chemistry and physics*, 1996, **45**, 136-144.
168. M. Jørgensen, O. Hagemann, J. Alstrup and F. C. Krebs: *Solar Energy Materials and Solar Cells*, 2009, **93**, 413-421.
169. K. S. Siow: *Journal of Alloys and Compounds*, 2012, **514**, 6-19.
170. W. Luo, W. Hu and S. Xiao: *The Journal of Physical Chemistry C*, 2008, **112**, 2359-2369.
171. H. Alarifi, M. Atis, C. Özdoğan, A. Hu, M. Yavuz and Y. Zhou: *Materials Transactions*, 2013, **54**, 884-889.
172. A. Hu, J. Guo, H. Alarifi, G. Patane, Y. Zhou, G. Compagnini and C. Xu: *Applied Physics Letters*, 2010, **97**, 153117-153117-153113.
173. E. Ide, S. Angata, A. Hirose and K. F. Kobayashi: *Acta Materialia*, 2005, **53**, 2385-2393.
174. A. Hirose, H. Tatsumi, N. Takeda, Y. Akada, T. Ogura, E. Ide and T. Morita: in *Journal of Physics: Conference Series*. IOP Publishing, 2009, vol. 165, 012074.
175. J. Yan, G. Zou, A.-p. Wu, J. Ren, J. Yan, A. Hu and Y. Zhou: *Scripta Materialia*, 2012, **66**, 582-585.
176. T. Morita, Y. Yasuda, E. Ide, Y. Akada and A. Hirose: *Materials Transactions*, 2008, **49**, 2875.
177. G. Zou, J. Yan, F. Mu, A. Wu, J. Ren, A. Hu and Y. Zhou: *Open Surface Science Journal*, 2011, **3**, 70-75.
178. T. Wang, X. Chen, G.-Q. Lu and G.-Y. Lei: *Journal of Electronic Materials*, 2007, **36**, 1333-1340.
179. S. Egelkraut, L. Frey, M. Knoerr and A. Schletz: in *Electronics Packaging Technology Conference (EPTC), 2010 12th*. IEEE, 2010, 660-667.
180. T. G. Lei, J. N. Calata, G.-Q. Lu, X. Chen and S. Luo: *Components and Packaging Technologies, IEEE Transactions on*, 2010, **33**, 98-104.
181. M. Knoerr and A. Schletz: in *Integrated Power Electronics Systems (CIPS), 2010 6th International Conference on*. IEEE, 2010, 1-6.
182. P. Peng, A. M. Hu, B. X. Zhao, A. P. Gerlich and Y. N. Zhou: *Journal of Materials Science*, 2012, **47**, 6801-6811.
183. T. Morita, E. Ide, Y. Yasuda, A. Hirose and K. Kobayashi: *Japanese Journal of Applied Physics*, 2008, **47**, 6615.
184. P. Peng, A. M. Hu, H. Huang, A. P. Gerlich, B. X. Zhao and Y. N. Zhou: *Journal of Materials Chemistry*, 2012, **22**, 12997-13001.
185. Y. Morisada, T. Nagaoka, M. Fukusumi, Y. Kashiwagi, M. Yamamoto, M. Nakamoto, H. Kakiuchi and Y. Yoshida: *Journal of Electronic Materials*, 2011, **40**, 2398-2402.
186. S. Magdassi, M. Grouchko, O. Berezin and A. Kamyshny: *ACS Nano*, 2010, **4**, 1943-1948.

187. M. Layani, M. Grouchko, S. Shemesh and S. Magdassi: *Journal of Materials Chemistry*, 2012, **22**, 14349-14352.
188. M. Layani and S. Magdassi: *Journal of Materials Chemistry*, 2011, **21**, 15378-15382.
189. Y. Tang, W. He, G. Zhou, S. Wang, X. Yang, Z. Tao and J. Zhou: *Nanotechnology*, 2012, **23**, 355304.
190. F. Gao, S. Mukherjee, Q. Cui and Z. Gu: *The Journal of Physical Chemistry C*, 2009, **113**, 9546-9552.
191. Z. Gu, H. Ye, D. Smirnova, D. Small and D. H. Gracias: *Small*, 2006, **2**, 225-229.
192. H. Tohmyoh: *Journal of applied physics*, 2009, **105**, 014907-014907-014909.
193. H.-S. Kim, S. R. Dhage, D.-E. Shim and H. T. Hahn: *Applied Physics A*, 2009, **97**, 791-798.
194. M. Hösel and F. C. Krebs: *Journal of Materials Chemistry*, 2012, **22**, 15683-15688.
195. L. Liu, P. Peng, A. Hu, G. Zou, W. Duley and Y. N. Zhou: *Applied Physics Letters*, 2013, **102**, 073107-073107-073104.
196. J. E. Krzanowski: in *Electronic Components Conference, 1989. Proceedings., 39th*. IEEE, 1989, 450-455.
197. L. Li, K. Nagai and F. Yin: *Science and Technology of Advanced Materials*, 2008, **9**, 023001.
198. Q. Ma, Z. Wang and Y. Zhong: *Journal of materials processing technology*, 2002, **123**, 61-66.
199. I. Shigematsu, Y.-J. Kwon, K. Suzuki, T. Imai and N. Saito: *Journal of materials science letters*, 2003, **22**, 353-356.
200. R. Nandan, T. DebRoy and H. Bhadeshia: *Progress in Materials Science*, 2008, **53**, 980-1023.
201. T. Tokuno, M. Nogi, M. Karakawa, J. Jiu, T. T. Nge, Y. Aso and K. Suganuma: *Nano Research*, 2011, **4**, 1215-1222.
202. H. Hirayama, Y. Kawamoto, Y. Ohshima and K. Takayanagi: *Applied Physics Letters*, 2001, **79**, 1169-1171.
203. C. Jin, K. Suenaga and S. Iijima: *Nature Nanotechnology*, 2007, **3**, 17-21.
204. Y. Wu and P. Yang: *Adv Mater*, 2001, **13**, 520-523.
205. M. A. van Huis, L. T. Kunneman, K. Overgaag, Q. Xu, G. Pandraud, H. W. Zandbergen and D. Vanmaekelbergh: *Nano Letters*, 2008, **8**, 3959-3963.
206. V. Gopal, V. R. Radmilovic, C. Daraio, S. Jin, P. Yang and E. A. Stach: *Nano Letters*, 2004, **4**, 2059-2063.
207. M. Wang, J. Wang, Q. Chen and L. M. Peng: *Advanced Functional Materials*, 2005, **15**, 1825-1831.
208. S. Xu, M. Tian, J. Wang, J. Xu, J. M. Redwing and M. H. Chan: *Small*, 2005, **1**, 1221-1229.
209. S. J. Kim and D.-J. Jang: *Applied Physics Letters*, 2005, **86**, 033112-033112-033113.
210. F. Mafuné, J.-y. Kohno, Y. Takeda and T. Kondow: *Journal of the American Chemical Society*, 2003, **125**, 1686-1687.
211. X. Liu, J. Luo and J. Zhu: *Nano Letters*, 2006, **6**, 408-412.
212. D. Chen and L. Gao: *Journal of Crystal Growth*, 2004, **264**, 216-222.
213. X. Jiang, S. Xiong, C. Chen, W. Chen and A. Yu: *Journal of Nanoparticle Research*, 2011, **13**, 5087-5101.
214. C. Lofton and W. Sigmund: *Advanced Functional Materials*, 2005, **15**, 1197-1208.
215. B. Wiley, Y. Sun, B. Mayers and Y. Xia: *Chemistry-A European Journal*, 2005, **11**, 454-463.
216. X. Yuan, C. Li, G. Guan, Y. Xiao and D. Zhang: *Polym Degrad Stab*, 2008, **93**, 466-475.

217. M. Zheng, M. Gu, Y. Jin and G. Jin: *Materials Science and Engineering: B*, 2000, **77**, 55-59.
218. B. Gao, G. Arya and A. R. Tao: *Nature Nanotechnology*, 2012, **7**, 433-437.
219. H. Christenson: *The Journal of Physical Chemistry*, 1993, **97**, 12034-12041.
220. A. Kuznetsova, D. B. Mawhinney, V. Naumenko, J. T. Yates Jr, J. Liu and R. Smalley: *Chemical Physics Letters*, 2000, **321**, 292-296.
221. C. Campbell, G. Ertl, H. Kuipers and J. Segner: *Surface Science*, 1981, **107**, 220-236.
222. W. Ludwig, A. Savara, R. J. Madix, S. Schauermann and H.-J. Freund: *The Journal of Physical Chemistry C*, 2012, **116**, 3539-3544.
223. J.-M. Savéant: *Journal of electroanalytical chemistry and interfacial electrochemistry*, 1991, **302**, 91-101.
224. J. Reyes-Gasga, J. Elechiguerra, C. Liu, A. Camacho-Bragado, J. Montejano-Carrizales and M. Jose Yacaman: *Journal of Crystal Growth*, 2006, **286**, 162-172.
225. U. Dahmen, C. Hetherington, V. Radmilovic, E. Johnson, S. Xiao and C. Luo: *Microsc Microanal*, 2002, **8**, 247-256.
226. J. L. Elechiguerra, J. Reyes-Gasga and M. J. Yacaman: *Journal of Materials Chemistry*, 2006, **16**, 3906-3919.
227. J. Wu, S. Nagao, J. He and Z. Zhang: *Nano Letters*, 2011, **11**, 5264-5273.
228. J.-H. Seo, Y. Yoo, N.-Y. Park, S.-W. Yoon, H. Lee, S. Han, S.-W. Lee, T.-Y. Seong, S.-C. Lee and K.-B. Lee: *Nano Letters*, 2011, **11**, 3499-3502.
229. J. H. Ahn, H. S. Kim, K. J. Lee, S. Jeon, S. J. Kang, Y. G. Sun, R. G. Nuzzo and J. A. Rogers: *Science*, 2006, **314**, 1754-1757.
230. T. Sekitani, U. Zschieschang, H. Klauk and T. Someya: *Nature Materials*, 2010, **9**, 1015-1022.
231. D. M. Sun, M. Y. Timmermans, Y. Tian, A. G. Nasibulin, E. I. Kauppinen, S. Kishimoto, T. Mizutani and Y. Ohno: *Nature Nanotechnology*, 2011, **6**, 156-161.
232. B. Yoon, D. Y. Ham, O. Yarimaga, H. An, C. W. Lee and J. M. Kim: *Adv Mater*, 2011, **23**, 5492-+.
233. T. Someya, Y. Kato, T. Sekitani, S. Iba, Y. Noguchi, Y. Murase, H. Kawaguchi and T. Sakurai: *Proceedings of the National Academy of Sciences of the United States of America*, 2005, **102**, 12321-12325.
234. T. S. van der Poll, J. A. Love, T. Q. Nguyen and G. C. Bazan: *Adv Mater*, 2012, **24**, 3646-3649.
235. W. B. Yang, H. S. Duan, B. Bob, H. P. Zhou, B. Lei, C. H. Chung, S. H. Li, W. W. Hou and Y. Yang: *Adv Mater*, 2012, **24**, 6323-6329.
236. A. Perumal, M. Frobel, S. Gorantla, T. Gemming, B. Lussem, J. Eckert and K. Leo: *Advanced Functional Materials*, 2012, **22**, 210-217.
237. Q. Wang, Y. T. Tao, X. F. Qiao, J. S. Chen, D. G. Ma, C. L. Yang and J. G. Qin: *Advanced Functional Materials*, 2011, **21**, 1681-1686.
238. Y. Jin, J. Feng, X. L. Zhang, Y. G. Bi, Y. Bai, L. Chen, T. Lan, Y. F. Liu, Q. D. Chen and H. B. Sun: *Adv Mater*, 2012, **24**, 1187-1191.
239. J. Chung, S. Ko, N. R. Bieri, C. P. Grigoropoulos and D. Poulikakos: *Applied Physics Letters*, 2004, **84**, 801.
240. Y. T. Cheng, R. H. Uang, Y. M. Wang, K. C. Chiou and T. M. Lee: *Microelectronic Engineering*, 2009, **86**, 865-867.

241. M. L. Allen, M. Aronniemi, T. Mattila, A. Alastalo, K. Ojanperä, M. Suhonen and H. Seppä: *Nanotechnology*, 2008, **19**, 175201.
242. A. P. Gerlich and T. Shibayanagi: *Science and Technology of Welding and Joining*, 2011, **16**, 295-299.
243. A. Shah, M. Mayer, I. Qin, C. Huynh, Y. Zhou and M. Meyer: *Journal of Physics D-Applied Physics*, 2010, **43**.
244. J. Perelaer, B. J. de Gans and U. S. Schubert: *Adv Mater*, 2006, **18**, 2101-2104.
245. C. Kim, P. E. Burrows and S. R. Forrest: *Science*, 2000, **288**, 831-833.
246. C. Kim and S. R. Forrest: *Adv Mater*, 2003, **15**, 541-545.
247. J. P. Coughlin, J. J. Williams, G. A. Crawford and N. Chawla: *Metallurgical and Materials Transactions a-Physical Metallurgy and Materials Science*, 2009, **40A**, 176-184.
248. L. B. Hu, M. Pasta, F. La Mantia, L. F. Cui, S. Jeong, H. D. Deshazer, J. W. Choi, S. M. Han and Y. Cui: *Nano Letters*, 2010, **10**, 708-714.
249. S. Horiuchi, F. Ishii, R. Kumai, Y. Okimoto, H. Tachibana, N. Nagaosa and Y. Tokura: *Nature Materials*, 2008, **7**, 922-922.
250. Y. Peng, T. Cullis and B. Inkson: *Nano Letters*, 2009, **9**, 91-96.
251. P. Peng, L. Liu, A. P. Gerlich, A. Hu and Y. N. Zhou: *Particle & Particle Systems Characterization*, 2013, **30**, 420-426.
252. J. G. Bai, J. N. Calata, G. Y. Lei and G. Q. Lu: *2006 Proceedings 10th Intersociety Conference on Thermal and Thermomechanical Phenomena in Electronics Systems, Vols 1 and 2*, 2006, 1126-1130.
253. Z. Li, R. Zhang, K. S. Moon, Y. Liu, K. Hansen, T. Le and C. Wong: *Advanced Functional Materials*, 2012.
254. C. Yang, W. Lin, Z. Y. Li, R. W. Zhang, H. R. Wen, B. Gao, G. H. Chen, P. Gao, M. M. F. Yuen and C. P. Wong: *Advanced Functional Materials*, 2011, **21**, 4582-4588.
255. K.-S. Moon, H. Dong, R. Maric, S. Pothukuchi, A. Hunt, Y. Li and C. Wong: *Journal of Electronic Materials*, 2005, **34**, 168-175.
256. R. Zhang, K.-s. Moon, W. Lin and C. Wong: *Journal of Materials Chemistry*, 2010, **20**, 2018-2023.
257. B. Zhao and H. J. Kwon: *J Adhes Sci Technol*, 2011, **25**, 557-579.
258. C.-H. Hsueh: *Materials Science and Engineering: A*, 1990, **123**, 1-11.
259. S. Mall, R. P. Vozzola and L. P. Zawada: *Journal of the American Ceramic Society*, 1989, **72**, 1175-1178.
260. W. C. Oliver and G. M. Pharr: *Journal of materials research*, 2004, **19**, 3-20.
261. X. Li and B. Bhushan: *Materials characterization*, 2002, **48**, 11-36.
262. L. Bonacina, A. Callegari, C. Bonati, F. van Mourik and M. Chergui: *Nano Letters*, 2006, **6**, 7-10.
263. G. Perrin: *Journal of Physics and Chemistry of Solids*, 2001, **62**, 2091-2094.
264. R. Li and J. Jiao: in *PROCEEDINGS-SPIE THE INTERNATIONAL SOCIETY FOR OPTICAL ENGINEERING*. International Society for Optical Engineering; 1999, 2000, 068-073.
265. D. Bhattacharyya, P. Maitrot and S. Fakirov: *Express Polym Lett*, 2009, **3**, 525-532.
266. E. Lee, Y. Lee, W. Oliver and L. Mansur: *Journal of materials research*, 1993, **8**, 377-387.

267. R. Bartali, V. Micheli, G. Gottardi, A. Vaccari and N. Laidani: *Surf Coat Technol,* 2010, **204**, 2073-2076.
268. H. Jiang, K.-s. Moon, Y. Li and C. Wong: *Chemistry of Materials*, 2006, **18**, 2969-2973.
269. W. Steinhogl, G. Schindler, G. Steinlesberger, M. Traving and M. Engelhardt: *Journal of applied physics*, 2005, **97**, 023706-023706-023707.
270. K. Raith, A. V. Kühn, F. Rosche, R. Wolf and R. H. Neubert: *Pharm Res*, 2002, **19**, 556-560.
271. Y. Xiong, I. Washio, J. Chen, H. Cai, Z.-Y. Li and Y. Xia: *Langmuir*, 2006, **22**, 8563-8570.
272. C. E. Hoppe, M. Lazzari, I. Pardiñas-Blanco and M. A. López-Quintela: *Langmuir*, 2006, **22**, 7027-7034.
273. Y. J. Zhan, Y. Lu, C. Peng and J. Lou: *Journal of Crystal Growth*, 2011, **325**, 76-80.
274. H. Wang, X. Qiao, J. Chen, X. Wang and S. Ding: *Materials chemistry and physics*, 2005, **94**, 449-453.
275. J. H. Lienhard: *A heat transfer textbook*. Courier Dover Publications, 2011.
276. http://www.engineeringtoolbox.com/overall-heat-transfer-coefficient-d_434.html.
277. P. Peng, H. Huang, A. M. Hu, A. P. Gerlich and Y. N. Zhou: *Journal of Materials Chemistry,* 2012, **22**, 15495-15499.
278. Y. J. Xiong, I. Washio, J. Y. Chen, H. G. Cai, Z. Y. Li and Y. N. Xia: *Langmuir*, 2006, **22**, 8563-8570.
279. J.-M. Zhang, F. Ma and K.-W. Xu: *Applied Surface Science*, 2004, **229**, 34-42.
280. I. Barin, F. Sauert, E. Schultze-Rhonhof and W. S. Sheng: *Thermochemical data of pure substances*. VCH Weinheim, Germany, 1993, **vol. 6940**.
281. http://www.roymech.co.uk/Related/Thermos/Thermos_HeatTransfer.html.
282. K. Kwak and C. Kim: *Korea-Australia Rheology Journal*, 2005, **17**, 35-40.
283. http://www2.ucdsb.on.ca/tiss/stretton/database/Specific_Heat_Capacity_Table.html.
284. H. N. Ngoc, A. M. Hu, J. Persic and J. Z. Wen: *Chemical Physics Letters*, 2011, **503**, 112-117.
285. E. Owen and G. Williams: *Journal of Scientific Instruments*, 1954, **31**, 49.
286. X. Jiang, S. Xiong, Z. Tian, C. Chen, W. Chen and A. Yu: *The Journal of Physical Chemistry C,* 2011, **115**, 1800-1810.
287. Y. G. Sun, B. Mayers, T. Herricks and Y. N. Xia: *Nano Letters,* 2003, **3**, 955-960.
288. K. Zeng and K. Tu: *Materials Science and Engineering: R: Reports,* 2002, **38**, 55-105.
289. H. Sirringhaus, T. Kawase, R. Friend, T. Shimoda, M. Inbasekaran, W. Wu and E. Woo: *Science*, 2000, **290**, 2123.
290. B. A. Ridley, B. Nivi and J. M. Jacobson: *Science*, 1999, **286**, 746.
291. W.-F. Lee and K.-T. Tsao: *Journal of Materials Science*, 2010, **45**, 89-97.
292. K. Yung, S. Wu and H. Liem: *Journal of Materials Science*, 2009, **44**, 154-159.
293. D. Kim and J. Moon: *Electrochemical and Solid-State Letters*, 2005, **8**, J30.
294. H. H. Lee, K. S. Chou and K. C. Huang: *Nanotechnology,* 2005, **16**, 2436.
295. C. James, T. Chakraborty, A. Brown, T. Comyn, R. Dorey, J. Harrington, A. Laister, R. Miles, C. Puchmark and B. Xu: *Journal of Materials Science*, 2009, **44**, 5325-5331.
296. J. G. Bai, Z. Z. Zhang, J. N. Calata and G. Q. Lu: *Ieee Transactions on Components and Packaging Technologies,* 2006, **29**, 589-593.
297. J. Yan, L. H. Rao, M. Z. Jiao, Y. Li, H. C. Cheng and S. T. Wu: *Journal of Materials Chemistry*, 2011, **21**, 7870-7877.

298. R. F. Gibson: *Composite structures*, 2010, **92**, 2793-2810.
299. V. Domenici, M. Conradi, M. Remškar, M. Viršek, B. Zupančič, A. Mrzel, M. Chambers and B. Zalar: *Journal of Materials Science*, 2011, **46**, 3639-3645.
300. H. Bai, C. Li and G. Shi: *Adv Mater*, 2011, **23**, 1089-1115.
301. S. Guicciardi, L. Silvestroni, M. Nygren and D. Sciti: *Journal of the American Ceramic Society*, 2010, **93**, 2384-2391.
302. K. S. Lee, K. S. Jang, J. H. Park, T. W. Kim, I. S. Han and S. K. Woo: *Materials & Design*, 2011, **32**, 4394-4401.
303. L. Zhang, H. Yang, X. Guo, J. Shen and X. Zhu: *Scripta Materialia*, 2011, **65**, 186-189.
304. S. Pemberton, E. Oberg, J. Dean, D. Tsarouchas, A. Markaki, L. Marston and T. Clyne: *Composites Science and Technology*, 2011, **71**, 266-275.
305. J. Yang, S. Li, Y. Luo, L. Yan and F. Wang: *Carbon*, 2011, **49**, 1542-1549.
306. J. Coughlin, J. Williams and N. Chawla: *Journal of Materials Science*, 2009, **44**, 700-707.
307. X. Li, F. Gao and Z. Gu: *Open Surface Science Journal*, 2011, **3**, 91-104.
308. P. X. Gao, C. S. Lao, W. L. Hughes and Z. L. Wang: *Chemical Physics Letters*, 2005, **408**, 174-178.
309. Z. Zhang, X. Chen and F. Xiao: *J Adhes Sci Technol*, 2011, **25**, 1465-1480.
310. G. G. Yadav, G. Zhang, B. Qiu, J. A. Susoreny, X. Ruan and Y. Wu: *Nanoscale*, 2011, **3**, 4078-4081.
311. X. Zhao, M. Fuji, T. Shirai, H. Watanabe, M. Takahashi and Y. Zuo: *Journal of Materials Science*, 2011, **46**, 4630-4637.
312. O. Krammer and B. Sinkovics: *Microelectronics Reliability*, 2010, **50**, 235-241.
313. A. Hirose, H. Yanagawa, E. Ide and K. F. Kobayashi: *Science and Technology of Advanced Materials*, 2004, **5**, 267-276.
314. W. S. Epling, G. B. Hoflund and G. N. Salaita: *The Journal of Physical Chemistry B*, 1998, **102**, 2263-2268.
315. H. Tada, J. Bronkema and A. T. Bell: *Catal Lett*, 2004, **92**, 93-99.
316. Z. Wu, Y.-W. Zhang, M. H. Jhon, H. Gao and D. J. Srolovitz: *Nano Letters*, 2012, **12**, 910-914.
317. N. Iyengar and W. Curtin: *Acta Materialia*, 1997, **45**, 1489-1502.
318. J. Chermant, G. Boitier, S. Darzens, G. Farizy, J. Vicens and J. Sangleboeuf: *J Eur Ceram Soc*, 2002, **22**, 2443-2460.
319. T. Vaughan and C. McCarthy: *Composites Science and Technology*, 2011, **71**, 388-396.
320. J. Roedel: *J Eur Ceram Soc*, 1992, **10**, 143-150.
321. H. Suemasu, A. Kondo, K. Itatani and A. Nozue: *Composites Science and Technology*, 2001, **61**, 281-288.
322. T. Suzuki, M. Sato and M. Sakai: *Journal of materials research*, 1992, **7**, 2869-2875.
323. H. Liao, Y. Wu, M. Wu and H. Liu: *Polym Compos*, 2011, **32**, 837-845.